Demonstration of a Dual Cavity Configuration for next Generation Light-Shining-Through-a-Wall Experiments

Von der Fakultät für Mathematik und Physik
der Gottfried Wilhelm Leibniz Universität Hannover

zur Erlangung des akademischen Grades
Doktor der Naturwissenschaften
- Dr. rer. nat -

genehmigte Dissertation von

M. Sc. Kanioar Karan

2021

Referent:	Apl. Prof. Dr. Benno Willke
Korreferent:	Prof. Dr. Hartmut Grote
Korreferentin:	Prof. Dr. Michèle Heurs
Tag der Promotion:	24.02.2021

Abstract

Based on peculiarities within the Standard Model of particle physics, such as the strong CP-problem, and on the observation of astrophysical phenomena, such as dark matter (DM), a group of particles, axions and axion-like particles (ALPs), is postulated. These particles are associated with a very light mass and weakly-interacting characteristics with ordinary matter. Their potential existence is the motivation for the so-called Light-Shining-Through-a-Wall (LSW) experiments. These experiments are based on the hypothesis that photons can oscillate into ALPs in the presence of magnetic fields and vice versa. The fundamental principle is to shine an intense laser beam onto a wall that is opaque to photons in the presence of a magnetic field. The interaction of the photons with the magnetic field can lead to an oscillation into ALPs that pass the wall due to their weak interaction with ordinary matter. In the presence of another magnetic field behind the wall, the reverse process can take place and the ALPs oscillate into photons that can be detected with a single photon or heterodyne detector.

The ALPS II experiment (Any Light Particle Search) is a laboratory-based experiment that exploits the mechanisms described above for the ALPs-photon conversion. To increase the probability of the production of ALPs and the regeneration of photons in front and behind the wall, two 122 m long optical resonators, called the Production Cavity (PC) and Regeneration Cavity (RC), are used. The circulating field in each cavity is directed through a string of 12 superconducting dipole magnets. In order to achieve the intended probability of production of ALPs and regeneration of photons, the frequency of the laser beam incident on the PC needs to be matched to the resonance frequency of the cavity. In addition, the cavities have to be tuned and maintained such that the field from the PC would resonate within the RC, which poses a particular challenge, since no light can reach the RC directly from the PC during the science run. This problem can be addressed by frequency doubling part of the light and injecting it into the RC for stabilization purposes. Furthermore, the eigenmodes of both cavities have to be matched spatially with high precision. Therefore, strict requirements on the lateral and angular alignment of the two eigenmodes to each other as well as on the alignment and long-term stability of the optical and mechanical components have to be fulfilled.

In the framework of this thesis, a miniaturized experiment based on ALPS II is conducted to experimentally verify some fundamental requirements for ALPS II. In contrast to ALPS II, this setup contains neither magnets nor a high power laser or a wall. First of all, the setup is used to test and verify the alignment concept, which is used to realize the desired angular alignment of the two eigenmodes. Furthermore, the long-term stability of the mechanical components that maintain the angular alignment is verified. In a further step, the methodology with which the position of the eigenmode is laterally tracked is verified and the long-term stability of the associated components is tested. In a final step, the concept of the dichroic stabilization

is demonstrated as a proof-of-concept experiment. With this concept, the cavities are tuned and maintained such that the field from the PC resonates within the RC. Therefore, the frequencies of the lasers used are stabilized to the respective eigenfrequencies of the cavities and a phase-locked loop is implemented to ensure that the PC field resonates within the RC.

Keywords: Light-Shining-Through-a-Wall, Axions, Axion-Like Particles, Optical Cavities, ALPS II

Kurzfassung

Basierend auf Auffälligkeiten innerhalb des Standard Models der Teilchenphysik, wie z.B. das starke CP-Problem, sowie auf der Beobachtung astrophysikalischer Phänomene, wie das Phänomen der dunklen Materie (DM), wird eine Gruppe von hypothetischer Partikeln, Axionen und axionenartige Partikel (engl.: Axion-like particles, ALPs), postuliert. Diesen Partikeln werden eine sehr leichte Masse sowie sehr schwache Wechselwirkungen mit der sichtbaren Materie zugewiesen. Ihre mögliche Existenz ist die Motivation für sogenannte Licht durch die Wand-Experimente (engl.: Light-Shining-through-a-Wall, LSW). Diese Experimente basieren auf der Annahme, dass Photonen in Gegenwart von Magneltfeldern in ALPs oszillieren können und umgekehrt. Das wesentliche Prinzip basiert darauf, einen intensiven Laserstrahl in Gegenwart eines Magnetfeldes auf eine für Photonen undurchlässige Wand zu richten. Durch die Interaktion der Photonen mit dem Magnetfeld kann es zur Entstehung eines ALPs kommen, welches aufgrund der schwachen Wechselwirkung mit der normalen Materie die Wand passiert. Hinter der Wand kann es in Gegenwart eines weiteren Magnetfeldes zum umgekehrten Prozess kommen und das ALP oszilliert in ein Photon, welches mit einem Einzelphotonenzähler oder einer hetrodynen-Detektion detektiert werden kann.

Das ALPS II-Experiment (Any Light Particle Search) ist ein laborbasiertes Experiment, welches die oben beschriebenen Mechanismen für die ALPs-Photonen-Konversion ausnutzt. Um die Wahrscheinlichkeit der Produktion von ALPs und der Regeneration von Photonen vor bzw. hinter der Wand zu erhöhen, wird jeweils ein 122 m langer optischer Produktions (PC)- bzw. Regenerationsresonator (RC) verwendet. Das zirkulierende Feld der Resonatoren wird dabei jeweils durch eine serielle Anordnung von 12 supraleitenden Dipolmagneten geleitet. Um die angestrebte Wahrscheinlichkeit der Produktion bzw. Regeneration von ALPs zu erzielen, muss der auf den Produktionsresonator einfallene Laserstrahl an die Resonanzfrequenz des Resonators angepasst werden. Weiterhin müssen die Resonatoren so angepasst werden, dass das Feld aus der PC innerhalb der RC resonant ist. Dabei muss die Abstimmung für die Messzeit erhalten werden, was besonders herausfordernd ist, da während der Datenaufnahme kein Licht direkt aus der PC in die RC gelangen darf. Dieses Problem wird gelöst, indem ein Teil des Lichtes frequenzverdoppelt und zur Stabilisierung in die RC eingespeist wird. Des Weiteren müssen die Eigenmoden beider Resonatoren örtlich mit einer hohen Präzision aufeinander ausgerichtet werden. Dies stellt besondere Anforderungen an die laterale Ausrichtung, an den Winkel der beiden Eigenmoden zueinander sowie an die Justage und Langzeitstabilität der optischen und mechanischen Komponenten.

Im Rahmen der vorliegenden Dissertation wird ein miniaturisiertes, an ALPS II angelehntes Experiment demonstriert, mit dessen Hilfe einige der oben erwähnten Anforderungen von ALPS II experimentell verifiziert werden. Im Gegensatz zu ALPS II beinhaltet dieser Aufbau keine

Magneten, keinen Hochleistungslaser und keine lichtundurchlässige Wand. Zunächst wird mit dem Aufbau das Ausrichtungskonzept, mit dem die angestrebte Winkelausrichtung der beiden Eigenmoden realisiert werden soll, getestet und anhand verschiedener Messungen verifiziert. Weiterhin wird die Langzeitstabilität der mechanischen Komponenten, welche die Winkelausrichtung aufrecht erhalten, verifiziert. In einem weiteren Schritt wird die Methodik, mit dessen Hilfe die Position der Eigenmode in lateraler Ausrichtung verfolgt werden soll verifiziert und die Langzeitstabilität der dazugehörigen Komponenten getestet. In einem abschließenden Schritt wird das Konzept der dichroitischen Stabilisierung getestet. Mit dieser Methodik werden die Resonatoren so angepasst, dass das Feld aus der PC innerhalb der RC resonant ist. Hierfür werden die Frequenzen der verwendeten Laser auf die Eigenresonanzen der Resonatoren stabilisiert und anschließend eine Phasenregelschleife implementiert, welche gewährleistet, dass das Feld aus der PC für die Messzeit innerhalb der RC resonant ist.

Stichwörter: Licht durch die Wand, Axionen, axionenartige Partikel, Optische Resonatoren, ALPS II

Contents

List of Figures

List of Tables

List of Abbreviations

AC	Autocollimator
ALPS	Any Light Particle Search
ALPs	Axion-like Particles
COB	Central Optical Bench
FSR	Free Spectral Range
IR	Infrared
PC	Production Cavity
PLL	Phase-Locked Loop
PPKTP	periodically poled potassium titanyl phosphate
PZT	piezo-electric transducer
QCD	Quantum Chromodynamics
RC	Regeneration Cavity
RMS	Root Mean Square
ROC	Radius of Curvature
ROC	Randius of curvature
SHG	Second Harmonic Generation

SM	Standard Model
TEC	Thermoelectric Cooler

List of Symbols

ρ	Cavity round trip loss
T	Mirror power transitivity
ω_p	photon angular frequency
F_f	Form factor
L_in	Interaction length
m_A	Mass of ALPs
$P_{\gamma \to a}$	Coupling probability between photons and ALPs
P_{tot}	Coupling probability for LSW experiments
q	Momentum transfer
α	tilt angle
β	diffraction-limited resolution angle
β_{PC}	Power build-up Production Cavity
β_{RC}	Power build-up Regeneration Cavity
δ	wedge angle
$\delta\alpha_{eig}$	tilt angle of the eigenmode
Δ_{eig}	lateral mismatch of waist position
$\delta_{Z0,eig}$	longitudinal mismatch of waist
ε_n	mode content order n
γ	electro-magnetic field

γ^*	virtual photon field
Λ	Wavelength
$\mathbb{F}$	Finess
$\omega_{0,eig}$	Waist radius of the eigenmode
$\theta_{0,eig}$	Half Divergent angle of the eigenmode
ζ	Coupling efficiency
B	Magnetic field
D	Free aperture
d	shift
d_{eff}	Non-linear coefficient
F	focal length
L	Cavity length
n	refractive index
N_{LSW}	Number of regenerated photons
T	Temperature
U_n	power in mode order n
Z_R	Rayleigh range

Chapter 1

Introduction

All physical processes known so far that are associated with ordinary matter can be described by the four fundamental forces [1]. Three of these forces, namely the strong, the weak and the electromagnetic force, are combined in a single model, the so-called Standard Model (SM) of particle physics [2], which describes these forces as an exchange of bosonic particles and thus the interaction between all known particles in the universe. The particles predicted by the SM have all been proven to exist, one after the other, by various experiments. The most recent confirmation of the SM was the discovery of the Higgs boson [3], which was awarded with the Nobel Prize in 2013 [4–6].

Despite its success, the SM has also some shortcomings. Based on precise measurements of the cosmic microwave background radiation, it is known that only 4.9 % of the universe is made of ordinary matter. Dark matter (DM) with 26.8 % and dark energy (DE) with 68.3 % make up the largest part of the universe [7]. The only thing known about the latter is that it is the driver of the expansion of the universe. Similarly, very little is also known about the nature of dark matter, only that it interacts via gravity with ordinary matter. Considering also current models of the history of the universe, the SM does not provide any explanation for dark matter or dark energy. A potential solution to the question of what DM is made of might result from another problem that the SM is confronted with: the strong CP-problem. It is generally know that the weak force violates the CP-symmetry, i.e. the symmetry of a physical process under inversion of charge (C) and the spatial coordinates (P, Parity) [8]. However, there exists no experimental evidence for the strong interaction also violating this symmetry, although quantum chromodynamics (QCD) includes a parameter $\overline{\theta}$, which theoretically allows for it [9]. Although, from a theoretical point of view, this parameter doesn't necessarily have to be very small [10], experimental measurements indicate a value of $< 10^{-10}$ [11]. A possible solution to that dilemma is proposed by Robert Peccei and Helen Quinn, which is to extend the SM by an additional U(1) symmetry that is spontaneously broken at low energies. A descriptive consequence of this

broken Peccei-Quinn (PQ) symmetry is the existence of a new pseudoscalar-boson, the axion, which is not included in the SM [10, 12]. Due to its very light-weight mass and weak interaction with ordinary matter, the axion might be a prominent candidate for DM [13]. Besides the axion, there are some astrophysical hints, such as the transparency of the universe for TeV photons [14] and an unusual cooling behavior of some white dwarfs [15], which indicates further particles beyond the SM with similar properties as the axion, the axion-like particles (ALPs). All these particles are summarized under the generic name *weakly-interacting slim particles* (WISPs). It should be noted here that in the further course of this thesis no distinction between axions and ALPs is made.

1.1 Search for ALPs

Although these hypothetical particles have at maximum a very weak interaction with ordinary matter, it is possible to probe their existence based on the assumption that the ALPs can couple to two photons [16]. Typically, one photon is provided by a known light source that propagates along a static magnetic field that supplies the second photon, which is virtual. The conversion probability of a photon to an ALP can then be expressed by the formula

$$P_{\gamma\to a} = \frac{1}{4}\frac{\omega_p}{\sqrt{\omega_p^2 - m_A^2}}\left(g_{A\gamma\gamma}BL_B\right)^2\left|F_f(qL_B)\right|^2. \tag{1.1}$$

Employing natural units, i.e. $\hbar = c = 1$, ω_p is the photon angular frequency, m_A is the ALP mass, $g_{A\gamma\gamma}$ is the coupling constant between the photons and the ALPs, B is the magnetic field strength, L_B is the magnetic field length in the direction of the photon propagation, F_f is the form factor and q is momentum transfer to the magnetic field [16]. The form factor is given by

$$\left|F_f(qL_B)\right| = \left|\frac{2}{qL_B} sin\left(\frac{qL_B}{2}\right)\right|, \tag{1.2}$$

where the momentum transfer q is defined as

$$q \approx \omega_p(n-1) + \frac{m_A^2}{2\omega_p}, \tag{1.3}$$

and n is the refractive index of the propagation medium of the photons. It should be noted that the conversion probability is identical in both directions, i.e. from photons into ALPs and vice versa [16].

Based on this probability of oscillation between photons and ALPs, a series of experiments is performed to prove the existence of these particles. These experiments can be summarized in three categories [17]: the first category are the *haloscopes*. This type of experiment aims

at ALPs of the dark matter halo of the Milky Way. These ALPs are associated with a specific energy, which is in the microwave range. Therefore, microwave cavities enclosed by strong magnetic fields are used for the search. If ALPs are present in the dark matter halo and reach the microwave cavity, they can oscillate into a photon by the mechanisms described previously and then be detected by a microwave receiver. Some prominent examples of experiments with haloscopes are the *Axion Dark Matter Experiment* (ADMX) [18], the *Magnetized Disc and Mirror Axion Experiment* (MADMAX) [19] and *ABRACADABRA* [20].

Another category are the *helioscopes*. These types of experiments focus on potential ALPs that could be generated in the stellar core. For that purpose, optically opaque telescopes, which are also enclosed by a strong magnetic field, are directed towards the sun. In the magnetic field of the telescope, ALPs can oscillate into X-ray photons that can be detected by X-ray detectors. Some examples of these experiments are the *CERN Axion Solar Telescope* (CAST) [21] and the the *International Axion Observatory* (IAXO) [22].

As the description of the two previous methods shows, the probability of ALPs-photon conversion depends strongly on the modeling of the respective ALPs source. This disadvantage is not present in the third category of experiments, the *Light-shining-through-a-wall* (LSW) experiments, where the photon-ALP-photon conversion is purely laboratory-based. This has the advantage that the photon source and the magnetic field - and with it the ALPs source - is precisely defined up to the coupling efficiency, which simplifies the interpretation of the experimental results. The principle of these experiments is shown schematically in Figure 1.1. The

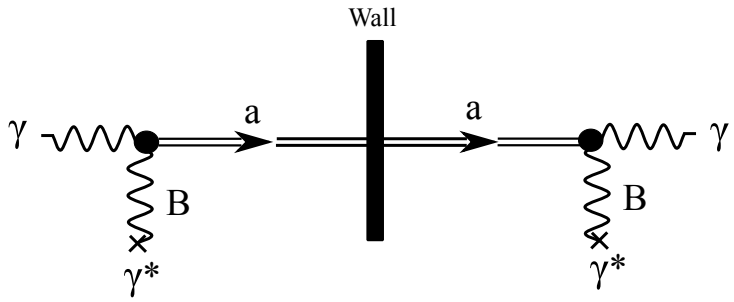

Figure 1.1: Feyman diagram of light-shining-through-wall experiments, in which γ represents an electro-magnetic field, γ^* represents a virtual photon field supplied by the magnetic field B, and a represents an ALPs field. Two magnetic fields are separated by a wall that is opaque to photons. In front of the wall, the photon can interact with the virtual photon and leads to an oscillation into ALPs, which can pass the wall. Behind the wall the inverse process can take place and the ALPs oscillate into a detectable photon.

basic principle is to shine photons from a known source onto a wall that is opaque for photons in the presence of a magnetic field. The photons can interact with the magnetic field, which supplies virtual photons. This process leads to an oscillation into ALPs. Due to the weak interaction with ordinary matter, ALPs can pass the wall. On the other side of the wall, and in

the presence of another magnetic field, the reverse process can take place and the ALPs can re-convert into detectable photons. Examples for such LSW experiments include ALPS I [23], OSQAR [24], GammeV [25] and BMV [26].

Due to the two necessary conversions, i.e. generation of ALPs before the wall and regeneration of photons behind the wall, the following total probability results for the entire LSW process [16]:

$$P_{tot} = P_{\gamma \to a} P_{a \to \gamma}, \tag{1.4}$$

where $P_{\gamma \to a}$ represents the probability for ALPs generation before the wall and $P_{a \to \gamma}$ the probability for photon regeneration behind the wall, as defined in Equation 1.1. The corresponding number of regenerated photons is then given by

$$N_{LSW} = \frac{P}{\omega_p} \Delta t P_{tot} \eta, \tag{1.5}$$

with P being the optical power incident on the wall, Δt the measurement time and η the efficiency of the photon detector [16]. As can be seen from Equation 1.5, the number of regenerated photons is proportional to the optical power in front of the wall. The *Any Light Particle Search II* experiment (ALPS II) [27], the successor of ALPS I, exploits this fact by using an optical cavity, the Production Cavity (PC), in combination with a laser, which significantly increases the number of photons in front of the wall. To also boost the regeneration of photons, another optical cavity, the Regeneration Cavity (RC), is used on the other side of the wall [28]. In order to achieve the desired probability of photon-ALP-photon conversion, the frequency of the laser incident on the cavity needs to be matched to the resonance frequency of the Production Cavity. In addition, both cavities have to be tuned such that the photons from the Production Cavity would resonate within the Regeneration Cavity if there is no wall. Furthermore, the eigenmodes of both cavities have to be spatially matched with a high precision.

In the framework of this thesis, a setup is demonstrated to experimentally verify some fundamental requirements for ALPS II. The setup is first used to verify the anticipated requirements regarding the spatial overlap of both cavities. In a second attempt the setup is used to demonstrate a concept, which ensures that the field from the Production Cavity resonates within the Regeneration Cavity.

1.2 Outline of this thesis

This thesis is arranged as follows: In **Chapter 2**, the optical layout of the ALPS II experiment is briefly explained. **Chapter 3** introduces a setup that represents a miniaturization of the ALPS II experiment. The individual stages of the setup are presented with their specifications and func-

tions. In **Chapter 4**, this setup is used to demonstrate some fundamental requirements of the ALPS II experiment. These are the concepts for the alignment of the planar cavity mirrors of the Production and Regeneration Cavity as well as the long-term performance of the associated mechanical components. Furthermore, the concept of tracking the eigenmode of both cavities is demonstrated and the long-term performance of the components used is verified. In **Chapter 5**, the same setup is used to demonstrate the entire length and frequency stabilization of ALPS II as a proof-of-concept experiment. This includes the stabilization of the frequency of the lasers to the resonances of the cavities and the implementation of a phase-locked loop, which ensures that the field from the Production Cavity resonates within the Regeneration Cavity. The design of the individual loops is presented and their performances are investigated. A summary of this thesis is given in **Chapter 6**.

Chapter 2

Optical layout of ALPS II

This chapter gives an overview of the optical layout of the ALPS II experiment and is arranged as follows: Section 2.1 describes the general design of the experiment. Section 2.2 gives an overview of the requirement regarding the spatial overlap between the two cavities. Finally, a summary of the control architecture for the transition edge sensor (TES) detection scheme is presented in Section 2.3.

2.1 Experimental design

Figure 2.1 shows a schematic of the ALPS II experiment. The experiment, which is planned to be performed at the *Deutsches Elektronen-Synchrotron* (DESY) in Hamburg, can be divided into three sections, which are depicted as Optical Bench 1 (OP1), Central Optical Bench (COB) and Optical Bench 2 (OP2). The High Power Laser (HPL), which is used to seed the Production Cavity[1], is installed on the OP1 together with the input mirror M_{PCI} of the Production Cavity. The laser is a single-frequency *Nonplanar Ring Oscillator* that operates at a wavelength of 1064 nm. Its output power is amplified by a laser amplifier system, similar to [30], to a maximum output power of 70 W. The planar output mirror M_{PCO} of the Production Cavity is located at a distance of ≈ 122 m apart from OP1 on the Central Optical Bench and forms a plano-concave cavity together with the input mirror. The input mirror M_{PCI} has a higher transitivity than the output mirror M_{PCO}, such that the Production Cavity is over-coupled to maximize the profitability for ALPs generation. The circulating beam of the cavity is directed through a string of 12 superconducting dipole magnets with a corresponding magnetic field times length product of $BL_B = 560\mathrm{T}\cdot\mathrm{m}$.

The planar mirror M_{RCI} of the Regeneration Cavity is also located on the Central Optical Bench. It forms a plano-concave cavity with the output mirror M_{RCO}, which is located at

[1] A detailed description of optical cavities and Gaussian beams can be found in [29].

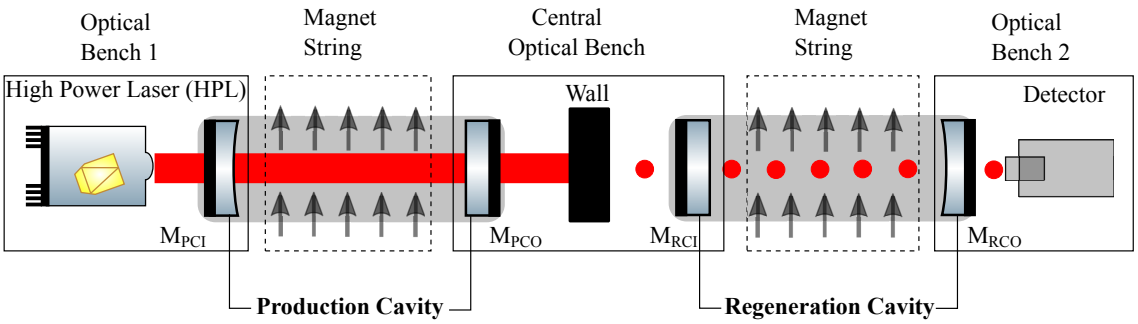

Figure 2.1: Schematic overview of the ALPS II experiment. The probability of producing ALPs in front of the wall is enhanced by an optical cavity, the so-called Production Cavity, which is seeded by a High Power Laser (HPL). On the other side the wall, the probability for photon regeneration is enhanced by another optical cavity, the so-called Regeneration Cavity. The circulating beam of both cavities is directed through a string of 12 superconducting dipole magnets. The solid red line represents the ALP-producing photon field while the dotted red line represents the ALP-regenerated photon field.

a distance of $\approx$ 122 m on the OP2. Its circulating beam is also directed through a similar magnet configuration as the circulating Production Cavity beam. To prevent photons from the Production Cavity from entering the Regeneration Cavity, a wall that is opaque to photons from the Production Cavity shields the two cavities from each other.

ALPS II uses two detection schemes with very different systematics to measure the reconverted photon, which will help to increase the confidence in the measurement [27]. For both detection schemes two different optical systems are required. The first system used is based on a hetrodyne (HET) detection. Its optical system is described in [31]. In this concept an interference beat note is generated between a local oscillator, which is a laser, and the regenerated photon field on a photo detector. The signal of the photo detector is demodulated with a known frequency difference between the ALPs generating High Power Laser and the local oscillator, which provides a signal that is proportional to the regenerated field strength. The second detection system, which is the focus of this thesis, uses a so-called transition edge sensor (TES) [32]. It consists of an absorptive tungsten chip whose temperature is kept at the threshold of superconductivity. If a photon is incident on the sensor, it is absorbed and causes a slight increase of the temperature. This increases the resistance of the chip, which leads to a measurable drop in the current flowing through the chip. The control architecture of this detection scheme is described in Section 2.3.

For such a cavity-enhanced LSW experiment, the number of the regenerated photons is given by

$$N_{LSW} = \frac{1}{16} \cdot \zeta^2 \cdot \frac{P}{\omega_p} \cdot \left(g_{A\gamma\gamma} \left| F_f(qL_B) \right| BL_B\right)^4 \cdot \beta_{PC}\beta_{RC} \cdot \Delta t, \tag{2.1}$$

with ζ^2 being the power coupling efficiency between the eigenmodes of both cavities and β_{PC} and β_{RC} the power build-up factor of the Production and Regeneration Cavity, respectively. The corresponding sensitivity of the LSW experiment is defined as [16]:

$$g_{A\gamma\gamma} = \frac{2}{BL_B \left|F_f(qL_B)\right|} \cdot \left(\frac{1}{\zeta}\right)^{\frac{1}{2}} \cdot \left(\frac{N_{LSW}\,\omega_p}{\beta_{PC}\beta_{RC}P\Delta t}\right)^{\frac{1}{4}}. \tag{2.2}$$

The power build-up parameters are defined as

$$\beta_{PC} \approx \frac{4 \cdot T_{PCI}}{(T_{PCI} + T_{PCO} + \rho)^2} \tag{2.3}$$

and

$$\beta_{RC} \approx \frac{4 \cdot T_{RCI}}{(T_{RCI} + T_{RCO} + \rho)^2}, \tag{2.4}$$

where T represents the power transitivity of the respective mirror and ρ represents the round trip power loss of the respective cavity [29]. The targeted sensitivity for ALPS II is given by $g_{A\gamma\gamma}$ = $2 \cdot 10^{-11}$/GeV, which requires an nominal power build-up of β_{PC} = 5000 for the Production Cavity and β_{RC} = 40,000 for the Regeneration Cavity [32]. However, the initial power build-up for the Regeneration Cavity is planned to be 10,000 for the first science run, which results in an initial sensitivity of $g_{A\gamma\gamma}$ = $2.8 \cdot 10^{-11}$/GeV. This corresponds to a photon rate of $n_{LSW} \approx 2.8 \cdot 10^{-5}$/s, which is $\approx$ 2.5 photons per 24h.

2.2 Overlap requirements

As can be seen from Equation 2.2, the coupling efficiency ζ is one crucial parameter to reach the desired sensitivity. It describes the coupling of the ALP field to the eigenmode of the Regeneration Cavity. Since the regenerated photons are identical to the photons circulating within the Production Cavity, this parameter can be expressed as the overlap between the eigenmode of the Production and Regeneration Cavity. It is composed of the spatial and spectral overlap of both cavities. While the spatial overlap includes the transverse and the angular mismatch of the eigenmode of both cavities, the spectral overlap describes the mismatch of the resonance frequencies of both cavities. The anticipated total overlap is $\geq$ 90 % [32, 33]. Here, a maximum power loss of 5 % is tolerated regarding the spatial mismatch of the eigenmodes of the two cavities. The remaining 5 % can be introduced by the spectral degree of freedom. If the line-width of the Regeneration Cavity, which is 15 Hz, is taken into account, 5 % loss for the spectral degree of freedom results in a mismatch of 0.5 Hz between the resonant frequencies of both cavities. The spatial overlap consist of the lateral, the angular and the axial degree of freedom and the waist size ratio of both cavities. It can be described with the misalignment

parameter $|\varepsilon|^2$, which describes the percentage power coupled into higher-order modes on a perturbative basis as

$$|\varepsilon|^2 \approx |\varepsilon_1|^2 + |\varepsilon_2|^2 \approx \frac{|U_1|^2}{|U_0|^2} + \frac{|U_2|^2}{|U_0|^2}$$
$$\approx \left(\frac{\delta\alpha_{eig}}{\theta_{0,eig}}\right)^2 + \left(\frac{\Delta_{eig}}{\omega_{0,eig}}\right)^2 + \left(\frac{\delta z_{0,eig}}{2\cdot Z_R}\right)^2 + \left(\frac{\delta\omega_{eig}}{\omega_{0,eig}}\right)^2, \tag{2.5}$$

where $|U_n|^2$ represents the power in a Hermite-Gaussian mode of order n, $\delta\alpha_{eig}$ is the relative angle, Δ_{eig} is the relative lateral position, $\delta z_{0,eig}$ is the relative axial beam waist position, and $\delta\omega_{eig}$ is the waist radius difference between the two cavity eigenmodes; $\theta_{0,eig}$ is the half divergence angle, $\omega_{0,eig}$ is the waist radius and Z_R is the Rayleigh range of the cavity eigenmodes [34, 35]. The latter two terms in Equation 2.5, $\delta z_{0,eig}$ and $\delta\omega_{eig}$, depend on the distance between the two planar cavity mirrors and the difference in the radii of the curvature of the curved mirrors of both cavities. The first two terms in Equation 2.5 depend on the angular and the lateral alignment of the cavity eigenmodes with respect to each other. To meet the anticipated requirements on the spatial overlap, the misalignment in angular and lateral degree of freedom should not exceed 5 μrad and 100 μm, respectively [32, 33].

In Chapter 3 and 4, the concepts with which these two degrees of freedom are controlled are presented and the feasibility to achieve the desired requirements regarding the lateral and angular degree of freedom is demonstrated.

2.3 Control architecture for the TES detection scheme

A schematic overview of the control architecture of the TES detection system is shown in Figure 2.2. To increase the number of photons before the wall, the frequency of the High Power Laser is stabilized to the resonance frequency of the Production Cavity using the Pound-Drever-Hall locking technique [36]. Since no light from the Production Cavity is allowed to reach the Regeneration Cavity during the science run, a second laser, the Reference Laser, is used to make the field from the Production Cavity resonant within the Regeneration Cavity. The fundamental beam of the Reference Laser is frequency doubled and injected to the Regeneration Cavity to stabilize its frequency to the resonance frequency of the Regeneration Cavity. While the frequency of both lasers are individually stabilized, an offset phase-locked loop (PLL) ensures that the field circulating in the Production Cavity also resonates within the Regeneration Cavity. For this purpose, a beat note signal of the transmitted field of the Production Cavity and the fundamental field of the Reference Laser is generated, which is sensed by a photodiode $\mathrm{PD_{PLL}}$.

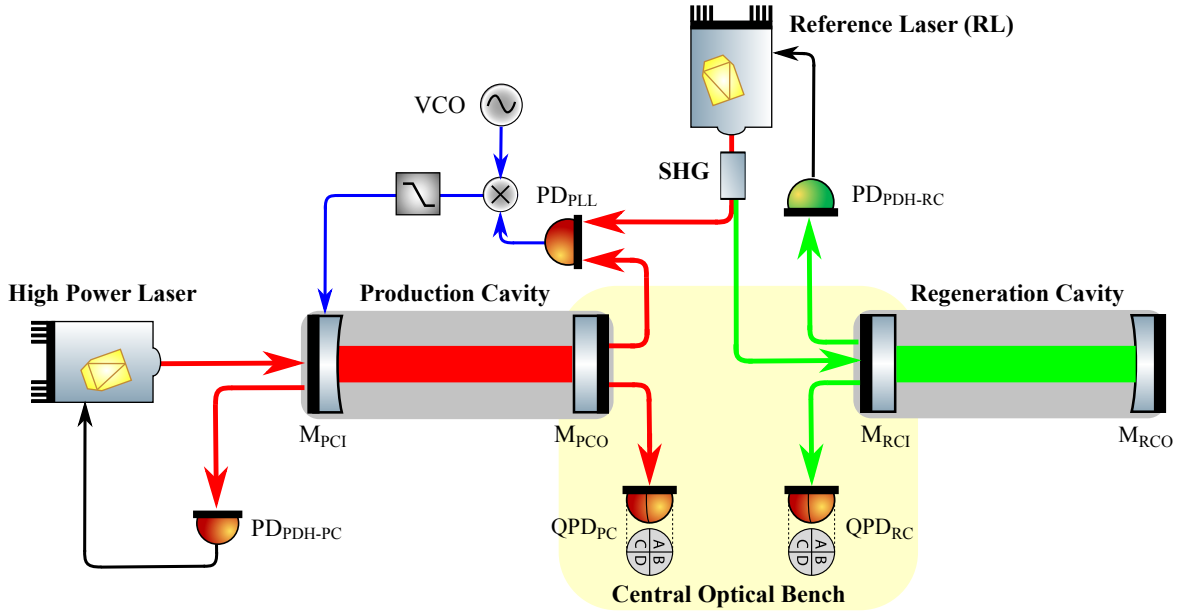

Figure 2.2: Control architecture of the ALPS II experiment for the TES detection scheme. The frequency of the High Power Laser is stabilized to the resonance frequency of the Production Cavity via its fundamental beam. At the same time the frequency of the Reference Laser is stabilized to the resonance frequency of the Regeneration Cavity via its frequency-doubled beam. Additionally, a phase-locked loop is implemented to match the frequency of the Production Cavity field to the resonance frequency of the Regeneration Cavity. Two quadrant photodiodes are used to track the eigenmode position of the cavities. Green lines depict the second harmonic beam of the Reference Laser while red lines represent the fundamental beam of the High Power and Reference Laser. Black lines depict electric wiring for frequency stabilization of the lasers and blue lines denote electric wiring for the phase-locked loop.

This beat note signal is than matched via the PLL to an anticipated offset frequency from a voltage-controlled oscillator (VCO) [37]. If the beat note frequency drifts, the PLL acts on the length of the Production Cavity to keep the beat note frequency matched to the desired offset frequency. The offset of the PLL is due to the fact, that the ration between the harmonic frequency of the Reference Laser and the High Power Laser within the Regeneration Cavity is not an integer of factor two, which is due to characteristics of the dichroic coatings of the cavity mirrors. The offset frequency, with which the beat note signal is compared with, represents the offset frequency between the two fields within the Regeneration Cavity. This experimental configuration, in which both the infrared beam from the Production Cavity and the frequency-doubled beam of the Reference Laser are resonant within the Regeneration Cavity, is referred to as dichroic locking in the further course of this thesis.

A detailed description of the frequency and length stabilization is given in Chapter 5, where the entire stabilization concept is demonstrated.

The eigenmodes of the two cavities are tracked by the quadrant photodiodes $\mathrm{QPD_{PC}}$ and

QPD_{RC} to ensure the desired spatial overlap in lateral degree of freedom. This places special demands on the long-term stability of the mounts of the quadrant photodiodes with respect to drifts. To ensure the desired special overlap in the lateral degree of freedom, the drift should not exceed 100 μm over the measurement time of ALPS II. In Chapter 3, a mechanical design for the mounts of the quadrant photodiodes is presented and the corresponding long-term stability is verified in Chapter 4. Furthermore, two different mounting schemes are presented for the planar mirrors of both cavities in Chapter 3 and the associated long-term stability is verified in Chapter 4.

Chapter 3

The ALPS 1m-prototype

A miniaturized 1m-prototype version of ALPS II is designed and built in Hanover, at the AEI, to verfiy some anticipated ALPS II requirements. Unlike ALPS II, the prototype cavities are operated in air without magnets, high power lasers and a wall. It is used to test the concept of the Central Optical Bench, which in conjunction with the two planar cavity mirrors and the quadrant photodiodes determines for the ALPS cavities the angular and lateral degrees of freedom, respectively. For this purpose, the alignment feasibility regarding the angular degree of freedom of the mirrors with respect to each other is investigated. Furthermore, the long-term performance of the corresponding mounting frame of the planar mirrors is investigated. Additionally, this test bed is used to verfiy the long-term stability of the mechanical mounts for the quadrant photodiodes. Furthermore, it is used to test the dichroic lock scheme of the Regeneration Cavity, which determines the requirements on the spectral degree of freedom, as a proof-of-concept experiment.

This chapter is structured as follows: Section 3.1 gives a general overview of the experimental setup. The Section 3.2 introduces the second harmonic generation stage (SHG), which is designed and characterized for the dichroic lock concept of the Regeneration Cavity. In Section 3.3, the Central Optical Bench (COB) with the mounting concepts for the planar mirrors and the quadrant photodiodes is described. This is followed by a description of the Production Cavity in Section 3.4 and concluded with a description of the Regeneration Cavity in Section 3.5.

3.1 Experimental setup

Figure 3.1 shows a schematic overview of the 1m-prototype setup, which is realized on a single optical table. The infrared light of a laser, called High Power Laser (HPL)[1], is mode matched to the eigenmode of the Production Cavity by some lenses, ML1 and ML2, and its correspond-

[1] This is not a high power laser. The designation only refers to the ALPS convention.

ing power is adjusted by a variable attenuator consisting of a $\lambda/2$ - waveplate and a polarizing beamsplitter PBS1. The laser used is a single-frequency *Nonplanar Ring Oscillator* (NPRO) designated *Memphisto* with a maximum optical power of 2 W and a corresponding wavelength of 1064 nm. A Faraday rotator, FI1, and a polarizing beamsplitter, PBS2, are used to separate the beam reflected from the Production Cavity from the injected beam. This reflected beam is sensed by a photodiode, $PD_{PDH\text{-}PC}$, to stabilize the frequency of the High Power Laser to the resonance frequency of the Production Cavity using the Pound-Drever-Hall locking technique [36, 38]. An electro-optical modulator, EOM_{PC}, is used to imprint sidebandes at 3.5 MHz to the optical frequency of the High Power Laser to generate the corresponding error signal. The High Power Laser frequency is actuated by a piezo-electric transducer (PZT), which is attached to the laser crystal. A detailed description of the frequency stabilization is given in Chapter 5. The Production Cavity is set up in a plano-concave configuration. Its curved mirror, M_{PCI},

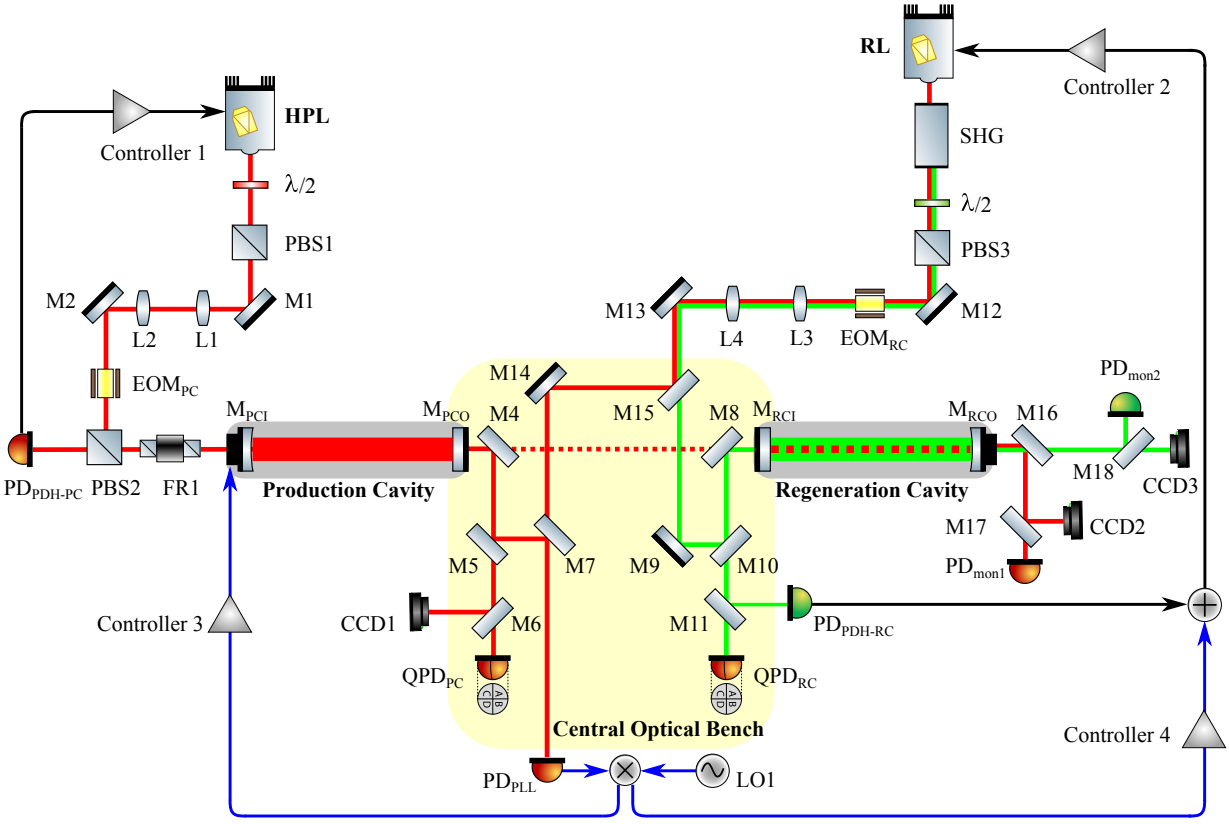

Figure 3.1: Schematic overview of the ALPS 1-m-prototype, where: EOM is representing electro-optical modulator, L lens, LO local oscillator, M optical mirror, PBS polarization beamsplitter, PD photodiode, QPD quadrant photodiode and SHG second harmonic generation. Furthermore: red lines depict infrared light, dashed red lines denote infrared light from the Production Cavity entering the Regeneration Cavity, green lines depict visible second harmonic light, black lines denote electric wiring for the Pound-Drever-Hall locking, and blue lines denote electric wiring for the phase-locked loop.

is fixed in a brass mount, which is in turn placed on a pitch-yaw stage. This stage is used for coarse alignment of the eigenmode of the Production Cavity. For fine-tuning alignment, a PZT with three control elements is glued to the curved mirror. The planar mirror, M_{PCO}, is fixed to the Central Optical Bench with custom-made mounts as described in Section 3.3. To track the eigenmode position, which is located on the planar mirror, a part of the transmitted Production Cavity beam is directed to a quadrant photodiode, QPD_{PC}, by means of the mirror M4 (T = 10 %, R = 90 %). A fraction of the transmitted Production Cavity beam is also injected into the Regeneration Cavity, as depicted in dashed red lines in Figure 3.1, for test purposes.

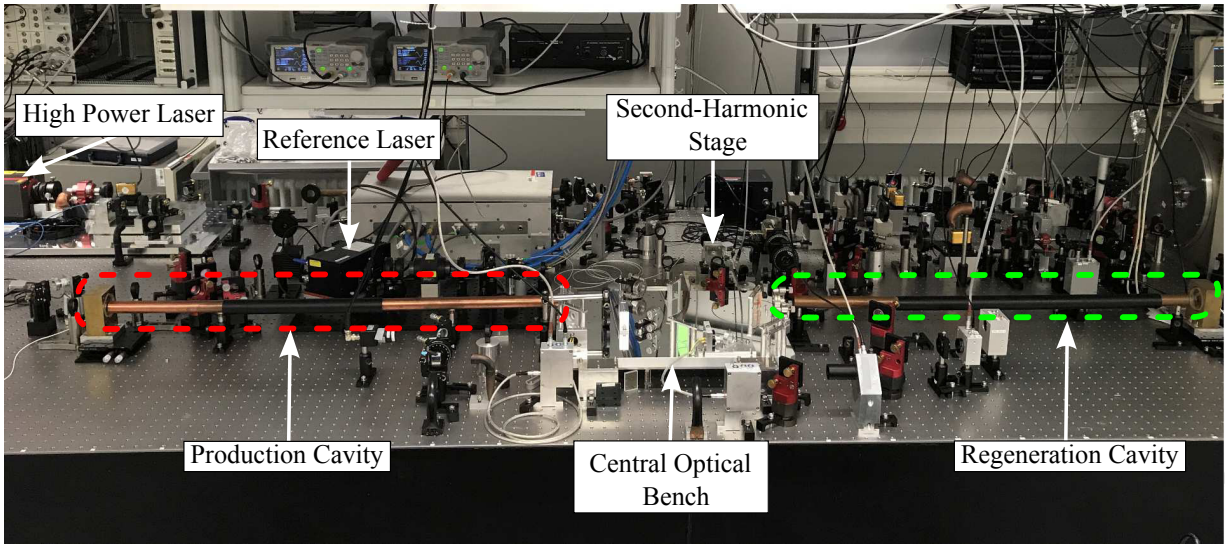

Figure 3.2: Photograph of the 1m-prototype. The entire experiment is set up on a single optical table. Both cavities are shielded by metal tubes to minimize the effect of air fluctuations on the cavity length.

To interrogate the Regeneration Cavity continuously, the frequency of a Reference Laser (RL) is doubled using a nonlinear PPKTP crystal, as described in Section 3.2. The laser used is also a single-frequency NPRO with a maximum fundamental power of 200 mW at 1064 nm from *Innolight*. The fundamental beam is separated from the second harmonic beam on the Central Optical Bench using a dichroic mirror M15 (HT @532 nm / HR @1064 nm). It is mode matched, by lenses ML3 and ML4, and injected to the Regeneration Cavity (RC), which is also set up in a plano-concave configuration. Similar to the Production Cavity, the power of the second harmonic beam is adjusted by a variable attenuation station consisting of a polarizing beamsplitter, PBS3, and a $\lambda/2$ - waveplate. The planar mirror of the Regeneration Cavity is attached to the Central Optical Bench with a commercial highly-stable mount designed for circular substrates. The curved mirror is placed on an identical stage as the curved Production Cavity mirror. The back-reflected beam by the Regeneration Cavity is split by a beamsplitter, M11, into two parts, which are sensed by the quadrant photodiode QPD_{RC} and a single-element photodiode PD_{PDH-RC} for tracking the eigenmode location of the Regeneration Cavity and for

frequency stabilization of the Reference Laser, respectively. The frequency stabilization is done in analogy to the Production Cavity.

Compared to ALPS II, the Regeneration Cavity of the prototype is not optically isolated from the Production Cavity by an opaque wall. However, in order to demonstrate the dichroic lock concept of the Regeneration Cavity, an offset phase-locked loop (PLL) [39–42] is implemented between the fundamental field of the Reference Laser and the transmitted field of Production Cavity. Mirror M7 (50:50%) is used to direct a part of the transmitted Production Cavity beam to the photodiode PD_{PLL}, which is used to sense the beat signal of the fundamental field of the Reference Laser and the Production Cavity transmitted field. To keep the Production Cavity field resonant in the Regeneration Cavity, this beat note signal is matched to a reference frequency from a local oscillator LO1. For any changes of the beat note signal, the length of the Production Cavity is actuated by means of its PZT to keep the beat note signal matched to the LO1 frequency. To keep this control loop robust, ALPS II adjusts at high frequencies the frequency of the voltage-controlled oscillator (VCO) used for LO1 [37]. In contrast, for the 1m-prototype a control signal is fed to the error point of the frequency stabilization control system of the Reference Laser to provide robustness to the PLL. A detailed explanation with corresponding experiments of the dual resonance cavities is given in Chapter 5.

3.2 Second harmonic stage

For the demonstration of the dichroic lock concept of the Regeneration Cavity, a single-path second harmonic stage is designed and built, which is briefly described in the following section.

3.2.1 Optical and mechanical design

Figure 3.3 shows a schematic overview of the designed second harmonic stage. The fundamental laser used is the Reference Laser described in the previous section. Its beam is mode matched

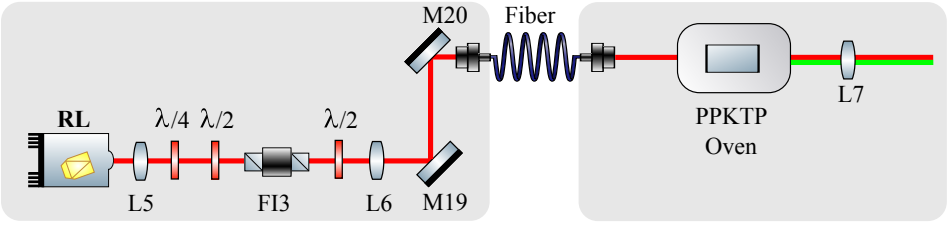

Figure 3.3: Schematic of the second harmonic stage. The fundamental laser (RL) and the PPKTP crystal are installed on individual transportable breadboards. Red lines denote infrared fundamental light, green line depicts visible harmonic light, L are lenses, M denotes mirrors and FI depicts Faraday isolator.

by a pair of lenses, L5 and L6, to the mode of a polarization-maintaining standard fiber *PM850*

from *Thorlabs* with a mode size of 3.6 μm. These components are installed on a transportable breadboard with a dimension of 300 mm $\times$ 500 mm, as shown in Figure 3.4. The fiber output is installed on a separate transportable breadboard with a dimension of 200 mm $\times$ 130 mm as illustrated in Figure 3.5. A fiber collimator *F220APC-1064nm* and a mode matching lens are

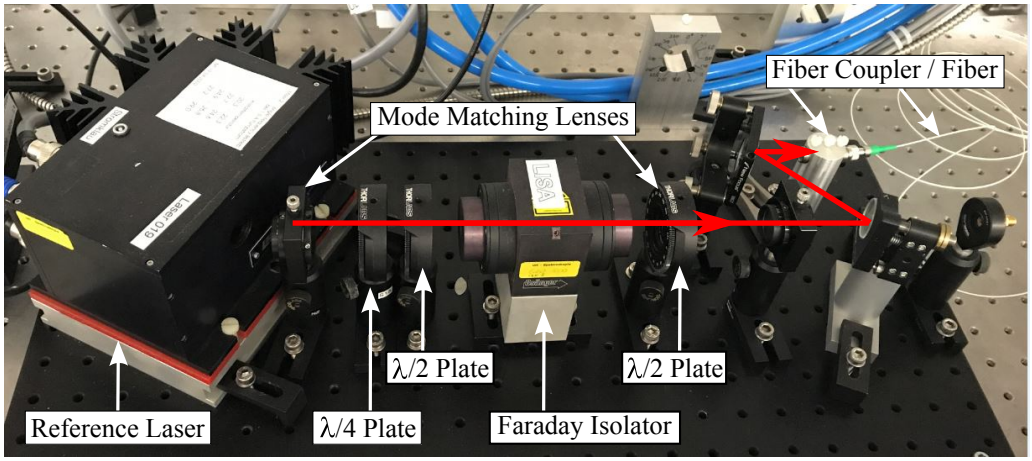

Figure 3.4: Photograph of the breadboard for the fundamental laser used for the second harmonic stage. The red line depicts infrared fundamental light from the Reference Laser coupled into the fiber.

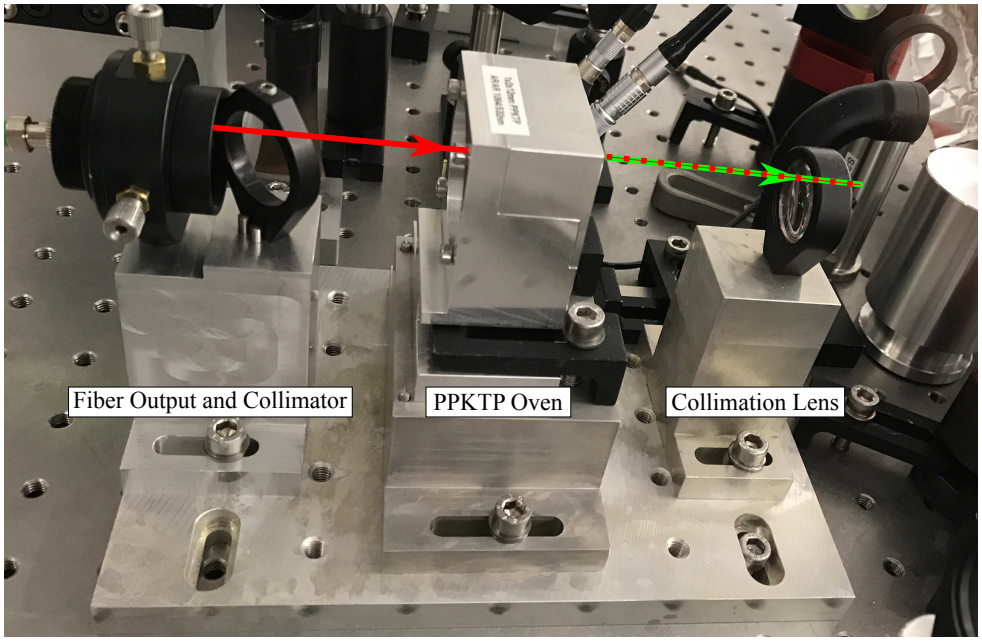

Figure 3.5: Photograph of the breadboard for the oven of the nonlinear crystal. The solid red line depicts infrared light from the Reference Laser injected to the PPKTP crystal to generate the second harmonic of its fundamental field, which is denoted by the green lines. The dashed red line represents the residual fundamental light after passing through the PPKTP crystal.

attached to the output of the fiber to mode match the beam to the nonlinear crystal. To be able

to align the beam to the crystal, these components are mounted in an adjustable x-y lens mount.

Nonlinear crystal and phase matching oven

A periodically poled potassium titanyl phosphate (KTiOPO4, PPKTP) crystal is used as the nonlinear medium. With this type of crystal, nonlinearities of up to $d_{eff} = 10\ \frac{\mathrm{pm}}{\mathrm{V}}$ can be achieved [43, 44], which allows high conversion efficiencies. The crystal used is from *Raicol Crystals* with a dimension of 1 mm $\times$ 2 mm $\times$ 12 mm and a corresponding periodicity of 9 μm. Since this type of crystal are phase matched at an elevated temperature, the PPKTP crystal is installed in an oven similar to those used for squeezed light sources [45, 46]. A thermoelectric cooler (TEC) [47] is used to control the phase matching temperature of the crystal. The crystal temperature is determined by reading the resistance of an negative temperature coefficient thermistor (NTC). The oven is mounted on the same transportable breadboard as the fiber collimator.

Optimal waist size according to Boyd-Kleinman

The waist size of 27 μm, for optimal conversion efficiency, is calculated according to the Boyd-Kleinman focusing condition [48]. The mode matching of the Reference Laser beam to the PPKTP crystal is therefore performed based on this condition. Since the waist size is essential for a high conversion efficiency, a measurement is performed to confirm its correct size as shown in Figure 3.6. The beam size is measured with a WinCam camera (CCD) at several positions

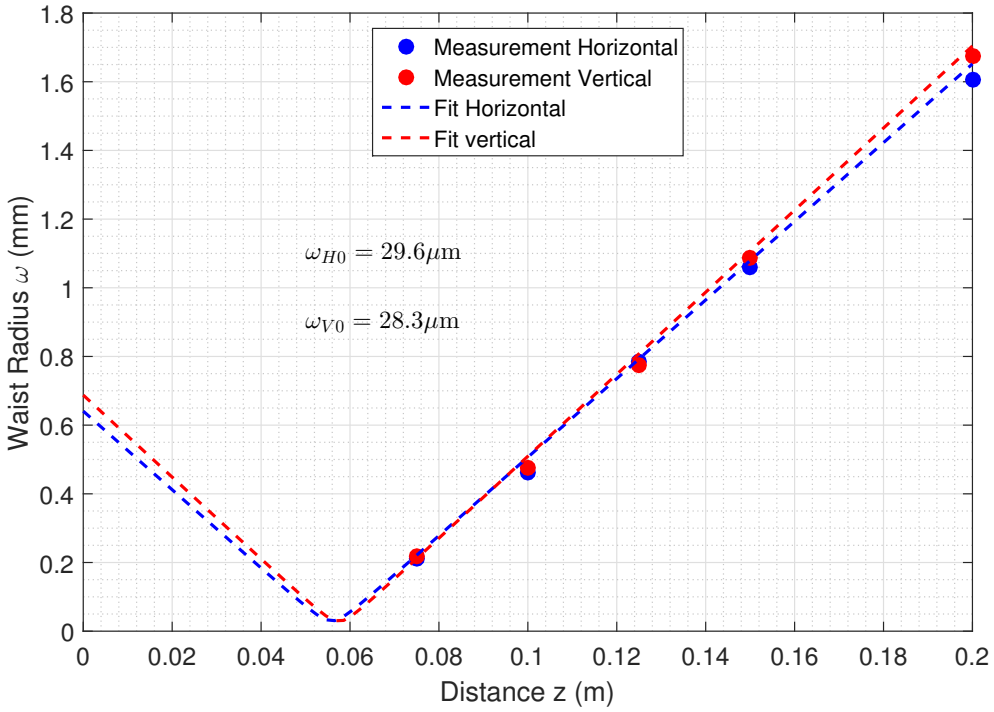

Figure 3.6: Measurement of the focused waist size of the fundamental beam. ω_{H0} and ω_{V0} represent the waist size in horizontal and vertical plane, respectively, and are in agreement with the expected waist size.

along the propagation direction. The measurement is performed without the nonlinear crystal and the exit of the collimator is the reference point for the measurement. A Gaussian fit is applied to the data to determine the corresponding size. As can be seen from the measurement, the waist size is determined to be $(29.6 \pm 2)\mu$m and $(28.3 \pm 2)\mu$m for the horizontal and vertical plane, respectively, which is in agreement with the expected value.

Phase matching temperature

The measured waist is located in the center of the PPKTP crystal, which is placed in the above-mentioned oven. To find an optimal phase matching condition, its temperature is varied and the corresponding harmonic power is measured at a fundamental power of 50 mW. As can be seen from the measurements shown in Figure 3.7, the optimal phase matching temperature is $\approx$ 32°C (corresponding NTC resistor $\approx$ 64 kΩ).

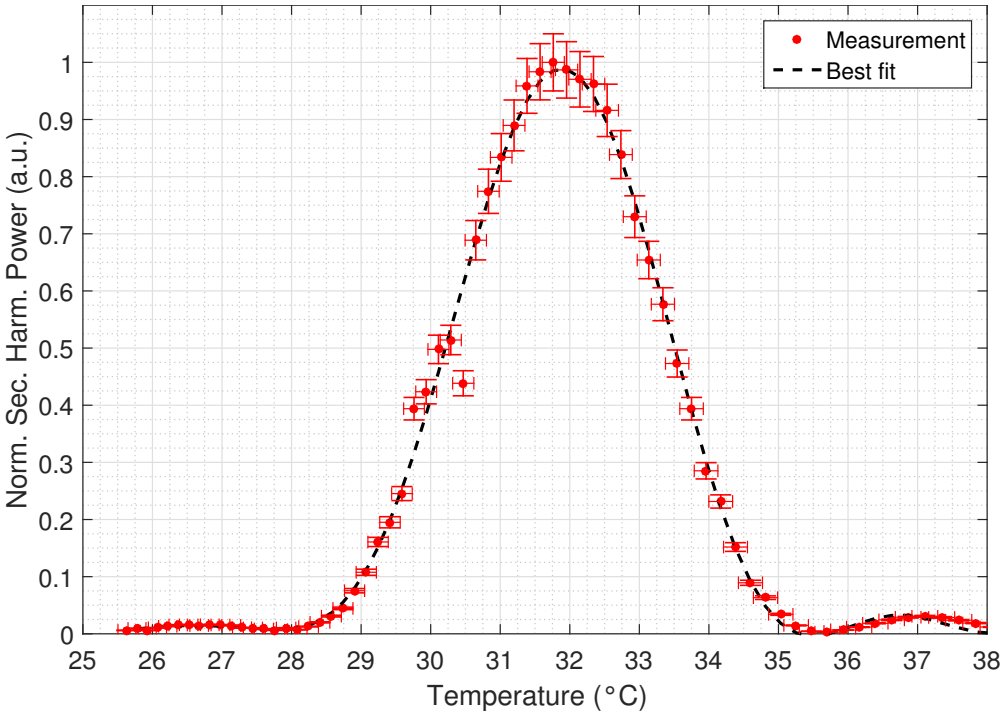

Figure 3.7: Normalized second harmonic power vs. temperature of the PPKTP crystal to determine the optimum phase matching condition. The data are fitted with a $sinc^2$ function.

Conversion efficiency

As can be seen from Figure 3.8, the designed stage provides a harmonic power of $\approx$ 380 μW at a fundamental power of 135 mW, which corresponds to a conversion efficiency of $\approx$ 0.3 %. This measurement is performed with the waist size and the phase matching temperature mentioned above.

Beam shape

Since the harmonic beam is enhanced inside the Regeneration Cavity, it is important to have

a good spatial beam quality. This means that the power in the fundamental TEM00 mode of

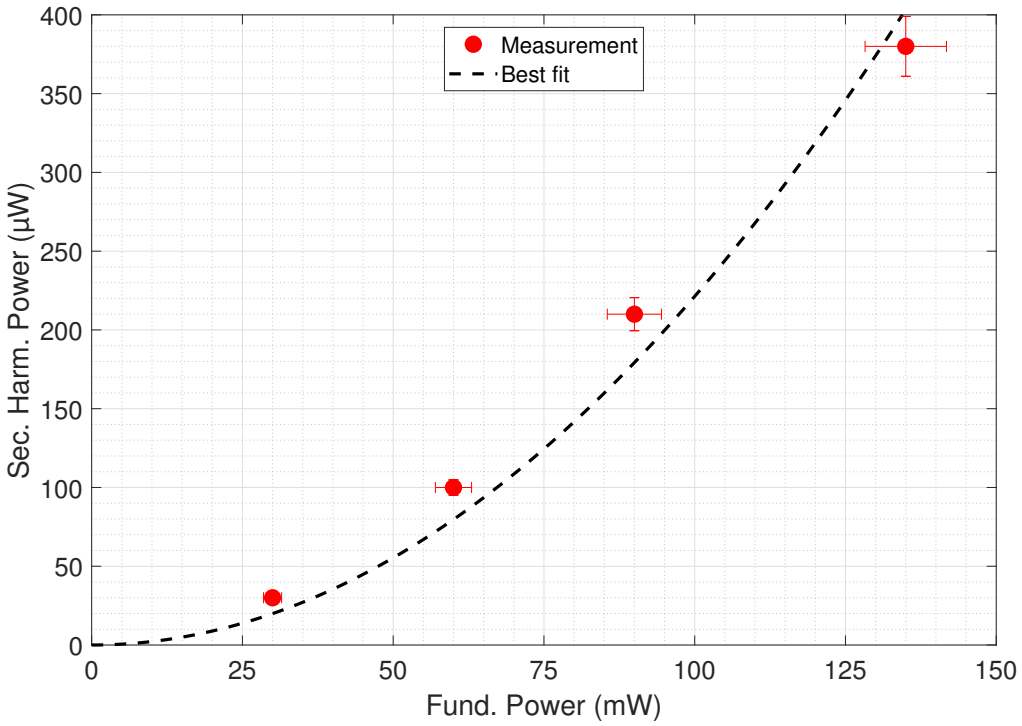

Figure 3.8: Second harmonic power as a function of the fundamental power. The error bars correspond to the standard deviation of the measurement. A fit, according to [48], with a nonlinear coefficient of $d_{eff} \approx 7 \frac{\text{pm}}{\text{V}}$ is applied to the measurement.

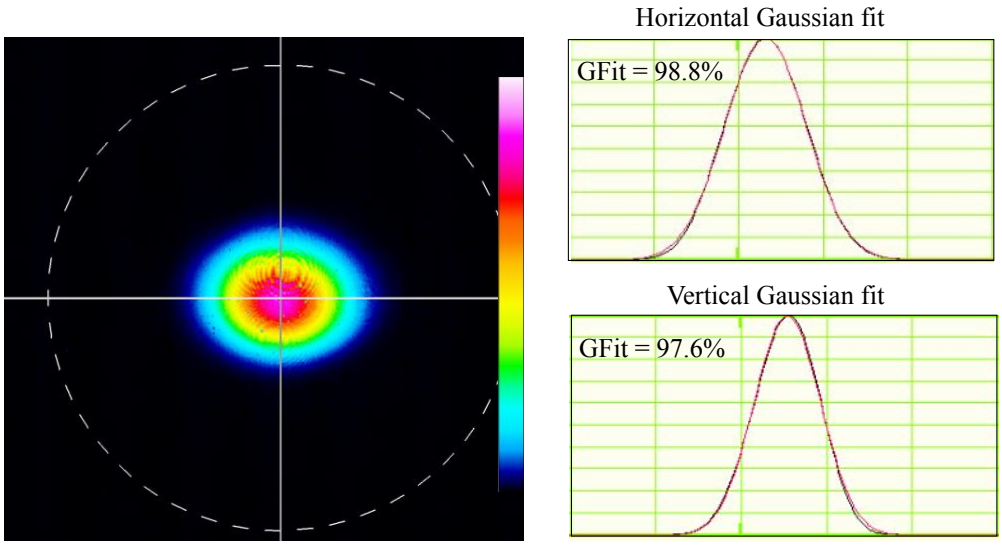

Figure 3.9: Intensity profile of the generated harmonic beam. The left part is a two dimensional profile with the CCD. The right part is a Gaussian fit to the horizontal and vertical data along the white planes. The ring-like patterns are measurement artifacts and are not part of the intensity profile.

the second harmonic beam should be as high as possible. A WinCam CCD is used to measure

the lateral intensity profile. The result is shown in Figure 3.9. The measurement shows a high quality beam with a Gaussian fit of G = 98.8 % and G = 97.6 % for the horizontal and vertical plane, respectively. The definition of the fit parameter G can be taken from the publication of the WinCam manufacturer [49].

This second harmonic stage is used to stabilize the frequency of the Reference Laser to the resonance frequency of the Regeneration Cavity and to interrogate the Regeneration Cavity. The corresponding experiments are described in Chapter 5.

3.3 Central Optical Bench

An essential component of the ALPS 1m-prototype and ALPS II is the *Central Optical Bench*. The two planar mirrors of the cavities and the quadrant photodiodes for monitoring the eigenmode position of the cavities are mounted on this bench. As discussed in Chapter 2, ALPS II aims to achieve a mode overlap of 90 % between the Production and Regeneration Cavity, which can only be achieved if the tilt angle between the planar mirrors does not exceed 5 μrad. This requirement demands precise alignment and high long-term stability of these mirrors. In order to achieve the anticipated mode overlap, similar demands are also placed on the stability of the quadrant photodiodes. To meet these requirements, two mounting methods are considered for the planar mirrors. The first method uses the high quality plane surface of the Central Optical Bench, while the other method is based on conventional adjustable mirror mounts. Also for the quadrant photodiodes special mounts are designed to meet the requirements. These mounting methods are briefly explained in the following sections.

3.3.1 Mechanical design

The Central Optical Bench used in the 1m-prototype is identical to the one described in the ALPS II technical design report [27]. It is made of a rolled ALPLAN, which is an alloy of aluminum, manganese and magnesium. The bench has a length of 525 mm along the main optical axis and a width of 370 mm. To support it with custom-made mounts, it is equipped with three 'ears' as shown in Figure 3.10. According to the optical design, threaded holes are drilled at appropriated positions on its surface to fix cuboid optical components on it with specially designed mounts. For the alignment of the optics in yaw, holes are provided which can be equipped with registration pins. On the side of the Regeneration Cavity, a groove is milled for a shutter, which can be used to prevent the transmitted beam of the Production Cavity from entering the Regeneration Cavity.

The pitch alignment of the optics on the Central Optical Bench is based on two conditions, namely the high planarity of the Central Optical Bench and the best-effort rectangularity be-

tween the bottom surface and highly reflective coated surface of the optic substrates. The

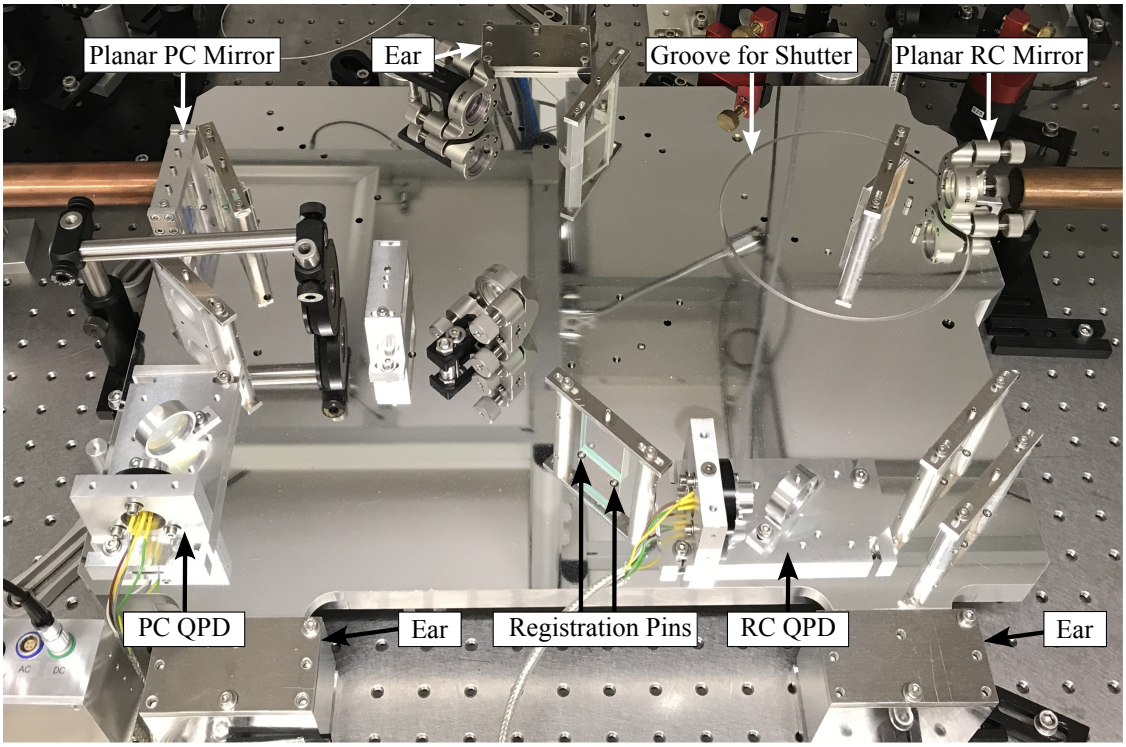

Figure 3.10: Photograph of the Central Optical Bench with assembled optical components.

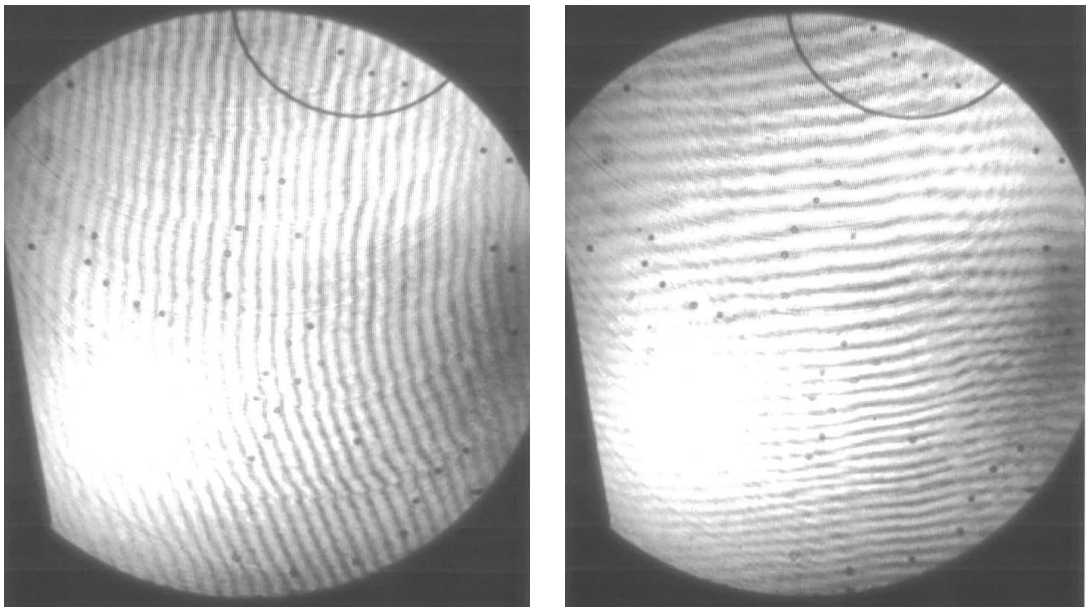

Figure 3.11: Planarity of the Central Optical Bench in longitudinal (left) and transverse (right) direction.

surface of the Central Optical Bench is milled by the company *ZEISS* with a diamond milling machine and the corresponding surface planarity is measured by interferometric methods [50]. Figure 3.11 shows a section of the planarity of the Central Optical Bench in longitudinal and

transverse planes, which has a planarity of 1.5 μm and 0.4 μm, respectively. The optical substrates on the central optical axis are provided by the company *Laseroptik* and are specified to have a best-effort rectangularity between the bottom surface and the highly reflective coated surface. Their bottom is also provided with a high planarity of $< \lambda/10$ at 633 nm.

Due to these facts, the required parallelism of the two planar cavity mirrors in pitch is automatically achieved by placing the substrates on the Central Optical Bench surface. To confirm the feasibility of this concept, some experiments are performed, which are described in Chapter 4.

3.3.2 Mirror mounts

Π-shaped frame for cuboid planar cavity substrates

The optical components are placed on the top of the Central Optical Bench and fixed with custom-made mounts. The planar mirror of the Production Cavity is fixed with a specially designed Π-shaped frame for cuboid optics with dimensions of 50 mm × 50 mm × 15 mm. As

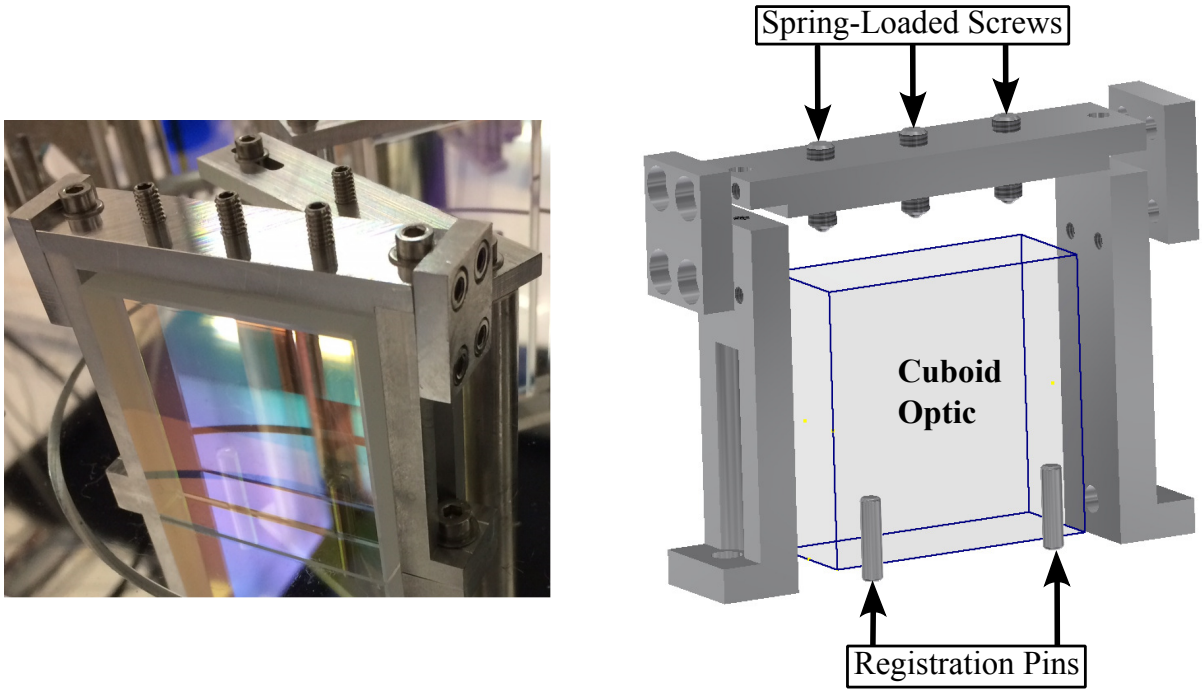

Figure 3.12: Photograph (left) and 3D technical drawing (right) of the Π-shaped frame for cuboid substrates.

can be seen from Figure 3.12, the frame is screwed onto the Central Optical Bench and fixes the substrate from the top with three spring-loaded screws. The force exerted by each screw is indicated to be 8.5 N and 14 N at the beginning and the end of its 0.8 mm stroke range. These screws are threaded in up to about half of the available stroke range. Registration pins are used

to correctly position the substrates in yaw. The pitch is defined, as described before, by the best-effort rectangularity of the substrates and the high planarity of the Central Optical Bench.

The optics between the two planar cavity mirrors, M4 and M8, on the main optical axis (40 mm × 40 mm × 10 mm) and the off-axis optics (40 mm × 30 mm × 10 mm) are also clamped with a similar configuration and their alignment in pitch and yaw are based on the same concept.

Commercial mirror mount for circular optics

The second mounting scheme is a commercial highly-stable *Polaris K1T* mount from *Thorlabs* designed for one inch circular mirrors, which is shown in Figure 3.13. The advantage of this

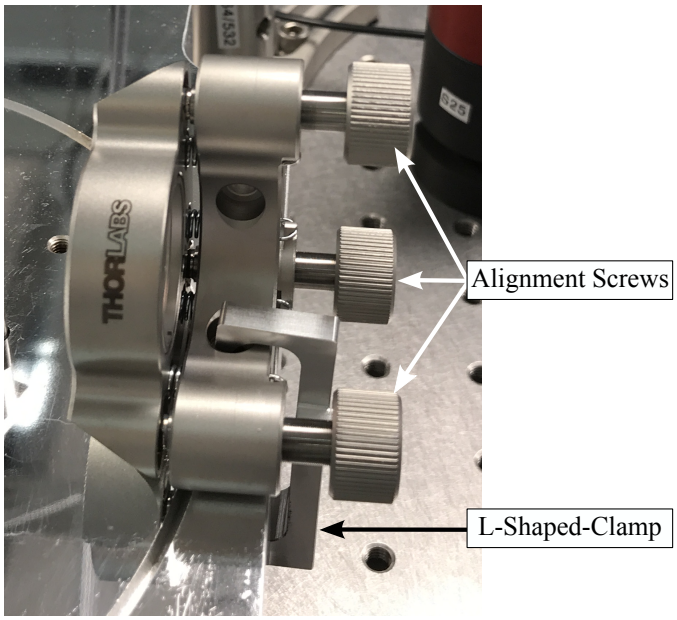

Figure 3.13: Photograph of the used polaris-mout, which is clamped to the Central Optical Bench.

alternative mounting scheme is the availability of alignment screws that simplifies the alignment of the optical components in yaw and pitch. Since it is considered as an alternative for ALPS II, it is used in the prototype to test its stability. This mount is used for the planar mirror of the Regeneration Cavity and for the alignment of the Reference Laser beam for the PLL path (M6 and M10). Since the Central Optical Bench is not designed for such mounts, the mount is fixed on it with an L-shaped clamp.

The feasibility of alignment and the long-term angular stability, with respect to ALPS II requirements, of this mount is tested and compared to the Π-shaped frame in Chapter 4.

3.3.3 Mechanical design of the quadrant photodiodes

Another crucial parameter for the power overlap between both cavities is the lateral displacement of the two eigenmodes. ALPS II aims to use quadrant photodiodes to monitor the eigenmode locations. The mounting scheme for theses quadrant photodiodes is similar to the concepts used for power stabilization in Advanced Virgo [51] and is illustrated in Figure 3.14. The quadrant photodiode is clamped between a baseplate and a cap with screws. The assembly can be moved on a xy-plate for alignment purposes. Once the quadrant photodiode is aligned, the assembly can be fixed to the xy-plate by screws from the back side. An adapter plate is used to mount the entire assembly to the Central Optical Bench.

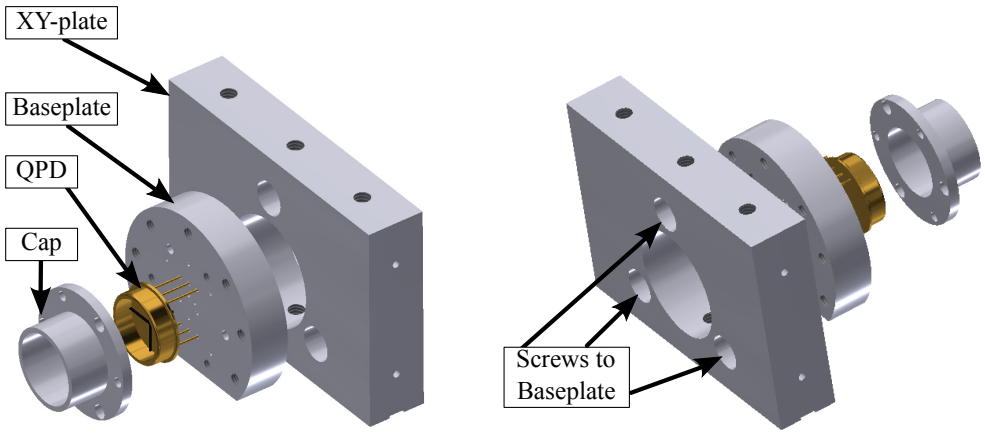

Figure 3.14: Assembly of the used quadrant photodiode. The assembly is mounted to the Central Optical Bench via an adapter plate (not shown).

In Chapter 4, some experiments are performed to verify the stability of this mounting concept with respect to the ALPS II requirements.

3.4 Design of the Production Cavity

The Production Cavity is designed and assembled in a plano-concave configuration. Its curved mirror, M_{PCI}, has a diameter of two inches, a radius of curvature of 10 m, and a reflectivity of 99 % at 1064 nm. The mirror is glued to a PZT (*Physik Instrument, S-315.10*) mirror mount that is in turn placed on a pitch and yaw platform (*PY004/M*) from *Thorlabs* as illustrated in Figure 3.15. This platform is used for coarse alignment of the cavity eigenmode to avoid saturating the fine-tuning range of the PZT. The PZT has three controls elements, which are arranged in intervals of 120° and can be controlled individually. The elements are controlled by matrix amplifiers, so that pure movement in pitch, yaw, and z is possible. The tuning and calibration of the actuator and the matrix amplifier are described in Chapter 4.

The planar mirror, M_{PCO}, has a cuboid design with dimensions of 40 mm × 40 mm × 10 mm and is installed on the Central Optical Bench, which is spaced 1 m apart from the curved mirror. Its specified reflectivity is 99 % at 1064 nm, which forms an impedance-matched cavity with the curved mirror. Since the Production Cavity is operated in air, a metal tube is placed with small gaps between the curved and planar mirror to minimize the effect of air fluctuations on the cavity.

The corresponding designed parameter of the cavity are listed in Table 3.1. In addition, the

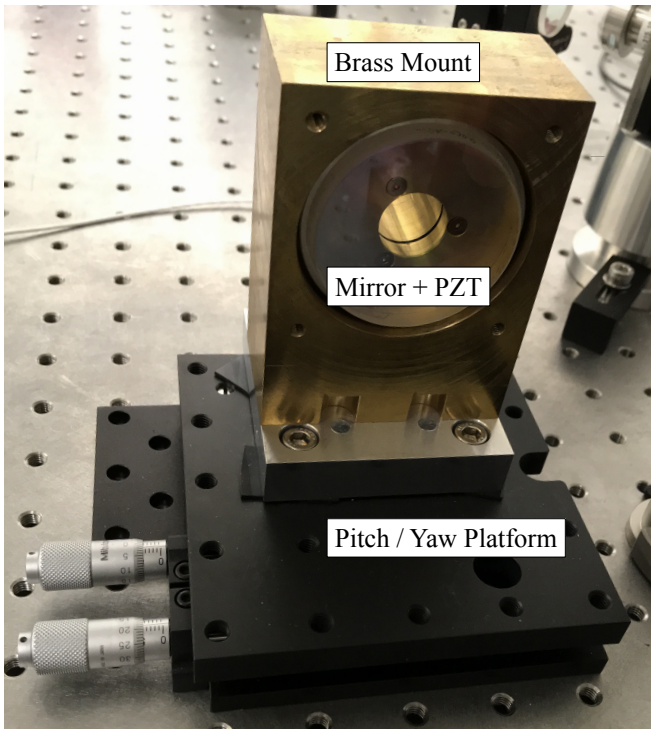

Figure 3.15: Photograph of the used actuator assembly for the Production Cavity.

Table 3.1: Designed and measured parameter of the 1m-prototype Production Cavity.

Parameter	Designed	Measured
Length [L]	1 m	1 m
Radius of curvature [ROC]	10 m	
Free spectral range [FSR]	150 MHz	(146 ± 5) MHz
Finesse [$\mathbb{F}$]	312	(269 ± 26)
Line-width	480 kHz	(562 ± 50) kHz
Waist radius [$\omega_{0,eig}$]	1 mm	(1.04 ± 0.05) mm
Half divergence angle [$\theta_{0,eig}$]	339 μrad	
Rayleigh range [Z_R]	3 m	

measured values for the finesse $\mathbb{F}$, the line-width, the waist radius $\omega_{0,eig}$ and the free spectral range FSR are given. The line-width and the finesse are determined by performing a mode scan

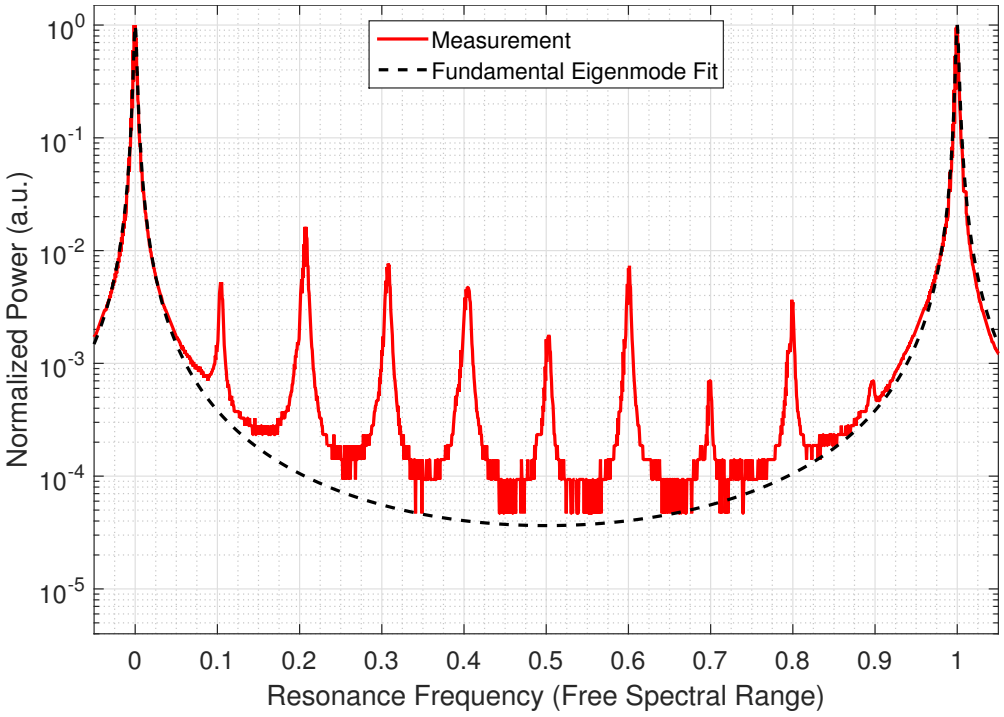

Figure 3.16: Single-trace of the cavity eigenmode scan of the Production Cavity to determine the finesse and line-width of the cavity.

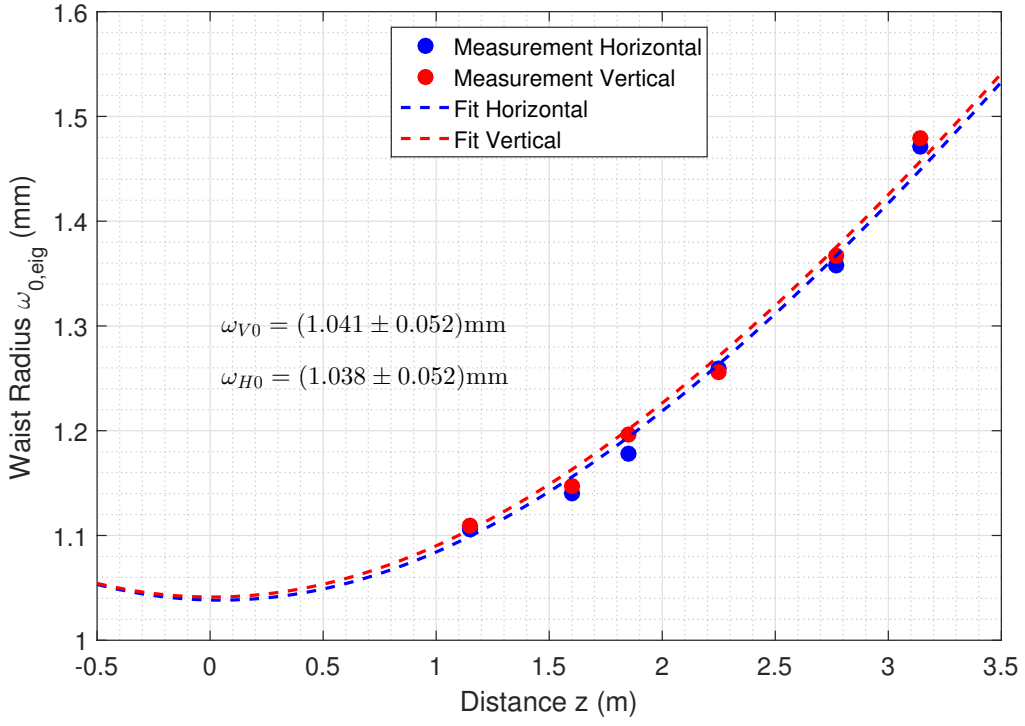

Figure 3.17: Measurement of the waist radius of the Production Cavity. ω_{H0} and ω_{V0} represent the waist radius in horizontal and vertical plane respectively.

in eigenmode basis of the Production Cavity and applying a fit to the measured fundamental mode as shown in Figure 3.16. The specified error is the standard deviation of the averaged

measurement. For the determination of the free spectral range, the imprinted sidebands are used as a reference to determine the frequency spacing between the fundamental modes in the mode scan. To determine the waist radius, the beam size is measured with a WinCam at several positions along the propagation direction and a Gaussian fit is applied to the data to determine the corresponding size, as shown Figure 3.17. These measured values are used for all following calculations.

3.5 Design of the Regeneration Cavity

The Regeneration Cavity is also assembled in a plano-concave configuration similar to the Production Cavity. Its curved mirror, M_{RCI}, has the same diameter and radius of curvature as the curved mirror of the Production Cavity. The length actuator is also assembled in the same configuration. Since it is used as a dual resonant cavity for 1064 nm and 532 nm, the mirror is dichroically coated with a specified reflectivity of 99 % for both wavelengths.

The planar mirror, M_{RCO}, has a circular substrate with a diameter of one inch and is placed on the Central Optical Bench, which is also 1 m away from the curved mirror. It is coated to have a specified reflectivity of 97 % at 532 nm and 25 ppm losses at 1064 nm, which results together with the curved mirror in an under-coupled and over-coupled cavity for 1064 nm and 532 nm, respectively. The substrate is chosen to be circular to test the mounting scheme described in Section 3.3. It is mounted in the commercial mount, which is clamped to the Central Optical Bench. Since the Regeneration Cavity is also operated in air, a metal tube is placed between the curved and planar mirror to minimize the effect of air fluctuations on the cavity, as can be seen in Figure 3.1.

In Table 3.2 the relevant designed and measured cavity parameter for both wavelengths are listed. The measured parameter are determined in analogy to the parameter for the Production Cavity described in the previous section.

Table 3.2: Designed and measured parameter of the 1m-prototype Regeneration Cavity.

Parameter	1064 nm (Designed / Measured)	532 nm (Designed / Measured)
Length [L]	1 m / 1 m	1 m / 1 m
Radius of curvature [ROC]	10 m	10 m
Free spectral range [FSR]	150 MHz / (147 $\pm$ 1.5) MHz	150 MHz / (147 $\pm$ 1.5) MHz
Finesse [$\mathbb{F}$]	623 / (553 $\pm$ 65)	102 / (101 $\pm$ 6)
Line-width	240 kHz / (273 $\pm$ 33)kHz	1.47 MHz / (1.45 $\pm$ 0.06) MHz
Waist radius [$\omega_{0,eig}$]	1 mm / (1.02 $\pm$ 0.05) mm	10.7 mm / (0.71 $\pm$ 0.04) mm
Half divergence angle [$\theta_{0,eig}$]	339 μrad	241 μrad
Rayleigh range [Z_R]	3 m	3 m

Another essential parameter for the Regeneration Cavity is the frequency offset between the

infrared field of the Production Cavity and the second harmonic field of the Reference Laser within the Regeneration Cavity. The ratio between the two frequencies is not an integer factor of two, which is due to different penetration depth of the fields into the dichroic mirror coating. As can be seen in Figure 3.18, this offset is determined to be $\approx 18\,\mathrm{MHz}$ (≈ 0.12 of the green free spectral range) for the prototype Regeneration Cavity. However, since this effect is related to temperature, the offset frequency varies between 10 MHz and 50 MHz corresponding to the temperature fluctuations of the mirror. This information is used in Chapter 5 to perform a dichroic lock of the Regeneration Cavity.

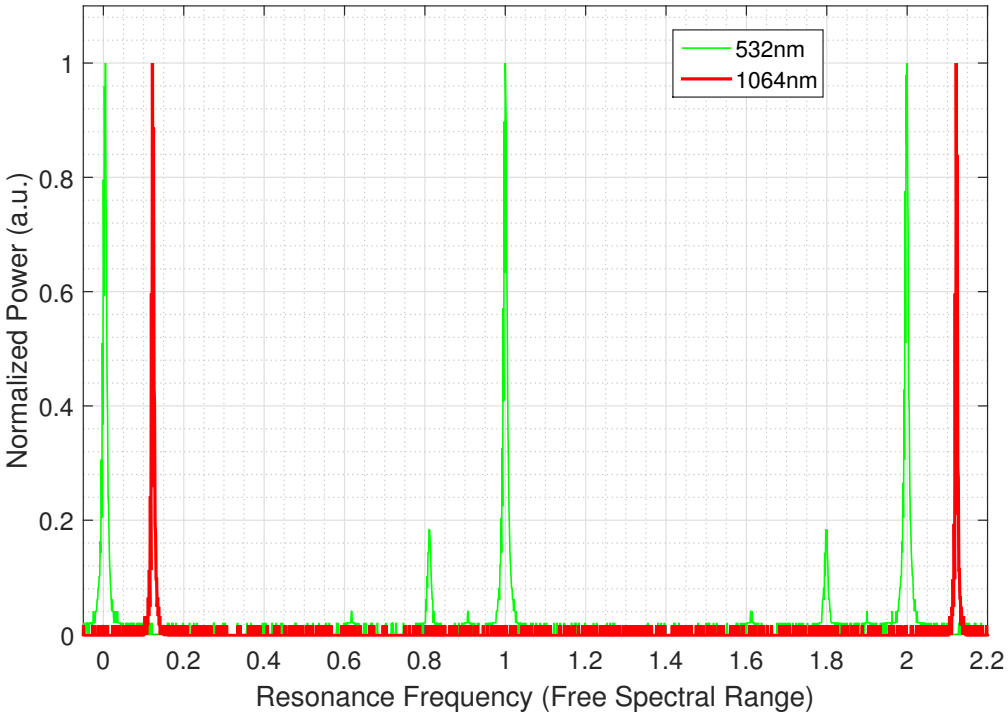

Figure 3.18: Mode scan of the Regeneration Cavity while the Production Cavity and the second harmonic filed of the Reference Laser are resonant in the cavity.

This setup is used in Chapter 4 to test and verify the described concept of the Central Optical Bench. Furthermore, it is used in Chapter 5 to demonstrate the entire frequency and length stabilization concept of ALPS II.

Chapter 4

Demonstration of the Central Optical Bench concept

As described in the previous chapter, ALPS II anticipates mounting the planar cavity mirrors and the associated quadrant photodiodes (QPDs) for the detection of the eigenmode positions on a Central Optical Bench. For the planar mirrors two different mounting concepts, each with its own advantages, are considered. The quadrant photodiodes are targeted to be mounted in custom-made mounts. The corresponding long-term stability with respect to the ALPS II requirements needs to be proven. Therefore, the miniaturized 1m-prototype test bed, described in previous Chapter 3, is used to perform several experiments to test the stability of this mounting concepts, which are described in this chapter. Section 4.1 of this chapter describes an autocollimator-assisted alignment concept to achieve the desired parallelism of the planar cavity mirrors with respect to each other. Furthermore, a long-term measurement concerning mirror-mount stability using the autocollimator is discussed. Section 4.2 shows an experiment in which the Production Cavity is spatially overlapped with the Regeneration Cavity. This experiment is performed to additionally prove the autocolimator-assisted measurements of the parallelism. The concluding Section 4.3 describes the readout verification of the quadrant photodiodes and their long-term performance concerning drifts.

4.1 Parallelism measurement with an autocollimator

In this section, the parallel alignment of the planar mirrors and the corresponding measurement on the long-term stability of their mounting concepts using the autocollimator are discussed. For a better understanding of these measurements, the operating principle and the operation modes of the autocollimator are briefly explained. Subsequently, the characterization of the mounting concepts and the results obtained are discussed.

4.1.1 Functional principle of the autocollimator

Measurement of the tilt angle

The autocollimator used is an electronic one with the designation *TriAngle TA300-57* from the manufacturer *TRIOPTICS*. It has a focal length of 300 mm and a free aperture of 50 mm. The operating wavelength is 530 nm. The used CCD detector has an image size of 780 × 570 pixels with a corresponding pixel size of 8.25 μm. Its diffraction limited resolution is

$$\beta = 1.22\frac{\lambda}{D} = 13\,\mu\text{rad}, \tag{4.1}$$

where λ is the operational wavelength and D is the free aperture [52]. The operating principle of the autocollimator for measuring tilt angles is illustrated in Figure 4.1 [53]. The image of an illuminated object reticle is located in the focal spot of an objective lens. The beam is reflected

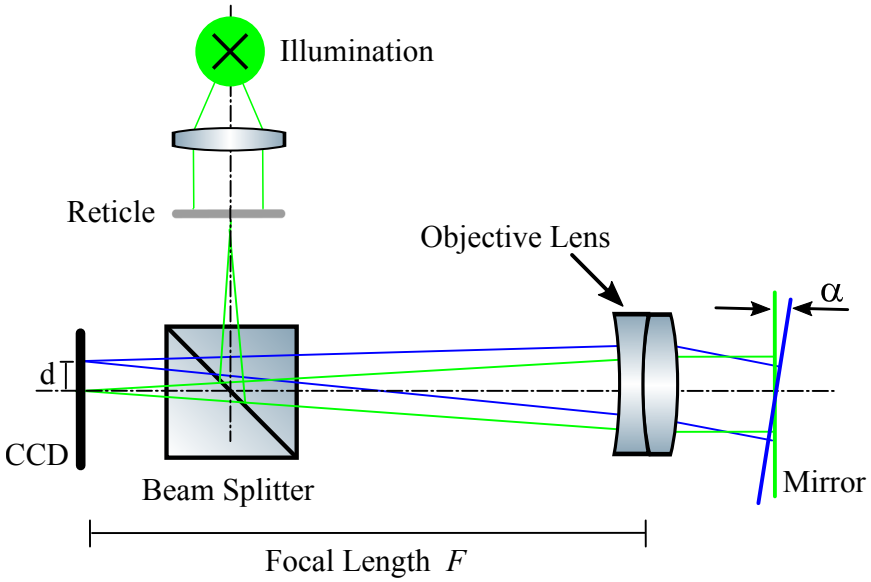

Figure 4.1: Functional principle of an autocollimator for measuring tilt angles. A slight alteration of the angle between the optical axis of the objective lens and the mirror causes a tilt of the collimated beam, which results in a different image position on the CCD detector.

by a beam splitter and then collimated by the objective lens. At a finite distance, the collimated beam is reflected by a mirror surface, which is then imaged on the object plane of the objective lens. When the mirror surface is tilted by an angle α, with respect to the optical axis, the reflected beam enters the objective lens at an angle of 2α. This results in a shift d of the image on the CCD. Assuming small tilts, the relationship between the angle α and the shift d can be approximated as follows [54]:

$$\alpha = arctan\left(\frac{d}{2F}\right) \approx \frac{d}{2F}, \tag{4.2}$$

where: d is the shift on the CCD and F is the focal length. The shift d is determined by computer-assisted image analysis of the CCD camera image. For this purpose, the center of mass for the intensity profile of the image is determined with a sub-pixel resolution and compared with a defined reference. With this sub-pixel method, the center of mass can be determined with an accuracy of $\approx 3.5\,\mu$rad [53]. This measuring principle is used for the alignment of the planar cavity mirrors and for investigating their long-term characteristics, as described in Section 4.1.2 and 4.1.3.

Measurement of the wedge angle

Another valuable measurement method provided by the autocollimator is the determination of wedge angles for wedged substrates. Its principle is shown schematically in Figure 4.2. Similar to tilt angle measurements, the beam reflected by the mirror surface is shifted if a

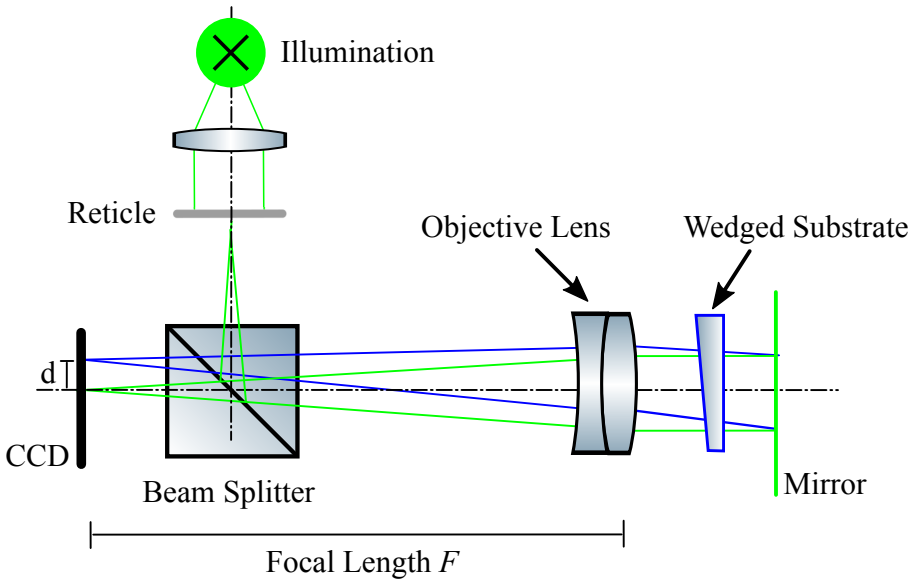

Figure 4.2: Functional principle of an autocollimator for measurements of wedge angles.

wedged substrate is located between the mirror and the objective lens. The resulting relationship between the shift d and the wedge angle δ is given by

$$\delta = \frac{d}{2\,(n-1)\,F}, \tag{4.3}$$

where n is the refractive index of the wedged substrate [53]. With the sub-pixel method mentioned previously, the wedge angle can also be measured with an accuracy of $\approx 3.5\,\mu$rad. Wedge angles $> 5\,\mu$rad for the optical components that are located on the Central Optical Bench between the two cavity mirrors would laterally shift the beam and limit the desired spatial overlap of both cavities. This would also be the consequence if the planar cavity mirrors have wedge angles $> 5\,\mu$rad. Therefore, the autocollimator is used in the described manner to measure the wedge angle of these substrates, as described in Section 4.2.

4.1.2 Custom-made Π-shaped mounts for cuboid mirrors

The first parallelism measurement is performed with custom-made mounts and cuboid cavity mirrors. This mounting scheme is based on the concept described in Chapter 3 and [27, 55]. The purpose of this measurement is to prove the feasibility of the alignment concept and the long-term stability of the mounts. The substrates of the used mirrors have a dimension of 50 mm × 50 mm × 16 mm (IBS coated) and their bottom surfaces are provided with a high planarity. They are specified to have a best-effort rectangularity (90°) between their bottom surface and the highly-reflective coated surface, as described in the previous Chapter 3. The combination of these mirrors and the described mounts has the advantage that the mirrors can be placed and mounted directly on the surface of the Central Optical Bench. As described previously, the pitch alignment is based on high-planarity of the Central Optical Bench and the rectangularity of the mirror substrates. Throughout the experiments, however, it is found that during the coating process of the mirrors, coating material also spilled on the flat bottom surface of the mirrors, which nullify the rectangularity of the mirrors and thus changes the alignment in pitch. Furthermore, the very hard coating material on the bottom side of the mirrors scratches the flat surface of the Central Optical Bench while aligning the yaw. In order to still achieve the required parallelism, single layers of aluminum foil with a thickness of 0.2 μm are used. Small pieces of this aluminum foil are placed at one side of the mirror between the bottom surface of the mirror and the Central Optical Bench. In order to measure the long-term stability, the Regeneration Cavity mirror is placed in the intended position by means of the registration pins. The mirror is fixed to the Central Optical Bench from the top with three of the previously mentioned spring-loaded ball-tip screws with an estimated applied force of ≈ 11 N per screw.

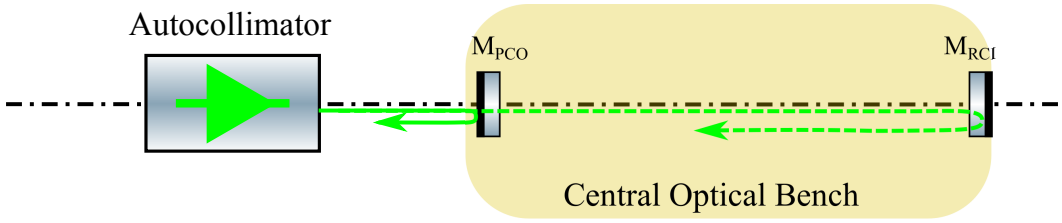

Figure 4.3: Schematic illustration of parallelism-measurement using the autocollimator. The Regeneration Cavity mirror is fixed and defines the alignment reference for the Production Cavity mirror. Registration pins and pieces of aluminum are used to align the Production Cavity mirror to this reference.

The position of the Regeneration Cavity mirror is defined as alignment reference for the Production Cavity mirror using the autocollimator located on the side of the Production Cavity mirror, as depicted in Figure 4.3. Depending on the measurement method, the reflected beam with the highest intensity is always the reference beam for the autocollimator. Since the Regeneration Cavity mirror has a significantly higher reflectivity for the operating wavelength, it

is first used to define this reference for the autocollimator and then covered for the alignment of the Production Cavity mirror. The registration pins are used to align the Production Cavity mirror to the defined reference in yaw. However, due to manufacturing tolerances of the Central Optical Bench, it is not sufficient to use only the registration pins to obtain parallelism better than 5 μrad for the yaw. Therefore, these registration pins are used for rough alignment of the yaw, while fine-tuning alignment is performed manually with an accuracy of $< 5\,\mu$rad. For the pitch, aluminum foil is used to align the mirror with an accuracy $< 5\,\mu$rad. For the long-term stability, the Production Cavity mirror is then fixed on the Central Optical Bench in the manner described before. The autocollimator is used to register the position of the aligned mirror relative to the position of the Regeneration Cavity mirror. This position is sampled at 300 s intervals with an average of 100 samples over a period of $\approx$ 190 hours. The registered data are shown in Figure 4.4. The corresponding histogram is shown in Figure 4.5.

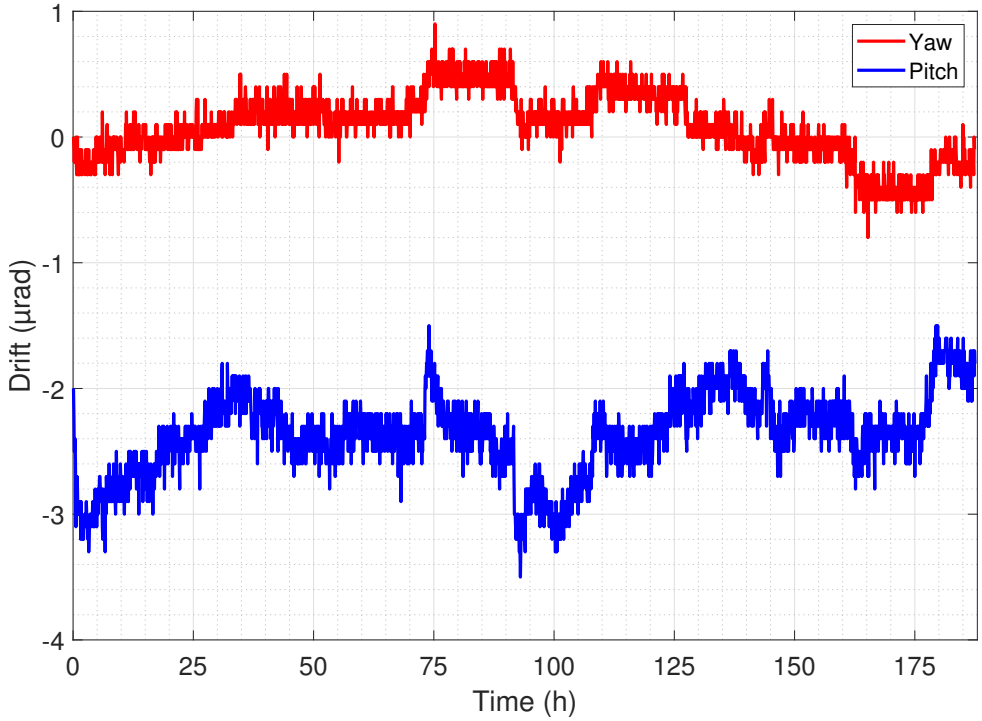

Figure 4.4: Autocollimator measurement time series on angular stability of Π-shaped frame. The data represent the angular position of the Production Cavity mirror in pitch and yaw relative to a defined reference. The peak-to-peak drift is $\approx 2\,\mu$rad for both pitch and yaw, which meets the ALPS II requirements.

Since the autocollimator always measures relative to the defined reference, a check is made at the end of the measurement to determine whether drifting of the Central Optical Bench itself occurs during the measurement. For this purpose, the Regeneration Cavity mirror is released and its position relative to the reference is measured. No drifts of the Regeneration Cavity are observed, so that it can be concluded that the measured drifts in Figure 4.4 are those of the

Production Cavity mirror relative to the defined reference. As can be seen from the Figures 4.4 and 4.5, the yaw is aligned to have an averaged parallelism of 0.1 μrad with a corresponding standard deviation of 0.3 μrad. The peak-to-peak drift is measured to be ≈ 2 μrad. Furthermore, it can be seen that occasionally an oscillation with a period of ≈ 16 h occurs. A correlation to humidity or temperature is suspected. However, since the measurement is in accordance with the ALPS II requirements, no further investigation is initiated. The pitch is aligned to have an

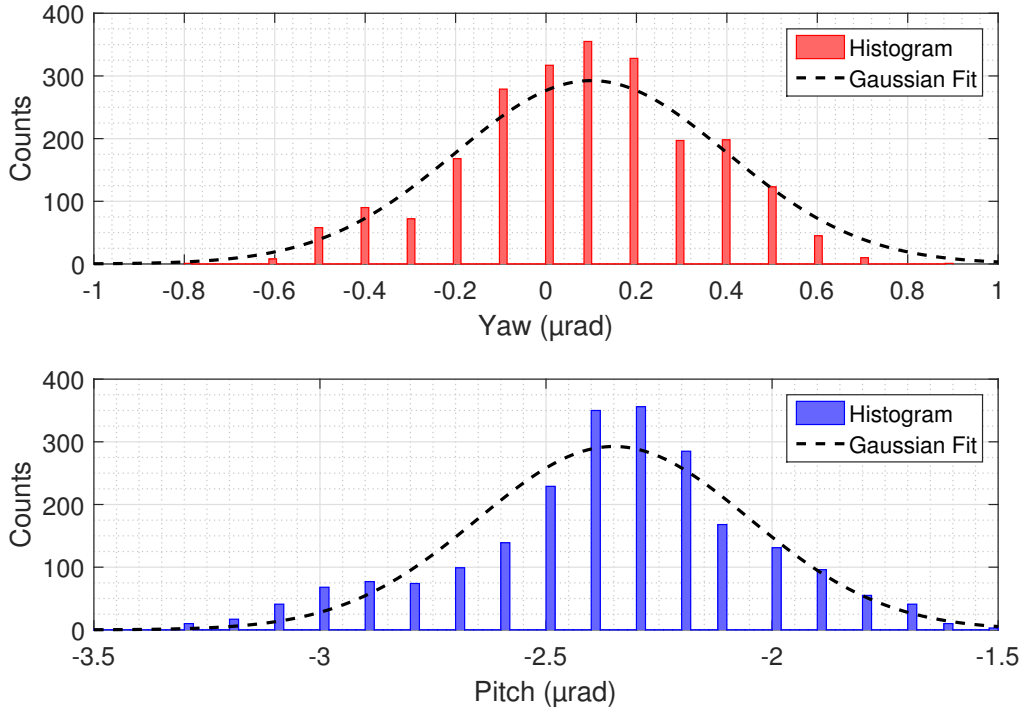

Figure 4.5: Histogram of the raw measurement data, which represents the mean value and the corresponding standard derivation of the angular reading for pitch and yaw for custom-made mounting frame. The bin width is 0.01 μrad.

averaged parallelism of ≈ -2.5 μrad with a corresponding standard deviation of 0.3 μrad. The sign is not of great importance since it only indicates whether the mirror position is above or below the defined reference position. The peak-to-peak drift is measured to be ≈ 2 μrad, which also meets the ALPS II requirements. There is also for the pitch a repeating oscillation with a period of ≈ 16 h. It is assumed that it refers to the same noise source as for yaw.

This measurement clearly satisfies the ALPS II requirements regarding long-term drifts. However, the corresponding alignment is very demanding and time-consuming. Therefore, an alternative mounting scheme is considered, which is described in the next Section 4.1.3.

4.1.3 Commercial mount vs. Π-shaped frame

As described in the previous chapter, the alternative mount is a commercial highly-stable mount with alignment screws from *Thorlabs* designed for circular substrates. To test its stability, the

cuboid Regeneration Cavity mirror is replaced by the circular mirror of the 1m-prototype and mounted in the polaris-mount as described in Chapter 3. A further modification, compared to the previous setup, is the replacement of the Production Cavity mirror by a dichroic (532 nm / 1064 nm, 30 mm × 20 mm × 10 mm) cuboid mirror. The reason for this modification is that the planar mirror used in the previous section is not specified to be used for the 1m-prototype. Because this Central Optical Bench will be used for the prototype later on, it is equipped with the mirrors of the prototype. Since both mirrors are highly-reflective for the operating wavelength of the autocollimator, is it not possible to observe both mirror surfaces simultaneously. Therefore, the planar Production Cavity mirror is installed laterally offset on the Central Optical Bench with respect to the optical axis, as depicted in Figure 4.6. This procedure allows simultaneous observation of both mirror surfaces with the autocollimator.

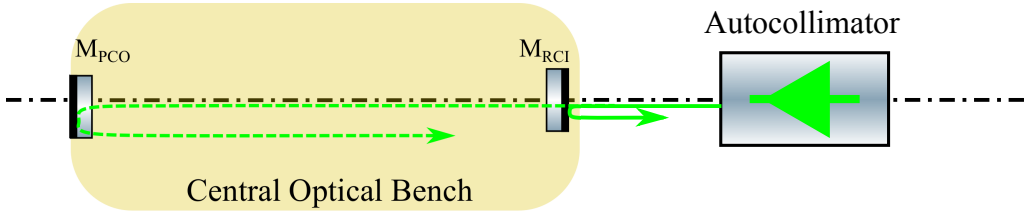

Figure 4.6: Schematic illustration of parallelism alignment of the planar Production Cavity mirror M_{PCO} and Regeneration Cavity mirror M_{RCO} using the autocollimator. The Production Cavity mirror is fixed by the Π-shaped frame and laterally offset with respect to the center axis of the Regeneration Cavity mirror. The lateral offset allows simultaneous detection of both mirror surfaces by the autocollimator.

The Production Cavity mirror is installed in the intended position by means of the registration pins and clamped to the Central Optical Bench. As described in the previous chapter, the Central Optical Bench is not designed for commercial mounts. Therefore, the polaris-mount is attached to the Central Optical Bench using an L-shaped clamp. Since only the long-term stability is of major interest for this measurement, the mirrors are not aligned to have the required ALPS II parallelism but an arbitrarily chosen one. To test the mounts for possible drifts, the position of both mirrors relative to each other is then registered over a period of 60 hours. In addition, the relative humidity and the temperature in the immediate vicinity of the setup are registered to identify possible correlations. The raw angle data of the autocollimator are sampled at 100 ms intervals. The relative humidity and temperature are registered every 10 minutes. Figure 4.7 shows the measured data and Figure 4.8 the histogram of the raw angle data for pitch and yaw.

Unlike ALPS II and the previous configuration in Section 4.1.2, this measurement is not performed in a quiet environment. Therefore, the data are additionally averaged over a period of ≈ 2 minute. To determine and calculate the correlation to relative humidity or temperature, the angular raw data are averaged in a second step to 10 minutes sampling periods. The 10 minutes average of the angular raw data is only used for the calculation of the correlation to

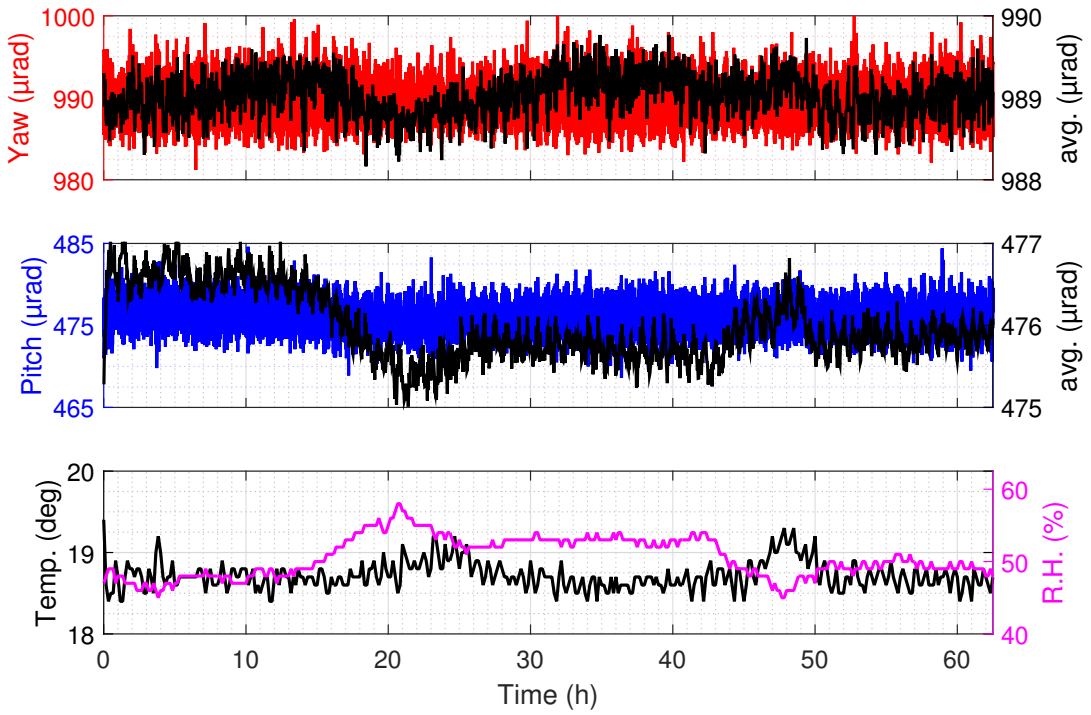

Figure 4.7: Autocollimator measurement time series on angular stability for polaris-mount and Π-shaped mirror frame. The left y-axis in the upper two plots shows the measured raw angle data while the right y-axis is used for a moving-average of 1000 data samples. In the lower plot the left y-axis represent the temperature while the right y-axis shows the relative humidity (R.H.).

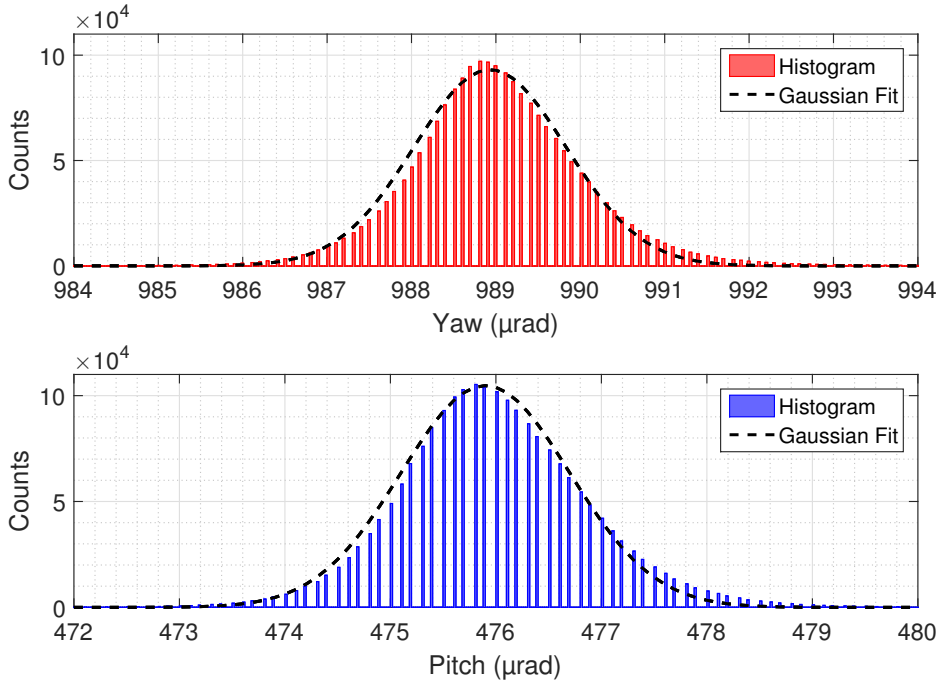

Figure 4.8: Histogram of the raw measurement data for pitch and yaw, which shows their mean value and the standard derivation σ of 0.8 μrad for pitch and 0.9 μrad for yaw.

humidity and temperature and is not shown in the Figure 4.7.

As can be seen from the data, the two-minutes moving-averaged measurement for yaw shows a drift of less than 2 μrad, which fully meets the requirements of ALPS II. The correlation to humidity and temperature is calculated as -0.14 and -0.13, respectively, which is negligible. For the pitch the two-minutes moving-averaged measurement also shows a peak-to-peak drift of $\approx$ 2 μrad, which also fully suffices the requirement. There exists a significant correlation of -0.74 between the relative humidity and the pitch-angle; the correlation to temperature, on the other hand, is negligibly small at -0.04. It is essential to emphasize that ALPS II is performed in vacuum. Therefore, the correlation to relative humidity is not particularly important and is not further investigated.

To verify this autocollimator-assisted measurement, an additional experiment is performed, which is described in Section 4.2.

4.1.4 Summary and conclusion

Π-shaped frame

An autocollimator is used to verify the alignment concept of the planar mirrors of the ALPS II cavities and to test the long-term stability of their custom-made mounts. Throughout the experiments, it is found that during the coating process of the mirrors, coating material also spilled on their flat bottom surface. This very hard coating material causes scratches on the planar surface of the Central Optical Bench and complicates the pitch alignment of the mirrors because it destroys their specified rectangularity. However, in order to allow for correct pitch alignment, aluminum foils with a thickness of 0.2 μm are used to compensate for this discrepancy. The autocollimator is then used to register the pitch and yaw angle of the aligned and clamped mirror over a course of $\approx$ 180 h. The measurement shows a peak-to-peak stability of $\approx$ 2 μrad per degree of freedom, which is in accordance with the ALPS II requirements. Despite difficulties, which are most likely due to this specific coating run of the mirrors, it can be concluded that the Central Optical Bench concept works. However, the corresponding alignment is very demanding and time-consuming. It is therefore worth considering commercial mounts as an alternative.

Polaris-mount

In a second attempt the stability of an alternative commercial mount designed for circular substrates is tested. A major benefit of this commercial mount is the availability of alignment-screws. These allow a much faster reproducible alignment in comparison to the custom-made mounts. This mount is clamped to the Central Optical Bench with custom-made clamps. A mirror is installed in it and its pitch and yaw angle is registered with the autocollimator over a course of $\approx$ 65 h. The measurement shows a peak-to-peak stability of $\approx$ 2 μrad per degree

of freedom, which fully satisfies the ALPS II requirements. Furthermore, the data show a humidity-correlated drift for pitch, which is not further investigated since ALPS II is performed in vacuum.

4.2 Spatial overlap of the Production and Regeneration Cavity

To verify the autocollimator-assisted measurement described in Section 4.1.2 and 4.1.3, an additional experiment is performed using the 1m-prototype described in Chapter 3. For this purpose, the frequency of the High Power Laser is stabilized to the resonance frequency of the Production Cavity using the Pound-Drever-Hall locking technique. A detailed description of the frequency stabilization is giving in Chapter 5. The transmitted beam of the Production Cavity is then spatially overlapped with the eigenmode of the Regeneration Cavity. Subsequently, a mode scan of the Regeneration Cavity is performed to determine the spatial overlap between the eigenmodes of both cavities by measuring the higher-order mode contents in its transmission. This mode scan carries the information of the planar mirror parallelism, which is proportional to the ratio between the transmitted power in the first-order mode and the fundamental mode in the eigenmode basis of the Regeneration Cavity. As described in Chapter 2, Equation 2.5 can be used to describe the percentage power in the higher-order modes using the $|\varepsilon|^2$-parameter. Assuming an ideal lateral alignment and identical radii of curvature for the curved mirror of both cavities, Equation 2.5 can be simplified as

$$|\varepsilon|^2 \approx |\varepsilon_1|^2 + |\varepsilon_2|^2 \approx \frac{|U_1|^2}{|U_0|^2} + \frac{|U_2|^2}{|U_0|^2} \approx \left(\frac{\delta\alpha_{eig}}{\theta_{0,eig}}\right)^2 + \left(\frac{\delta z_{0,eig}}{2 \cdot Z_R}\right)^2. \tag{4.4}$$

Due to the planar-concave linear cavity configuration of the 1m-prototype cavities, the waist of the eigenmode for both cavities is located on the planar mirrors. As described in Chapter 3, these mirrors are installed on the Central Optical Bench, i.e. the waists are spaced $\delta z_{0,eig}$ $\approx$ 500 mm apart due to the geometry of the optical bench. If this parameter is used together with the Rayleigh range of Z_R = 3 m to calculate the second term in Equation 4.4 and if the ALPS II angular requirement of $\delta\alpha_{eig}$ = 5 μrad is used together with the divergence angle $\theta_{0,eig}$ = 339 μrad, the following percentage power distribution in eigenmode basis of the prototype Regeneration Cavity results:

$$|\varepsilon|^2 \approx |\varepsilon_1|^2 + |\varepsilon_2|^2 \leq 0.022\,\% + 0.7\,\% = 0.722\,\%. \tag{4.5}$$

Thus, for an optimal lateral alignment, about 99.28 % of the power is expected to be in the fundamental mode. The lateral alignment of the eigenmodes is done by the means of the PZT,

which is attached to the curved mirror. Since the cavities are formed in a plano-concave configuration, angular tilts of curved mirrors are translated into lateral translation of the cavity eigenmodes on the planar mirror. The translation of the eigenmodes on the planar mirrors can be determined using the Equation 4.6

$$\Delta_{eig} = sin(\alpha) \cdot \mathrm{ROC}, \tag{4.6}$$

where α is the tilt angle of the curved mirror and ROC is its radius of curvature [56].

4.2.1 Preparations

Before the overlap experiment can be performed, some preparations are made. In a first step, the Central Optical Bench has to be assembled in the described manner. This includes also the measurement and compensation of the wedge angle for the substrates located on the optical axis. Furthermore, the PZT attached to the curved cavity mirrors has to be calibrated, since it is used as an actuator for the lateral alignment and for length scanning of the Regeneration Cavity. Finally, a photodetector has to be designed and calibrated to measure the higher-order mode contents in the eigenmode basis of the Regeneration Cavity. These preparations are described in the following sections.

4.2.2 Preparation of the Central Optical Bench

The Central Optical Bench is prepared in a first step. An important step in the preparation is the measurement of the wedge angle of the planar cavity mirrors as well as the optics located on the optical axis between the two planar mirrors (M4 and M8). The planar mirrors used are commercial substrates which are not optimized with respect to the wedge angle. Their wedge angle could be therefore larger than the 5 μrad allowed for the ALPS II substrates. Consequently, the mentioned expected spatial overlap would be limited without appropriate compensation. The measuring method explained in the Section 4.1 is used to determine the wedge angles, which are listed in the Table 4.1.

Table 4.1: Determined wedge angle for optics on the main optical axis of the Central Optical Bench. For each data five measurements are averaged. The uncertainty is given by the corresponding standard deviation.

Substrate	Pitch (μrad)	Yaw (μrad)
M_{PCO}	22 ± 1	3 ± 2
M_{RCI}	2 ± 1	46 ± 2
M4	1 ± 1	1 ± 1
M8	1.5 ± 1	1 ± 1

As can be seen from the measurement, the wedge angle for the planar mirrors is significantly larger than the tolerable 5 μrad. The mirrors M4 and M8, which are located between the planar cavity mirrors, however, meet the requirements.

The two planar mirrors are installed to be parallel in the manner described in Section 4.1 using the autocollimator. For the Production Cavity, the cuboid mirror described in Section 4.1.3 is used as a planar mirror. It is attached to the Central Optical Bench with the Π-shaped mount. The Regeneration Cavity mirror is installed in the commercial mount, which is clamped to the Central Optical Bench. The autocollimator is used to align the high-reflective surface of both mirrors such that they are parallel within 5 μrad. To compensate for the wedge angles, the parallelism is detuned by the measured wedge angles, which means that the high-reflective surface of both mirrors are refractively parallel within 5 μrad.

4.2.3 Calibration of the length and alignment actuator

The pitch and yaw platform used for the curved mirrors provides a minimum angular resolution of $\approx 44\,\mu$rad for pitch and $\approx 78\,\mu$rad for yaw. It is therefore only used as an additional alignment tool for coarse adjustment of the eigenmode position. This is to avoid saturation of the fine adjustment range provided by the 3-axis PZT. As mentioned in Chapter 3, the three PZTs in the mirror mount form a triangular constellation. To use these PTZs as an alignment platform for pitch and yaw and as an actuator for the length scanning of the cavity (z), it must be carefully calibrated with the matrix amplifier. For pitch or yaw alignment, two elements of the PZT must be controlled simultaneously. For the longitudinal degree of freedom, all three elements must be controlled simultaneously. Therefore, crosstalks between the individual degrees of freedom cannot be excluded if the amplifier is not optimally tuned. It is of particular importance to keep the crosstalk on to pitch and yaw during the longitudinal scanning (z) as low as possible. This is important to keep the power coupled to the first-order mode due to lateral misalignment of the eigenmode position as minimal as possible. Therefore, the autocollimator is used in conjunction with the matrix amplifier to calibrate the PZTs accordingly. The autocollimator is used to observe the reflection of the back side of the curved mirror. Then, a voltage signal is applied to the input of the matrix amplifier and it is then tuned by means of potentiometers in such a way that by applying a voltage to one of the degrees of freedom, crosstalk to the others is minimized. The corresponding measurements are shown in Figures 4.9 and 4.10 for pitch and yaw, respectively, and in Figure 4.11 for the longitudinal degree of freedom. Each data point represents an average of 10 measurements. The error bar is the corresponding standard deviation. A linear fit is applied to the data to determine the responses of each degree of freedom and the corresponding crosstalk to the others.

According to the measurements, the pitch and yaw provide $\approx 60\,\mu\text{rad/V} = 0.6\,\mu\text{rad/10mV}$,

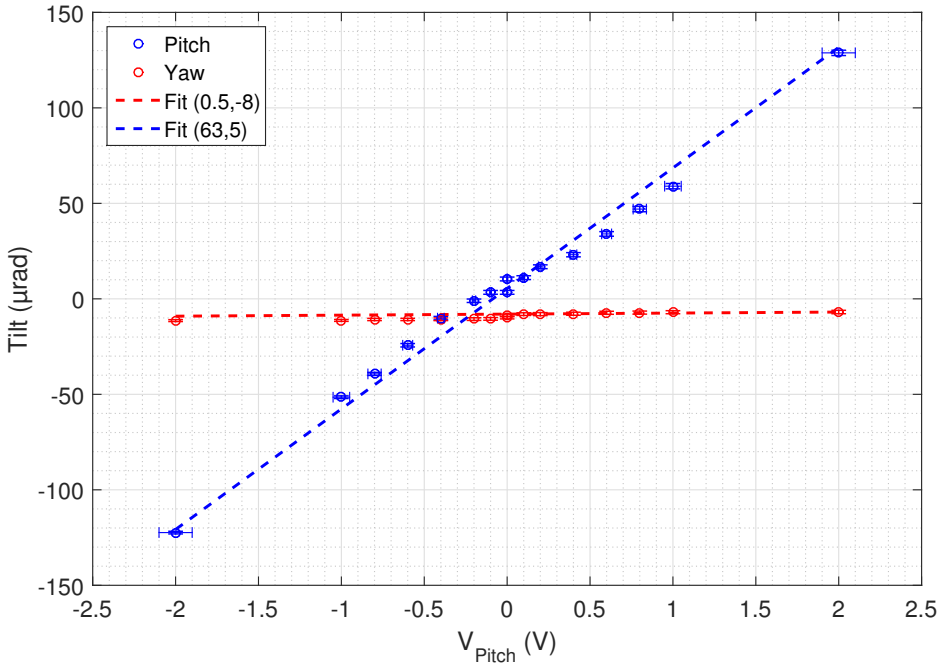

Figure 4.9: Calibration of the length and alignment actuator for the pitch degree of freedom. The autocollimator is used to measure the tilt of the curved mirror in pitch and yaw when a voltage is applied to the pitch input of the matrix amplifier, which has an amplification of 7.7 V/V. Fit legends: (a,b) with $y = ax + b$.

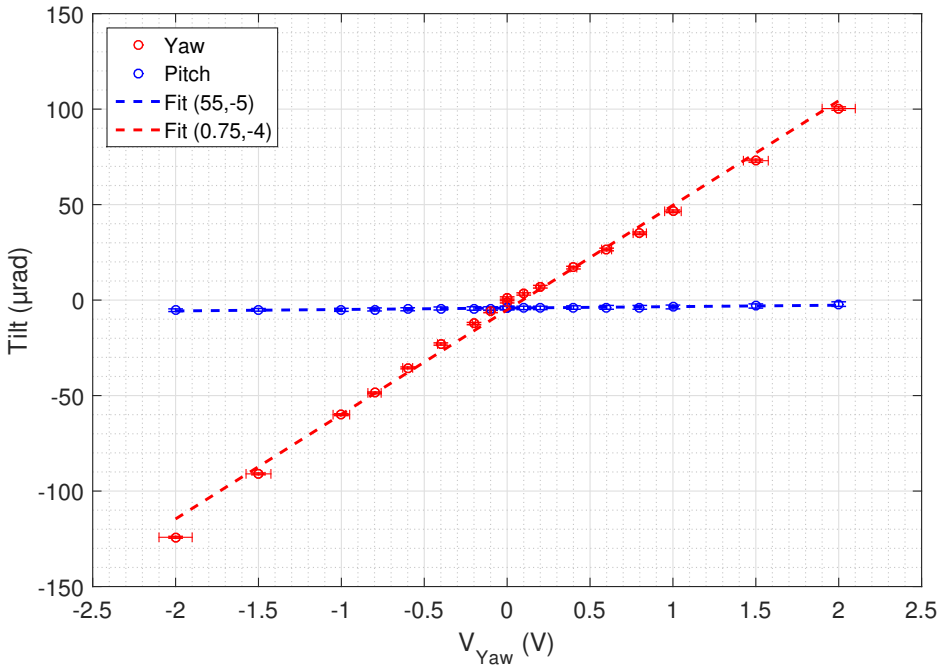

Figure 4.10: Calibration of the yaw degree of freedom in analogy to the pitch degree of freedom shown in figure 4.9. Fit legends: (a,b) with $y = ax + b$.

which allows an alignment resolution of $\approx 10\,\mu$m in vertical and horizontal planes. Furthermore, it can be seen that the matrix amplifier can be tuned in such a way that the crosstalk

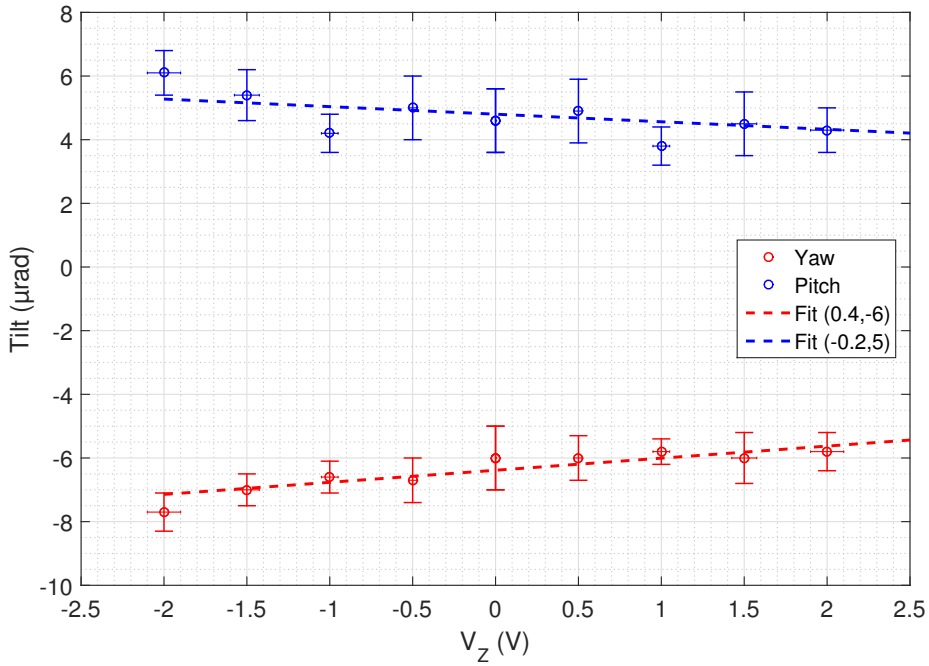

Figure 4.11: Calibration of the longitudinal degree of freedom. A voltage is applied to the z input of the amplifier and the corresponding tilt in pitch and yaw is measured using the autocollimator. Fit legends: (a,b) with $y = ax + b$.

between the degrees of freedom is $\approx 1\,\%$ and thus not relevant. The calibration of the longitudinal degree of freedom (z), is optimized such that the crosstalk is $0.2\,\mu\mathrm{rad/V}$ and $0.4\,\mu\mathrm{rad/V}$ to pitch and yaw, respectively. Using the PZTs longitudinal response ($20\,\mathrm{MHz/V}$) projected into the cavity resonance frequency and the amplifier gain of $7.7\,\mathrm{V/V}$, the applied voltage of $1\,\mathrm{V}$ corresponds to a scan of one free spectral range ($150\,\mathrm{MHz}$). Consequently, for a scan of one free spectral range, the total lateral translation of the cavity eigenmode due to pitch and yaw crosstalk is $\approx 6\,\mu\mathrm{m}$. The corresponding first-order eigenmode content $|\varepsilon_1(\Delta_{eig})|^2$ is therefore $\approx 3.6 \times 10^{-5}$ and must be taken into account for the overlap measurement.

4.2.4 Calibration of the detector

In order to measure the overlap accurately, an appropriated photodetector is essential. Due to low power expected in the first-order mode, a photodiode with a pre-amplification stage is used. The voltage signal is further amplified by $100\,\mathrm{V/V}$ amplifier stages in series, resulting in three different output amplifications: +0dB, +40dB and +80dB. These channels are combined to form the eigenmode scanning measurement as described in 4.2.6. To calibrate the channels accurately, the output voltages are determined for different optical powers. The measurement is shown in Figure 4.12.

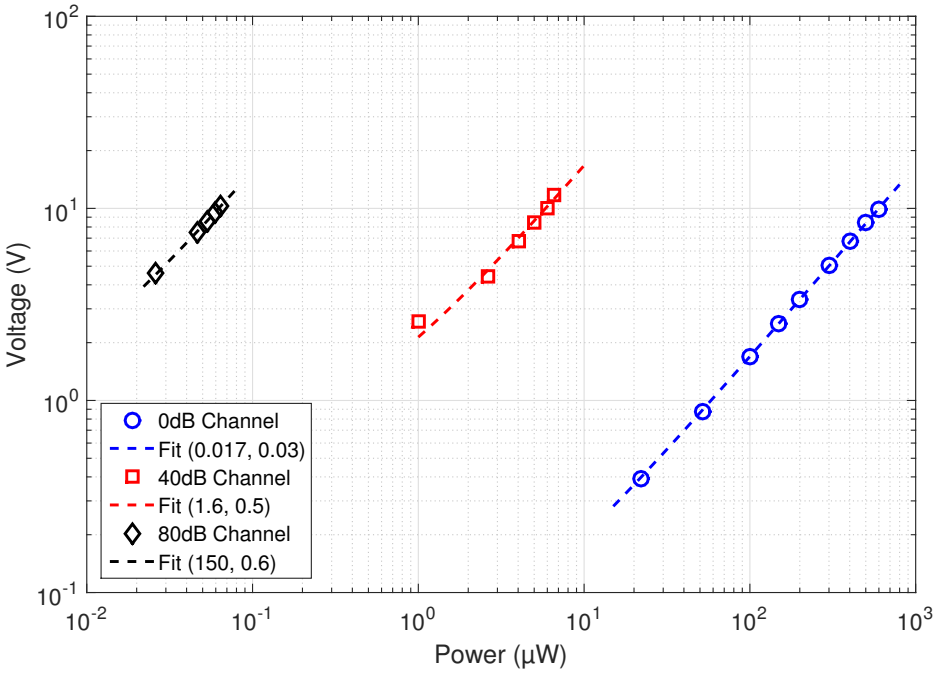

Figure 4.12: Output voltage of the different channels of the photodetector vs. optical power. For the calibration, a linear fit is applied to the data resulting in an gain of 95 V/V for the two amplification stages. Fit legends: (a,b) with $y = ax + b$.

4.2.5 Alignment of the cavities

To facilitate the alignment for the spatial overlap of the cavities, the experimental setup is prepared in several steps. These steps are explained in more detail below.

Step 1: Definition of an optical axis

In a first step, the beam of the High Power Laser is mode matched to the eigenmode of the Production Cavity. An optical axis is defined for this mode-matched beam by aligning it to the reference apertures A1 and A2, as shown in Figure 4.13. The previously prepared Central Optical Bench with the planar mirrors is then inserted and aligned to the optical axis using the aperture A1. Several aluminum layers of 200 μm thickness are used to match the height of the reflected beam to the aperture. The aperture A3 is aligned to the reflection of the planar Production Cavity mirror M_{PCO}. Then, the position of the Central Optical Bench on the optical table is registered with the aid of rods fixed to the table.

Step 2: Alignment of the curved mirror

In a second step, the Central Optical Bench is removed and the curved mirrors of both cavities are installed as shown in 4.14. The mirrors are ≈ 2.5 m apart and form two separate cavities (Production and Regeneration Cavity) once the Central Optical Bench is installed in between. These mirrors are aligned with their pitch-yaw platforms to the defined axis. Since these mirrors form a cavity, proper alignment leads to flashes in transmission of the curved Regeneration Cavity mirror while the frequency of the High Power Laser is scanned. These beam flashes can

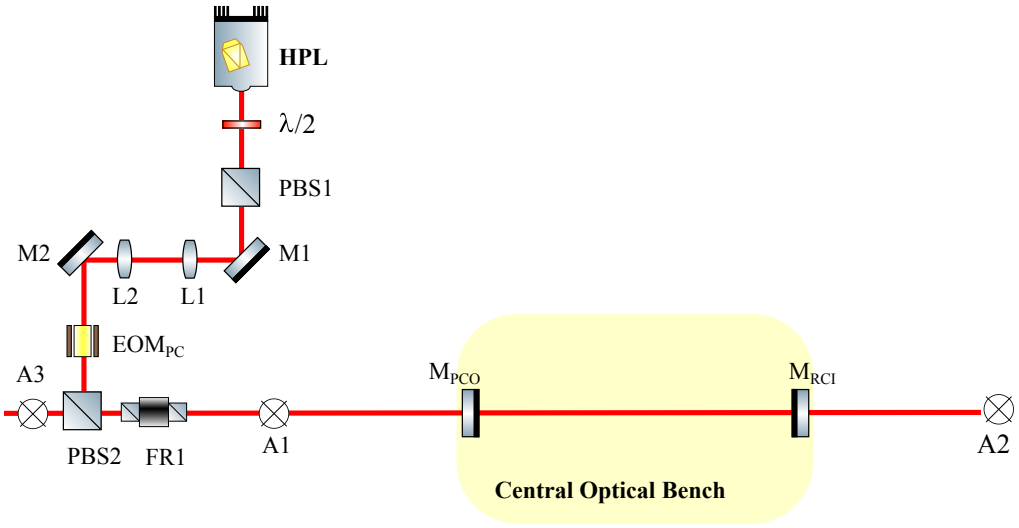

Figure 4.13: First step of the alignment procedure for the overlap performance: an optical axis is defined for the whole experiment using apertures A1, A2 and A3. The High Power Laser beam and the Central Optical Bench are aligned to these apertures. M represent mirrors, PBS polarization beamsplitter, FR Faraday rotator, L lenses and EOM electro-optic modulators.

be observed with the calibrated photodetector PD_{mon1} and CCD2.

Figure 4.14: Second step of the alignment procedure for the overlap performance: the curved mirrors are aligned to the optical axis by adjusting their reflections to the apertures A1, A2, and A3. For simplicity, the HPL and its corresponding components are not shown.

Step 3: Installation of Central Optical Bench

In a final step, the Central Optical Bench is inserted and aligned to the curved mirrors in the known manner using the rods, as described in step 1, such that the beam transmits through the apertures. The frequency of the High Power Laser is then stabilized to the resonance frequency of the Production Cavity. Its transmitted beam consequently enters the Regeneration Cavity. When correctly aligned and while scanning the length of the Regeneration Cavity by means of its calibrated length actuator, flashes are immediately seen in its transmission, which means that the eigenmodes of both cavities are spatially overlapped. To monitor the location of the cavity eigenmodes, the two 45° mirrors, M4 and M8, are then installed on the Central Optical Bench

to direct the corresponding beams to the quadrant photodiode, as shown in Figure 4.15.

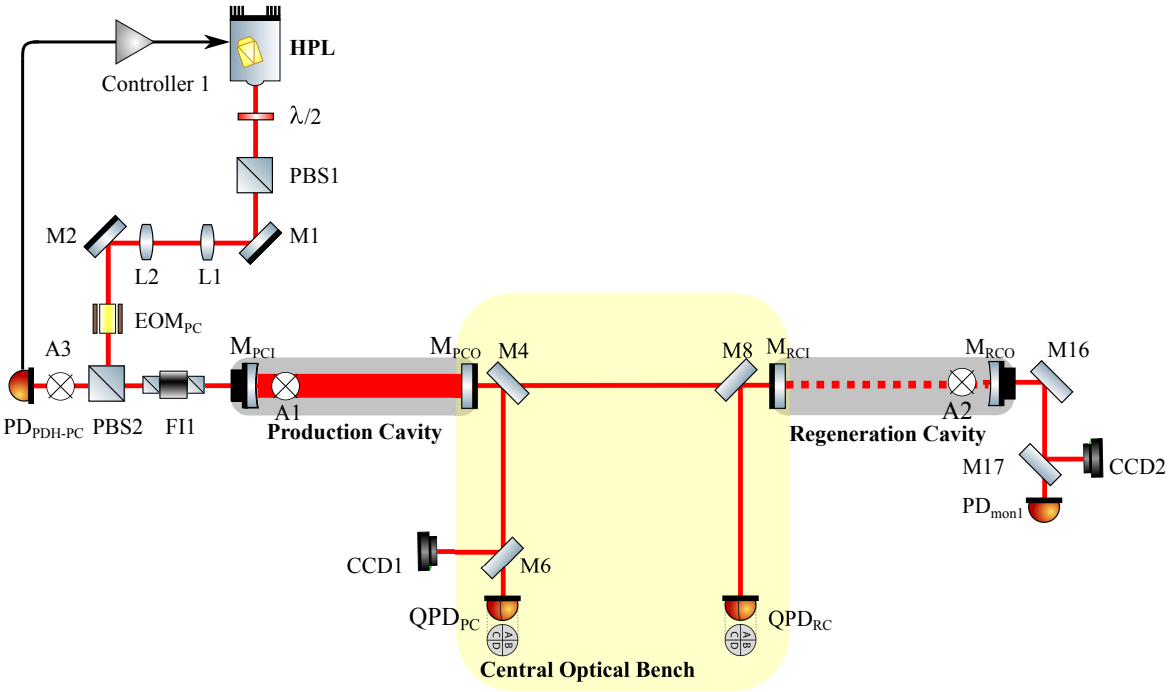

Figure 4.15: Finale step of the alignment procedure for the overlap performance: the Central Optical Bench is inserted and aligned to the defined axis using the apertures. Since both cavities are aligned to the same reference, they start to flash immediately. At this stage the eigenmodes of both cavities are coarsely spatially overlapped. Red lines depict fundamental infrared light, dashed red lines denote infrared light from Production Cavity entering the regeneration cavity and black lines denote electric wiring for Pound-Drever-Hall locking.

To optimize the overlap, the transmitted beam of the Regeneration Cavity is then sensed by the calibrated three-channel photodiode. To minimize the power in the first-order mode due to lateral misalignment, a voltage is applied to the pitch and the yaw of the PZT to fine-tune the angle of the curved mirror and with it the lateral position of the eigenmode of the cavity. The residual power remaining in the first-order mode is then attributed to angular misalignment of the eigenmodes corresponding to the angle between the planar cavity mirrors.

4.2.6 Results of the spatial overlap experiment

The result of the Regeneration Cavity mode scan, after optimizing the lateral degree of freedom, is shown in 4.16. For this measurement, the cavity is scanned over one free spectral range using the calibrated length actuator. In transmission of the cavity, the fundamental mode is detected using the 0dB-channel while the first-order mode and the second-order mode are observed with the 80dB and the 40dB channels, respectively. A lens is used to focus the transmitted beam onto the photodiode to minimize clipping-loses. The channels are observed with an oscillo-

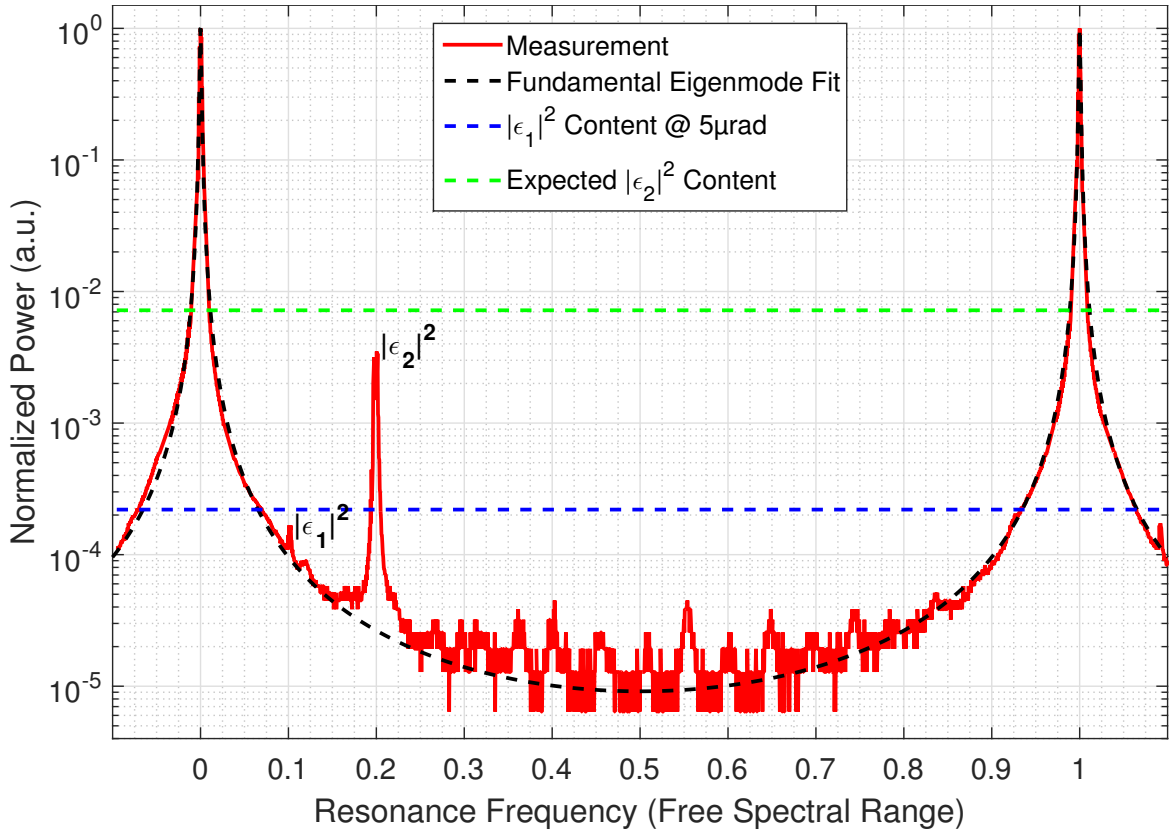

Figure 4.16: Single-trace of the cavity eigenmode scan of Regeneration Cavity for determining the parallelism of the planar mirrors. Beside the fundamental mode, the first-order mode, which is mostly related to angular misalignment, and the second-order mode, which is attributed to mismatch of waist location, are identified. Their spacing corresponds to ≈ 0.1·FSR. From the measurement, it is obvious that the angular-mismatch between the two planar mirrors is less than 5 μrad.

scope, which allows recording $\approx$ 2500 data points per channel. These data of the individual channels are then combined to form the mode scan. The x-axis (time-axis) is normalized to a the free spectral range of the Regeneration Cavity, which is 150 MHz as listed in Table 3.2. Because of the known mode spacing of 0.1·FSR, the normalization simplifies the identification of the modes. The power is normalized to the power in the fundamental mode. To estimate the percentage power distribution accurately, five measurements are averaged, resulting in the following contents:

$$|\varepsilon_1|^2 = 1.6 \times 10^{-4} \pm 1.8 \times 10^{-5}$$
$$|\varepsilon_2|^2 = 3.5 \times 10^{-3} \pm 2.6 \times 10^{-4}.$$

The specified error is the corresponding standard deviation. It is noticeable that the order-two eigenmode content is smaller by a factor 2 than the estimated value in Equation 4.5. A potential explanation might be a possible curvature of the planar mirrors, which occurs during the coating process [57, 58]. Also clipping losses might be a further reason. However,

since this content is not relevant for the estimation of the parallelism, it is not further investigated. The measured order-one content of $\approx 1.6 \times 10^{-4}$ corresponds to a parallelism of $4\,\mu$rad. Taking into account the previously mentioned contribution regarding the lateral misalignment due to crosstalks between the degrees of freedom of the actuator, it can be concluded that the angular mismatch between the cavity eigenmodes is $< 4\,\mu$rad, which confirms the previous autocollimator-measurements. This spatial overlap measurement is also performed for intentionally induced angular misalignment to further confirm the autocollimator reading. The parallelism is de-tuned for pitch and yaw and the corresponding first-order mode content is measured in the manner described above. The results are shown in Figure 4.17 together with the expected relation between angular misalignment $\delta\alpha_{eig}$ and the eigenmode content $|\varepsilon_1|^2$ (Model 1).

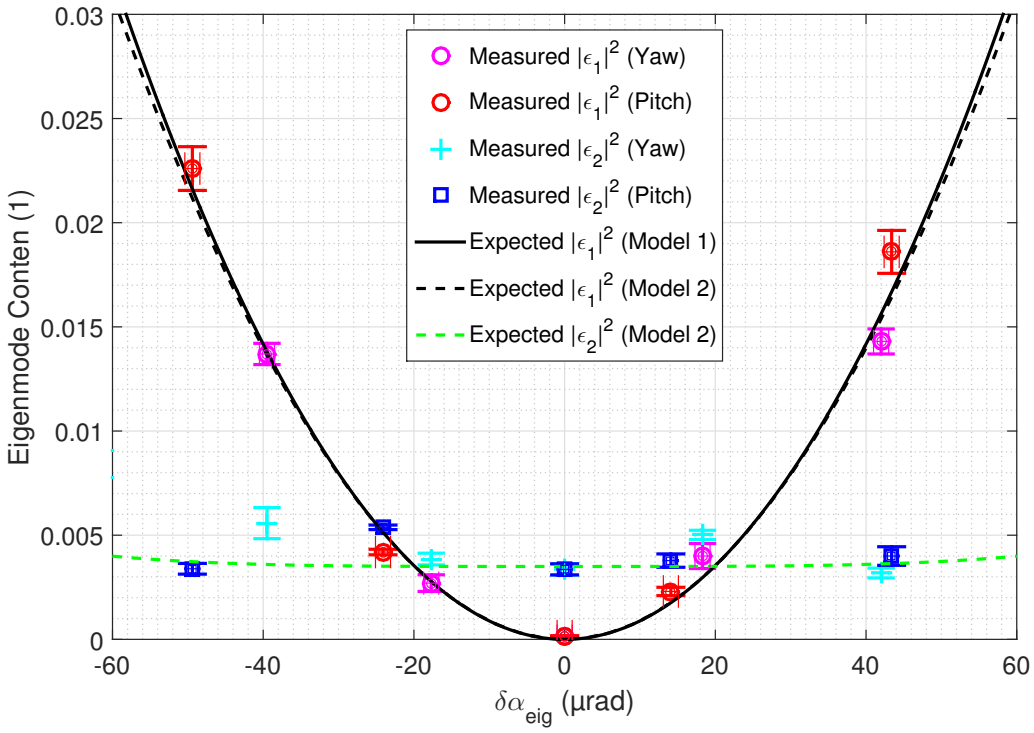

Figure 4.17: First-order mode content vs. intentionally induced angular misalignment for pitch and yaw. Since model 1 is valid only for small angular deviations, model 2, which takes into account the angular and the axial degree of freedom, is applied to the data. For comparison, the percentage power in second-order mode content $|\varepsilon_2|^2$ is also shown.

Each data point represent an average of three measurements with the corresponding standard deviation. Since the $|\varepsilon|^2$- parameter (Mode 1) is only based on a pertubative basis [34], it is valid only for $\alpha_{eig} \ll \theta_{0,eig}$. In the case of large angular deviations, the power couples also to the Hermit-Gaussian modes of order > 1. For this reason, the percentage power in second-order mode content $|\varepsilon_2|^2$ is measured and shown for comparison. A two-dimensional finite-difference

calculation (Model 2) of

$$\varepsilon_k = \sum_{n,m\in\mathbb{N}}^{n+m=k} \left\{ \iint U_{00}(\alpha_x, \alpha_y, 0) \cdot U^*_{nm}(\alpha_x + \delta\alpha_{\text{eig}}, y, \delta z_{0,\text{eig}}) d\alpha_x d\alpha_y \right\}, \tag{4.7}$$

is additionally applied to the measurement [29], where U_{nm} represents the field of a Hermite-Gaussian beam of order (n,m). This model considers the contribution of the relative angular degree of freedom and the relative axial position to the $|\varepsilon|^2$- parameter. As can be seen from the Figure 4.17, the two models agree very well for $\theta_{0,eig} \leq 40\,\mu$rad or $|\varepsilon_1|^2 \leq 1.4\,\%$ and are consistent with the measurement. For larger $\delta\alpha_{eig}$, the model 2, which is based on the finite-difference calculation, would be better suited to describe the measurement. However, since ALPS II is anticipated to work with sub-percent $|\varepsilon_1|^2$, the pertubative model based on Equation 4.4 is valid. This measurement can therefore be considered as a further verification of the autocollimator-measurement and as a verification of the pertubative model used to describe the spatial overlap with respect to the angular degree of freedom.

4.2.7 Summary and conclusion

The prototype, described in Chapter 3, is used to confirm the concept of measuring the angle-mismatch between the ALPS II planar cavity mirrors using an autocollimator. For this purpose, the frequency of the High Power Laser is stabilized to the resonance frequency of the Production Cavity and the eigenmode of the Production Cavity is spatially overlapped with the eigenmode of the free running Regeneration Cavity. To estimate the spatial overlap, the length of the Regeneration Cavity is actuated and a mode scan is performed in its eigenmode basis. A calibrated three-axis PZT is used to align the eigenmodes laterally to minimize the power contributions to the first-order modes due to lateral mismatches. A calibrated three-channel photodiode is used for the mode scan measurement. Two measurements are performed: in a first step the planar mirror are aligned with the autocollimator such that the angular mismatch is $< 5\,\mu$rad, and a spatial overlap is performed to measure the relative power in the first-order mode content. The measurement shows a relative power of $\approx 1.6 \times 10^{-4}$ for the first-order mode content $|\varepsilon_1|^2$, which corresponds to an angular mismatch of $4\,\mu$rad and therefore clearly confirms the autocollimator measurement. The relative power in the second-order mode content is also determined in this measurement, and a discrepancy between the expected and measured value is found. This might be explained by possible curvature of the planar mirrors that occurred during the coating process or by clipping losses. In a second attempt, several angular mismatches of $> 5\,\mu$rad are intentionally induced to the planar mirrors and the corresponding power contribution to the first-order mode is measured and compared with the expected relation between $|\varepsilon_1|^2$ and $\delta\alpha_{eig}$. The data shows that for the targeted sub-percent level of $|\varepsilon_1|^2$, the measurement is

almost perfectly consistent with the pertubative model of $|\varepsilon_1|^2$. Since the planar mirrors are aligned using the autocollimator, it can be concluded that the aimed ALPS II autocollimator-assisted measurement is sufficient to prove the requirement on the angular degree of freedom. The findings of this section are published in [59].

4.3 Stability of quadrant photodiode mounts

ALPS II intents to use quadrant photodiodes as references for the lateral position of the cavity eigenmodes. To preserve the anticipated overlap mentioned in Chapter 2, their lateral drift should not exceed 100 μm. Therefore, the stability of their mechanical mount is tested in a corresponding experiment. The quadrant photodiode (*QP50-6*) used is from *FirstSensor* with an active diameter of ≈ 7.98 mm and a gap of 42 μm between the elements. The DC voltage of the individual elements of the quadrant photodiode is added to an overall sum signal U_s by means of appropriate electronics. To measure the beam position on the quadrant photodiode with respect to its center, two differential signals, U_x and U_y, are generated as shown in Equation 4.8:

$$\begin{aligned} U_s &= U_A + U_B + U_C + U_D \\ U_x &= (U_A + U_D) - (U_C + U_B) \\ U_y &= (U_A + U_B) - (U_C + U_D). \end{aligned} \tag{4.8}$$

Here $U_{A,B,C,D}$ are the voltage signals of the individual elements. These signals can be used to estimate the beam position, with respect to the center of the quadrant photodiode, according to the following Equation 4.9

$$\Delta x, y = \sqrt{\left(\frac{\pi}{8}\right)} \cdot \omega_{0,eig} \cdot \frac{U_{x,y}}{U_s}, \tag{4.9}$$

where $\Delta x, y$ are the beam positions in horizontal and vertical plane, respectively [60–62]. This formalism is used to read out the beam position on the quadrant photodiodes.

4.3.1 Readout verification

To verify the reading of these quadrant photodiodes, the frequency of the High Power Laser is first stabilized to the resonance frequency of the Production Cavity. The quadrant photodiodes are then centered to its transmitted beam as illustrated in Figure 4.15. $\mathrm{QPD_{PC}}$ is centered to the beam directed by the mirror M4 and $\mathrm{QPD_{RC}}$ is aligned to the back-reflected Regeneration Cavity beam directed by the mirror M8. Theses beams are representing the eigenmode location of the Production Cavity on both quadrant photodiodes. Then, the eigenmode location of the

Production Cavity is altered by applying a voltage to the corresponding degree of freedom of its alignment PZT. The corresponding lateral movement Δ_{eig} is then read on the quadrant photodiodes using the Equation 4.9 and is compared to its decomposition in terms of eigenmode content of the Regeneration Cavity, which is scanned in length. The measurement is performed for both the vertical and horizontal plane and is shown in Figure 4.18 and 4.19 for the Regeneration Cavity and Production Cavity quadrant photodiode, respectively. Additionally, the expected relation between Δ_{eig} and the eigenmode content $|\varepsilon_1|^2$ according to Equation 2.5 is shown. For each data point, five measurements are averaged. The error bars shown are the corresponding standard deviations. Since the ε^2- model is also for the lateral degree of freedom only based on a pertubative basis [34], it is valid only for $\Delta_{eig} \ll \omega_{0,eig}$, as can be seen from the measurements. For this reason, the percentage power in second-order mode content $|\varepsilon_2|^2$ is measured and shown for comparison. In analogy to the previous section, a two-dimensional finite-difference calculation (Model 2) of

$$\varepsilon_k = \sum_{n,m\in\mathbb{N}}^{n+m=k} \left\{ \iint U_{00}(x,y,0) \cdot U^*_{nm}(x+\Delta_{\mathrm{eig}},y,\delta z_{0,\mathrm{eig}})dxdy \right\}, \tag{4.10}$$

is plotted additionally, which considers the contribution of the relative lateral and axial position to the $|\varepsilon|^2$- parameter. This is shown for $|\varepsilon_1|^2$ and $|\varepsilon_2|^2$. As can be seen from the measurements, both models agree almost perfectly for $|\varepsilon_1|^2$ for eigenmode displacements $\Delta_{eig} \leq 150\,\mu$m, e.g $|\varepsilon_1|^2 \leq 2\,\%$, and are consistent with the quadrant photodiode readings using Equation 4.9. For larger eigenmode displacements, the quadrant photodiode readings are better described by model 2. It can also be seen that $|\varepsilon_2|^2$ slightly increases for larger eigenmode displacements as predicted by model 2, which is due to power coupling into modes of order $>$ 1. This measurement clearly verifies the reading of the quadrant photodiode based on Equation 4.9, which justifies the anticipated ALPS II tracking concept of the cavity eigenmode positions. Furthermore, this measurement can be considered as a guarantee for the accuracy of the drift measurement of the quadrant photodiode mounts in the next section.

4.3.2 Drifts measurement

In a next step, the stability of the quadrant photodiode mounts is tested. For this purpose, the experimental setup shown in Figure 4.15 in the previous Section 4.2 is used. However, a modification is made by removing the Production Cavity from the setup. This is to get rid of its possible lockouts. The High Power Laser beam is directed and centered to the quadrant photodiodes using mirrors M4 and M8. Then, the differential voltages U_x, U_y and the sum voltage U_s are registered using a multi-channel analog-to-digital converter (ADC) from *Texas Instrument.* The data are sampled in 5 s intervals with 10000 samples per channel and are

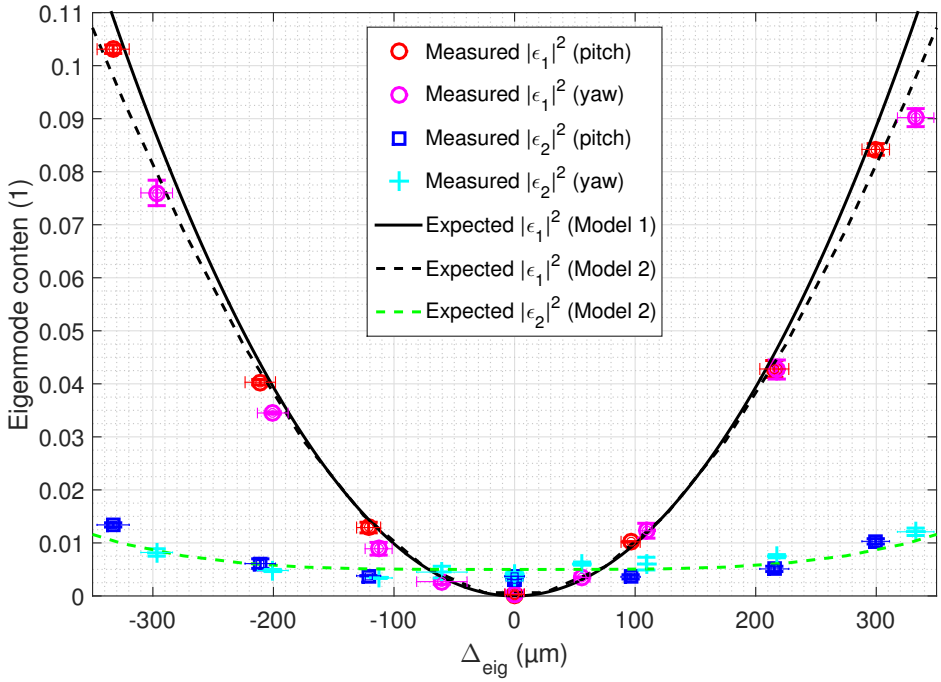

Figure 4.18: Verification of the Regeneration Cavity quadrant photodiode reading using the power coupled into the first-order mode due to lateral mismatch of the cavity eigenmodes. For an accurate verification, two different models are applied to the measured data. The percentage power in second-order mode is shown to illustrate that for large lateral mismatch power couples also into modes of order higher than 1.

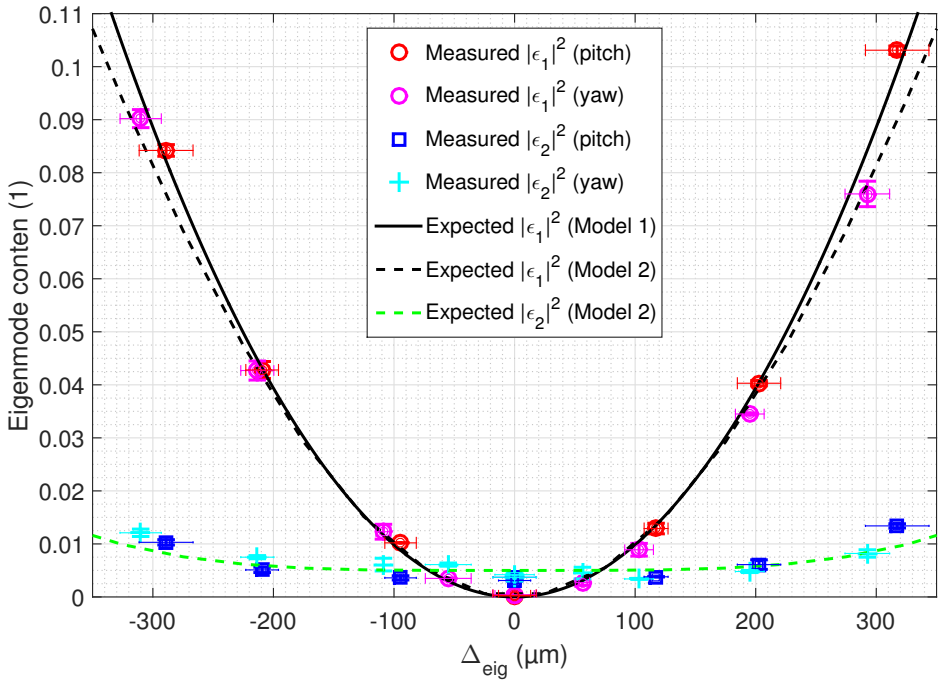

Figure 4.19: Verification of the Production Cavity quadrant photodiode reading using the power in the first-order mode due to lateral displacement in analogy to the verification of the Regeneration Cavity quadrant photodiode shown in Figure 4.18.

registered over a course of $\approx$ 120 hours. These voltages are then translated to beam positions using Equation 4.9. To cross out possible beam fluctuations, the beam position on both quadrant photodiodes are subtracted from each other. This is done for both the horizontal and vertical planes. The results of the measurement are shown in Figure 4.20.

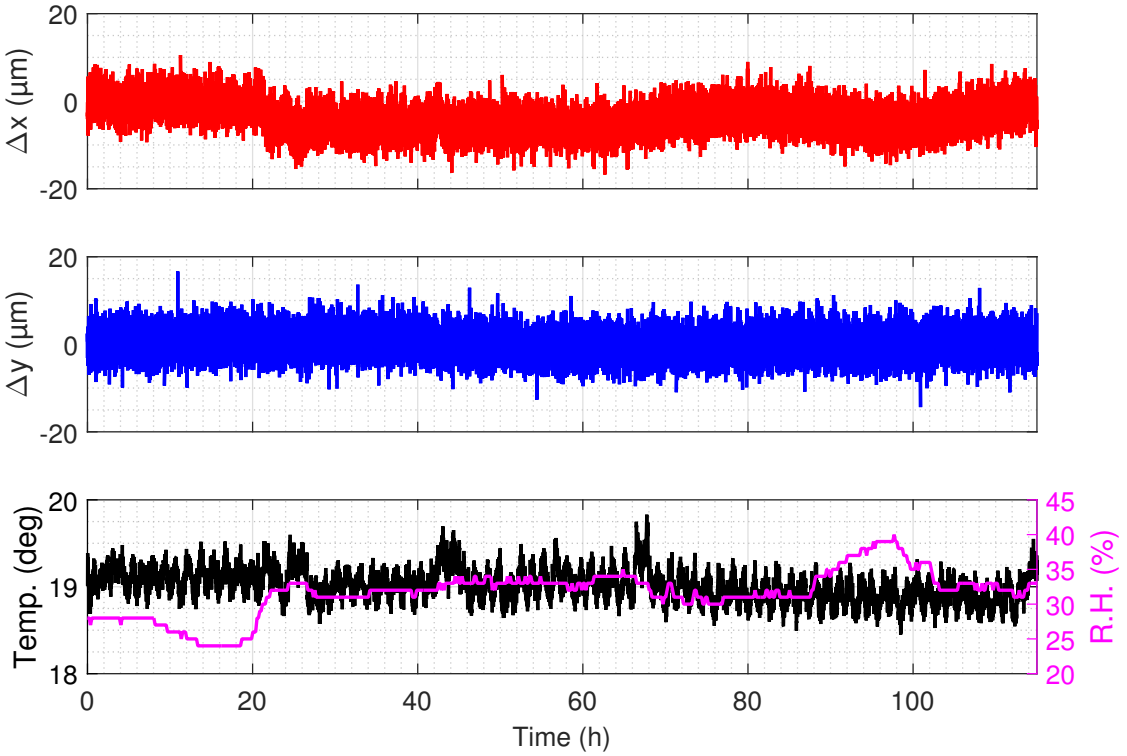

Figure 4.20: Measured time series on quadrant photodiode drifts for the vertical and horizontal plane. The measurement verify that the long-term stability of the quadrant photodiodes meets the ALPS II requirements. In the lower plot the left y-axis represent the temperature while the right y-axis shows the relative humidity (R.H.).

As can be seen from the measurement, the mounted quadrant photodiodes provide a high-stability; the peak-to-peak drift is $< 40\,\mu$m for both the vertical and horizontal plane. There exists a correlation of 0.4 between the relative humidity and the horizontal plane to be compared with the correlation of -0.3 between the vertical plane and the relative humidity. Since this correlation does not lead to significant drifts and ALPS II will be performed in vacuum, this effect is not further investigated and can be neglected. The correlation to temperature is also negligible.

Thus, it can be concluded that the quadrant photodiode mounts used fully suffices the ALPS II requirements regarding lateral drifts.

4.3.3 Summary and conclusion

The 1m-prototype is used to verify the reading of the quadrant photodiodes and the long-term stability of their mounts, which are aimed to be used for ALPS II. For this purpose, the frequency of the High Power Laser is stabilized to the resonance frequency of the Production Cavity whose eigenmode is spatially overlapped with the eigenmode of the Regeneration Cavity. Its eigenmode is translated using a calibrated three-axis PZT and the translation is measured using the quadrant photodiodes. The corresponding first-order mode content is measured for each translation and compared with the expected relation between Δ_{eig} and $|\varepsilon_1|^2$. It is shown that the eigenmode position determined by the quadrant photodiodes and the corresponding first-order mode content are for displacements $\Delta_{eig} \leq 150\,\mu$m almost perfectly consistent with the expected pertubative relation between Δ_{eig} and $|\varepsilon_1|^2$. For larger displacements, the quadrant photodiode reading could be verified by an additional two-dimensional finite-difference calculation.

The same test bed is used to quantify the mechanical stability of the quadrant photodiode mounts. A test beam is centered on the quadrant photodiode for monitoring its position. It is shown that over a measurement period of ≈ 120 hours the quadrant photodiode drift is less than $20\,\mu$m for both the horizontal and vertical plane, which meets the ALPS II requirements.

Thus, the quadrant photodiodes aimed to be used in ALPS II to track the eigenmode position of the Production and Regeneration Cavity provide precise readout of the eigenmode position and their long-term performance regarding lateral drifts meets the ALPS requirements. The findings of this section are published in [59].

Chapter 5

Dual resonance experiment

Besides the proven stability in terms of angular and lateral degree of freedom, the spectral degree of freedom is a crucial parameter for ALPS II. To keep the field of the Production Cavity resonant within the Regeneration Cavity, it is essential to stabilize the length of the Production Cavity to the length of the Regeneration Cavity. To control this degree of freedom, ALPS II utilizes an offset phase-locked loop to maintain synchronous resonance of the two cavities. As described before, ALPS II can tolerate about 5 % power loss of the Production Cavity beam within the Regeneration Cavity due to the spectral mismatch. Considering the line-width of the Regeneration Cavity of ALPS II, this means that the resonant frequencies of both cavities should have less than 0.5 Hz mismatch. Due to the in air configuration of the 1m-prototype cavities, it is very difficult to meet the frequency stabilization requirements of the ALPS II with the prototype cavities. Therefore, the aim of this chapter is to demonstrate the frequency and lengths control scheme of ALPS II as a proof-of-concept experiment. The goal is to demonstrate that the Production Cavity beam experiences no more than 5 % RMS power fluctuation downstream of the Regeneration Cavity while the entire system is stabilized.

This chapter is arranged as follows: Section 5.1 gives an overview of the control structure of the prototype, which includes the control system for frequency stabilization of both lasers and the control system of the phase-locked loop. The following Sections 5.2 and 5.3 describe the performance of the Production and Regeneration Cavity in terms of frequency and power noise. Finally, Section 5.4 describes the results related to the dichroic lock of the Regeneration Cavity. For these experiments, the second harmonic stage described in Chapter 3 is used.

5.1 Control architecture

For a better understanding of the experiments performed in this chapter, a brief description of the locking architecture of the 1m-prototype is given, which is schematically shown in Figure 5.1.

The frequency of the High Power Laser is stabilized to the resonance frequency of the Produc-

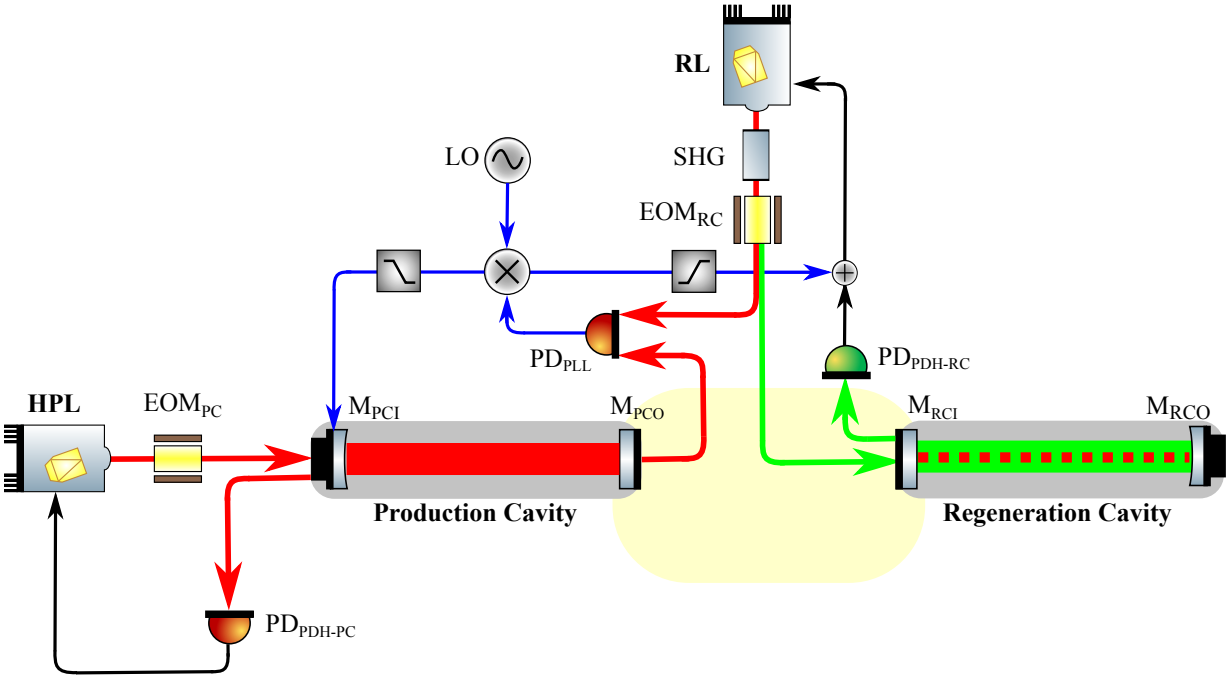

Figure 5.1: Control architecture for the 1m-prototype. The frequency of the High Power Laser is stabilized to the resonance frequency of the Production Cavity. At the same time, the frequency of the Reference Laser is stabilized to the resonance frequency of the Regeneration Cavity by means of its frequency-doubled beam. Additionally, a phase-locked loop is implemented to match the frequency of the Production Cavity field to the resonance frequency of the Regeneration Cavity. Red lines depict infrared light from the High Power Laser and Reference Laser while green lines represent the second harmonic light of the Reference Laser. Black lines depicts electric wiring for the Pound-Drever-Hall frequency locking, and blue lines denote electric wiring for the phase-locked loop.

tion Cavity by means of a dedicated frequency stabilization feedback-control loop [63], which acts on the frequency of the High Power Laser. A similar control loop is used to stabilize the frequency of the Reference Laser to the resonance frequency of the Regeneration Cavity. However, there is a significant difference: While the High Power Laser frequency is stabilized via its fundamental beam, the Reference Laser is frequency doubled and its second harmonic beam is used for frequency stabilization. A detailed description of the frequency stabilization is given in the next section. While the frequency of both lasers are individually stabilized, an additional control loop ensures that the field circulating in the Production Cavity resonates also within the Regeneration Cavity[1]. This additional loop is a so called phase-locked loop (PLL) [39–41, 64], as described in Chapter 3. For this purpose, a beat note signal of the transmitted field of the Production Cavity and the fundamental field of the Reference Laser is generated, which is sensed

[1]Unlike ALPS II, the prototype is built without a wall such that the transmitted Production Cavity beam reaches the Regeneration Cavity unhindered.

by the photodiode PD_{PLL}. This beat note signal is matched via a feedback-control loop to an anticipated offset frequency from a local oscillator. If the beat frequency drifts, e.g. if either the High Power Laser or the Reference Laser frequency changes, the control loop acts on the length of the Production Cavity by means of its PZT to keep the beat note signal matched to the reference frequency. Due to resonances of the Production Cavity length actuator, the unity gain frequency for this path of the control loop is limited to be $< 2.5\,\mathrm{kHz}$, as shown in Section 5.4. Therefore, the control signal of the PLL is low-pass filtered before sending it to the PZT of the Production Cavity. Additionally, to provide more robustness for the PLL, a high-pass filtered control signal is fed to the error point of the Pound-Drever-Hall loop of the Reference Laser. Its control system treats this signal as an additional frequency fluctuation of the Reference Laser causing the control loop to act on the frequency of the Reference Laser. This feedback is necessary to provide a stable operation of the PLL with a high unity gain frequency. Due to the large line-width of the Regeneration Cavity for the second harmonic beam of the Reference Laser, this additional frequency fluctuation does not lead to instability of the control system. However, there are power fluctuations of the green beam downstream of the Regeneration Cavity, because the added PLL control signal shifts the frequency of the Reference Laser away from the resonance frequency of the Regeneration Cavity. These power fluctuations are tolerated in the 1m-prototype experiment as well as in ALPS II. It should be noted that the departure of the green light from the Regeneration Cavity resonance neither influences the length of the Regeneration Cavity nor the frequency of the High Power Laser. Therefore, it does not influence the resonance condition of the High Power Laser beam in the Regeneration Cavity.

5.1.1 Frequency stabilization of the High Power and the Reference Laser

To increase the number of photons within the Production Cavity before the wall, the frequency of the High Power Laser is stabilized to a resonance of the Production Cavity. On the other side of the wall, the frequency of Reference Laser is stabilized to the resonance frequency of the Regeneration Cavity to transfer the Regeneration Cavity resonance frequency to the PLL's sensing beat note. These frequency stabilization are usually achieved with a dedicated feed-back control loop, which controls the frequency of the High Power and Reference Laser by means of their PZTs. The control loop actively minimizes the differential frequency between the frequency of the lasers and the resonance frequency of the cavities. There are several techniques for generating an error signal for the frequency stabilization between a laser and a cavity [65, 66], among them the well established Pound-Drever-Hall technique [38]. This method can be used to either stabilize the frequency of a laser to a resonance frequency of the cavity or vice versa. A detailed introduction to this technique can be found in [36]. The method relies on radio frequency (RF)

phase-modulation sidebands, which are imprinted to the carrier frequency of the light incident into the cavity. This sidebands are usually generated by passing the incident carrier through an electro-optic modulator, which uses the Pockels effect [67]. In the experiment, the control system for this concept can be represented by a block diagram shown in Figure 5.2, which is explained using the High Power Laser as an example, but is also applicable to the Reference Laser.

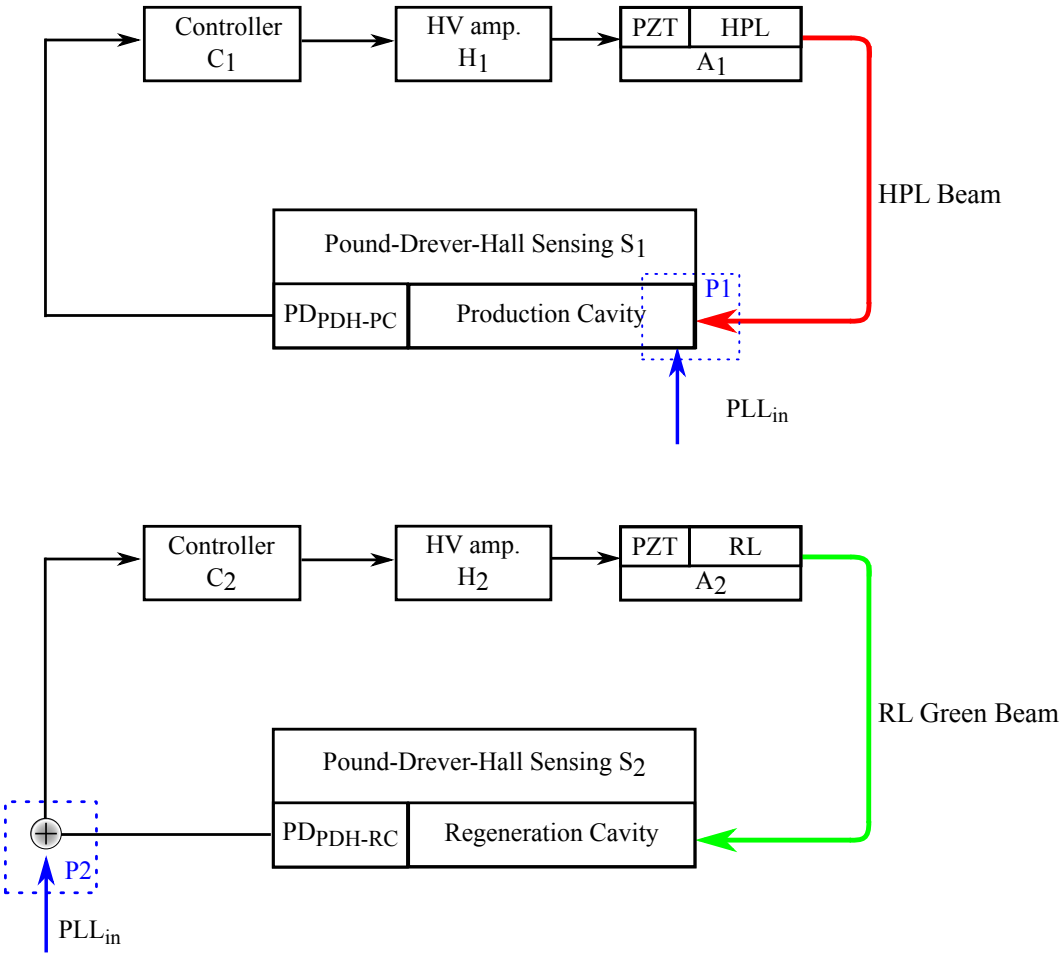

Figure 5.2: Block diagram of the control loop for the frequency stabilization of the High Power Laser (above) and the Reference Laser (below). The frequency difference between the lasers and the cavities resonance frequency is measured using the Pound-Drever-Hall sensing. In case of frequency drifts of the lasers from the resonance frequency of the cavities, a controller C, applies a voltage to the PZT A of the High Power Laser / Reference Laser to tune the corresponding frequency. A high-voltage amplifier H is used to extend the dynamic range of the PZTs. The red line denotes infrared light from the High Power Laser, the green line represent the second harmonic beam of the Reference Laser and the black lines are electric wiring. The dashed blue diagram P1 and P2 are the interfaces of the individual loops, which are relevant for the phase-locked loop in the next section.

The frequency difference is measured by the Pound-Drever-Hall sensing mentioned above.

This unit of the control system can be described by a complex transfer function of S_1. The Pound-Drever-Hall signal that serves as the error signal is fed to a controller, which has a complex transfer function of C_1. In case of a change of the differential frequency, the controller sends a voltage signal to the PZT of the High Power Laser and actuates its frequency. The PZT can be allocated with a transfer function of A_1. In order to keep the dynamic range for the frequency actuation as large as possible, the voltage signal is amplified by means of a high-voltage amplifier with the transfer function H_1. The transfer function of the components can be combined to an overall open-loop transfer function [63] of

$$L_{PC} = C_1 \cdot H_1 \cdot A_1 \cdot S_1. \tag{5.1}$$

As described in the next section, the phase-locked loop interacts with the closed-loop transfer function of frequency loop of the lasers, which is defined as

$$L_{PC-CL} = \frac{L_{PC}}{1 + L_{PC}}. \tag{5.2}$$

In analogy, the following transfer functions result for the frequency stabilization control system of the Reference Laser:

$$L_{RC} = C_2 \cdot H_2 \cdot A_2 \cdot S_2 \tag{5.3}$$

$$L_{RC-CL} = \frac{L_{RC}}{1 + L_{RC}} \tag{5.4}$$

Based on this concept, a dedicated control system is designed for the High Power Laser and the Reference Laser. The performance regarding frequency noise and relative power noise downstream of the corresponding cavity are investigated in the Sections 5.2 and 5.3.

5.1.2 Phase-locked loop for the Production Cavity

The next step towards a complete stabilization of the entire prototype system is the implementation of the phase-locked loop. This ensures accurate tracking of the Production Cavity field to the Reference Laser, while the frequency of the lasers is stabilized to the resonance frequencies of the cavities. A detailed introduction to PLL is given in [42, 64]. The principle is essentially based on measuring a signal to be controlled and comparing it with a reference signal. If a deviation is detected, the system generating the signal is actuated to match it to the reference signal. In case of ALPS II and the prototype, the signal to be controlled is the beat note signal between the field of the High Power Laser circulating in the Production Cavity and the fundamental field of the Reference Laser when its frequency is stabilized to the Regeneration Cavity via its sec-

ond harmonic beam. Here, this signal contains the information about the phase and frequency difference between the two lasers, when the Production Cavity field is additionally resonating in the Regeneration Cavity. As mentioned before, the ratio between the harmonic frequency of the Reference Laser and the High Power Laser within the Regeneration Cavity is not an integer factor two, which is due to the properties of the dichroic coatings of the cavity mirrors. The reference signal, with which the beat note signal is compared and which is provided by a local oscillator, has exactly this offset frequency of both fields. These two signals are compared by a phase and frequency detector. The detector used here is a digital circuit based detector called *MCH12140* from *On Semiconductor* [68]. It is compatible with analog phase-locked loops and is similar to the detectors used for squeezed light sources [45]. The detector output signal is proportional to the phase difference between the reference signal and the beat note signal. The aim of the PLL is to keep this signal as small as possible, i.e. to keep the beat note signal and the reference signal matched. If the beat note signal fluctuates, i.e. if either the frequency of one of the lasers or the frequency of both independently change, either the frequency of the Reference Laser or the High Power Laser is actuated, depending on the speed of the fluctuation. At low frequencies, the length of the Production Cavity is driven, which is proportional to the frequency of the High Power Laser, and at higher frequencies the frequency of the Reference Laser is driven directly by feeding a signal to the error point of its frequency control loop. In a real scenario, the entire phase-locked loop for the prototype can be represented by the block diagram depicted in Figure 5.3.

The beat note signal of the Reference Laser and the High Power Laser is sensed by the detector PD_{PLL} and the corresponding phase is compared with the phase of the reference signal by the phase detector. The photodiode and the phase detector are allocated with the complex transfer function S3. For every change in phase, the controllers C3 and C5 send a low-pass filtered signal to the PZT of the Production Cavity actuator with the transfer function A3 and a high-pass filtered signal to the error signal of the Reference Laser's frequency control loop and thus causing the loop to act on the frequency of the Reference Laser via its PZT. The controller have the transfer functions C_3 and C_5 for the Production Cavity and Reference Laser, respectively. Their signals are fed to the interaction interfaces, which are marked with dotted blue lines and labeled with P1 and P2 in the block diagram shown in Figure 5.2. Therefore, the PLL control system interacts with the closed-loop transfer function of the High Power and the Reference Laser frequency stabilization loop. Taking this aspect into account, the following transfer function results for the Production Cavity path:

$$L3 = C_3 \cdot H_3 \cdot A_3 \cdot L_{PC-CL}. \tag{5.5}$$

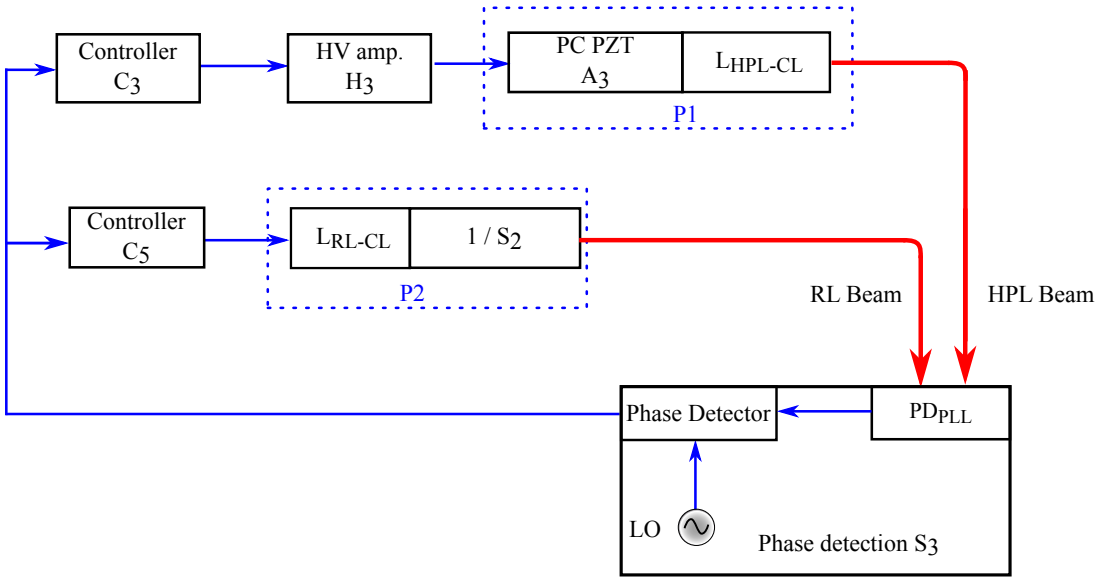

Figure 5.3: Block diagram of the phase-locked loop for the 1m-prototype. The beat note signal is sensed by the photodiode PD_{PLL} and is compared to the reference frequency by the phase detector. To continuously match theses signals, the frequency of the High Power Laser is actuated by the controller C3 at low frequencies. At higher frequencies, the frequency of the Reference Laser is actuated by the controller C5. The red lines denote the infrared beam of the High Power Laser downstream of the Production Cavity and the infrared beam of the Reference Laser. The dotted blue lines, labeled with P1 and P2, are the interaction interfaces with the frequency stabilization loops of both lasers, which are labeled in the same way in the Figure 5.2. The PLL loop interacts with the closed-loop transfer function of the frequency stabilization loop of both lasers.

In analogy to that, a similar transfer function results for the Reference Laser path:

$$L3 = C_5 \cdot L_{RL-CL} \cdot \frac{1}{S_2}. \tag{5.6}$$

These transfer functions can be combined to the following overall loop for the entire PLL system

$$L_{PLL} = (L3 + L4) \cdot S_3. \tag{5.7}$$

In comparison to the frequency stabilization explained in the previous section, there is an essential difference with this control system: for frequency stabilization, the sensor converts a frequency into a voltage while the actuator converts a voltage into a frequency. In the PLL control system, the sensor converts a phase difference to a voltage and the actuators convert the control voltage into a length change or frequency change, respectively. It is important to consider this fact when designing the PLL control loop. Based on this knowledge, a dedicated control system is designed for the prototype in Section 5.2.1 and the associated performance is experimentally investigated .

5.2 Performance of the Production Cavity

This section describes the performance of the frequency stabilization of the High Power Laser. First the design of the control loop is discussed. Its transfer function is then measured experimentally and discussed. Afterwards, the Production Cavity is analyzed regarding its free running length noise. Finally, the relative power noise of the High Power Laser is analyzed downstream of the Production Cavity.

5.2.1 Design of the control loop

In order to perform the frequency stabilization of the High Power Laser, its beam is mode matched to the eigenmode of the Production Cavity as described in the previous Chapter 4. Before incident on the Production Cavity, the beam passes an EMO_{PC} that imprints sidebands at 3.5 MHz, which are needed to generate an error signal for the frequency stabilization loop. In the next step, a controller is then designed based on the transfer function of the frequency actuator of the High Power Laser, which is shown in Figure 5.4.

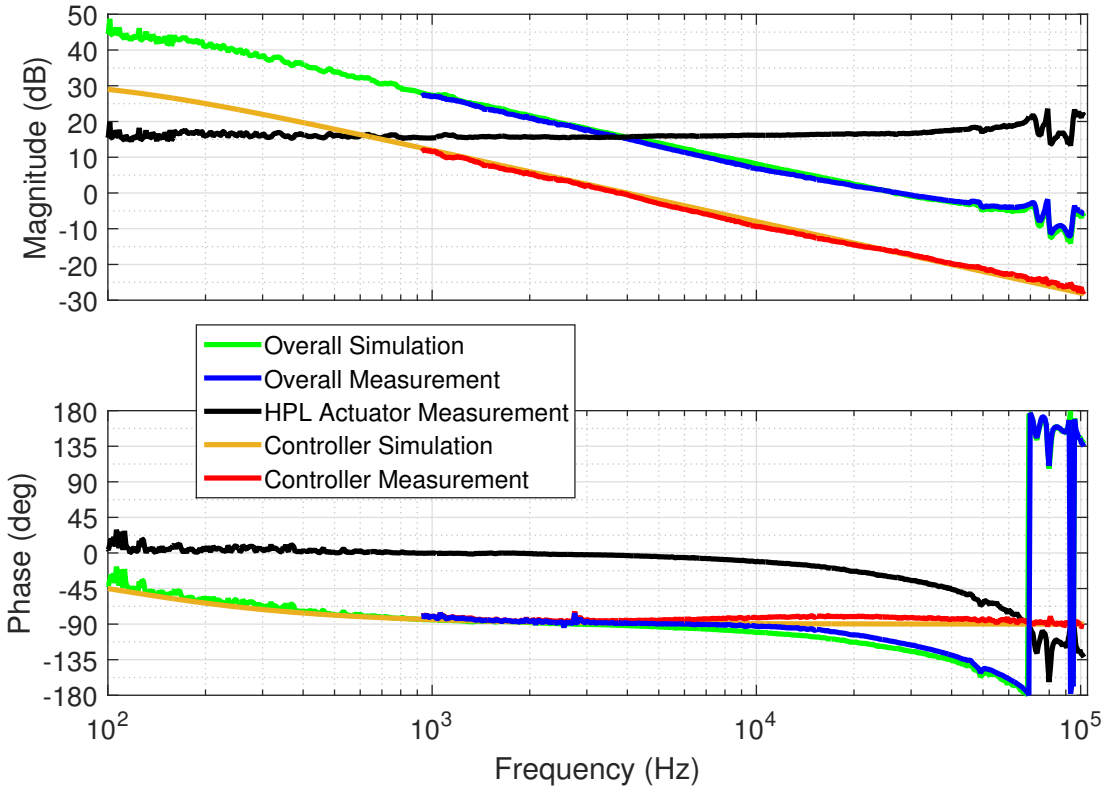

Figure 5.4: Bode plot of the measured and simulated transfer functions of the components for the control loop of the frequency stabilization of the High Power Laser and the resulting open-loop transfer function, which has a unity gain frequency of ≈ 27 kHz. The overall transfer function is measured by applying a swept sine signal to the error port of the control loop.

As can be seen from the Figure 5.4, the response of the actuator (PZT) is flat up to about 60 kHz. Above this frequency, the actuator has several resonances, the first resonance appears at $\approx$ 70 kHz. This lead to a phase lag and thus limits the bandwidth[2] of the control loop to $<$ 60 kHz. The designed controller consists of a low-pass filter and a proportional gain stage. The corresponding measured transfer function is shown in Figure 5.4 and agrees very well with the simulated transfer function. As can be seen from the measured open-loop transfer function, the loop has a unity gain frequency of $\approx$ 27 kHz with a phase margin of about 60°. It can also be seen that the measured transfer function agrees very well with the simulated one. The simulated open-loop transfer function consist of the measured transfer function of the PZT and the simulated transfer function of the controller. In order to make the dynamic range of the High Power Laser actuator as large as possible, the output signal of the controller is amplified by a high-voltage amplifier with a gain of 15 V/V and an output voltage of 150 V. The transfer functions are measured with a network analyzer *Stanford Research SR785* and a swept sine signal with an amplitude of $\approx$ 10 mV. The swept sine signal is injected to the error point while the loop is closed.

5.2.2 Frequency noise performance

To estimate the length noise of the Production Cavity, the amplitude spectral density (ASD) of the error and control signal are measured with the network analyzer while the loop is closed. This measurement is shown in Figure 5.5. To calibrate these signals in terms of frequency, the control signal is multiplied by the frequency response of the High Power Laser actuator. This factor is measured by applying a linearly increasing voltage signal to the frequency actuator, which results in a linear change of the frequency of the High Power Laser. The frequency spacing of the sidebands in the Pound-Drever-Hall error signal is then used to determine the voltage-dependent frequency change produced by the actuator, which is measured to be (1.5 $\pm$ 0.2) MHz/V. Additionally, the control signal is calibrated with the transfer function of the actuator shown in Figure 5.4. This is to account for the fact that the response of the actuator is, for frequencies close to and above its resonances, frequency dependent.

The calibration of the error signal can be realized in two ways. The first one is to use the slope of the linear regime of the error signal, which can be measured by determining the voltage change of the error signal due to frequency change, which is induced by a control signal ramp. As described in [36], the slope of the error signal depends on several parameters, including alignment between the eigenmode of the incident beam and the eigenmode of the cavity. Therefore, it has to be reevaluated every time the system is aligned or has drifted. For the

[2]The bandwidth limit of a transfer function is defined as the frequency, where the phase of the open-loop transfer function reaches -180° [63].

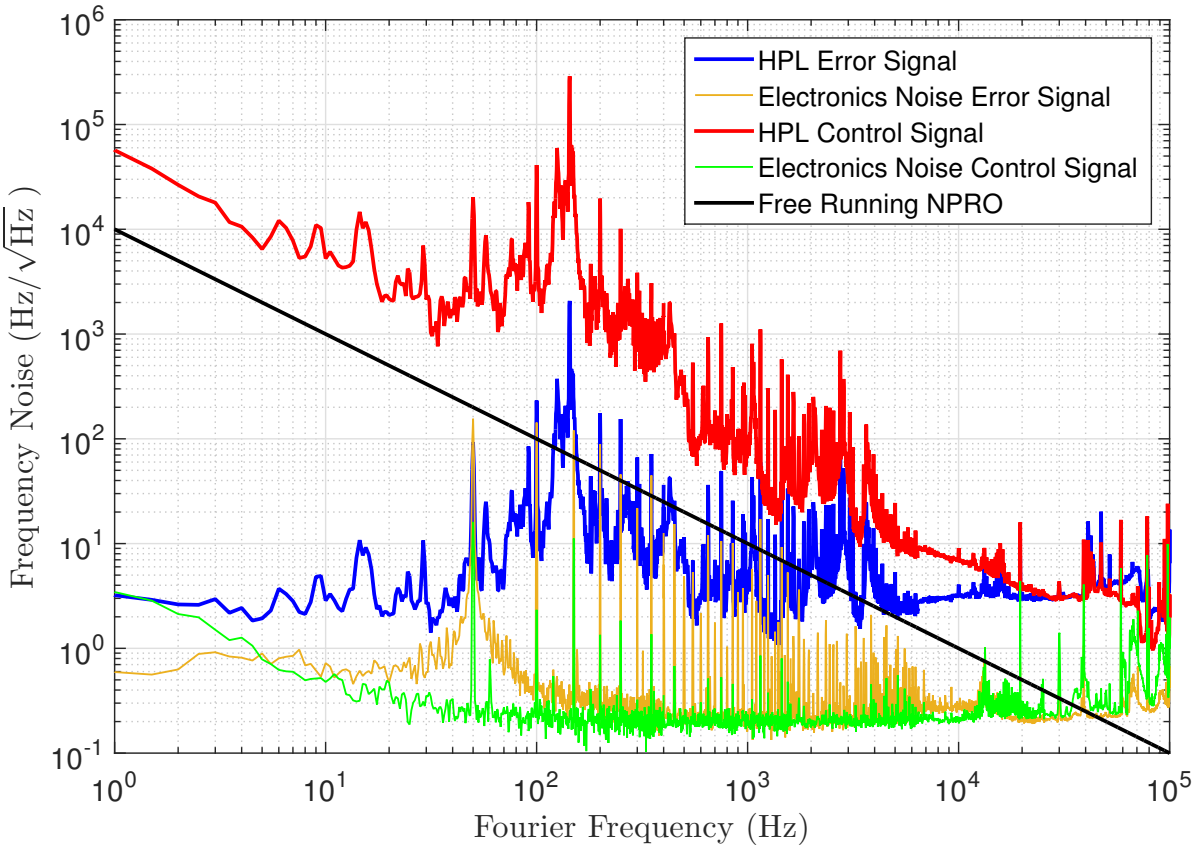

Figure 5.5: Calibrated amplitude spectral density of the error and control signal of the frequency stabilization control system of the High Power Laser. The control signal is calibrated with the voltage-dependent frequency change of the High Power Laser's actuator, which is (1.5 ± 0.2) MHz/V, the gain factor of the high-voltage amplifier which is 15 V/V, and the transfer function of the High Power Laser's frequency actuator. The error signal is calibrated with a factor according to is slope, which is (0.57 ±0.1) V/MHz. The shown electronics noise is measured while the loop is open and the photodiode is covered. Their calibration is done in the same way as the control and error signal.

measurement shown in Figure 5.5, the calibration factor for the error signal, according to its slope, is measured to be (1.7±0.3) MHz/V. On the other hand, the unity gain frequency of the open-loop transfer function of the control system can be used. At the unity gain frequency of the open-loop transfer function, the control and error signal are equal. This fact can be used to calibrate the error signal such that it crosses the calibrated control signal at the unity gain frequency of the open-loop transfer function. For the measurements in this chapter, the slope of the error signal is used to calibrated the error signals.

As can be seen from the Figure 5.5, the calibrated signals cross at about 27 kHz, which is the unity gain frequency of the control system. Below the unity gain frequency, the control signal represents the length fluctuation of the free running Production Cavity. It is noticeable that the free running Production Cavity fluctuates more than a free running NPRO by a factor about five.

It is important to note that the NPRO noise shown is not the noise of the free running High Power Laser but a general assumption for such NPROs, which is measured in various experiments [69–71]. Its amplitude spectral density is estimated with $\frac{10}{f}\ \frac{\mathrm{kHz}}{\sqrt{\mathrm{Hz}}}$ and the frequency noise of the High Power Laser is assumed to be in the same order. The free running noise is most likely caused by acoustics, which couples into length fluctuation by various mechanisms. On the one hand, acoustic noise can excite eigenresonances of the mechanical mounts of the optics, as is the case with the mount of the length actuator of the Production Cavity. This is noticeable in the frequency range around 140 Hz, since the noise is significantly increased in this band. As shown in Section 5.4.2, the length actuator has several eigenresonances and one of them is around 140 Hz. However, acoustic noise can also cause air density fluctuations and thus lead to fluctuations in the optical length of the cavity, which directly couple into frequency fluctuations. Although a metal tube is placed between the mirrors of the cavity to minimize the effect of air fluctuations, better protection of the cavity is necessary to completely avoid these effects. A possible solution might be to operate the cavity in a vacuum chamber. However, since the free running noise does not limit the experiments presented in this chapter, this option is not further investigated.

The calibrated error signal represents, below the unity gain frequency, the differential frequency noise between the High Power Laser and the Production Cavity with suppression from the control system. It can be seen that at about 10 Hz the control system design provides a suppression of the free running noise by about four orders of magnitude. The shown electronics noise in the error and control point are measured while the loop is open and the photodiode $\mathrm{PD}_{\mathrm{PDH-PC}}$ is covered, meaning no light incident on it. They are calibrated in the same way as the control and the error signal. As can be seen, the electronics noise in the error point does not exceed the error signal noise, which means that the suppressed noise is mostly dominated by the differential frequency noise between the laser and the cavity and the electronic noise is not the dominated noise source. In addition, the electronics noise in the control point is below the free running noise and thus not limiting the measurement.

This calibrated frequency noise of the free running Production Cavity is used in Section 5.4.1 to design and implement a control loop for the phase-locked loop between the Production Cavity field and the fundamental field of the Reference Laser.

5.2.3 Relative power noise performance

Since the circulating Production Cavity field is injected into the Regeneration Cavity, it is of interest to analyze its relative power noise (RPN) performance. Figure 5.6 shows the amplitude spectral density of the relative power noise downstream of the Production Cavity, of the free running High Power Laser, and that of the High Power Laser while its frequency is stabilized

to the length of the Production Cavity. The latter is referred to as the input beam in the further course of this chapter. The High Power Laser is equipped with an internal fast control loop, the so-called *noise eater*, which suppresses the power noise originating from the relaxation peak of the High Power Laser [72]. It is observed, however, that the noise eater does not function properly and the noise eater control loop starts oscillation randomly until it is reset. To ensure a consistent measurement, the noise eater is therefore deactivated for the measurements in this chapter.

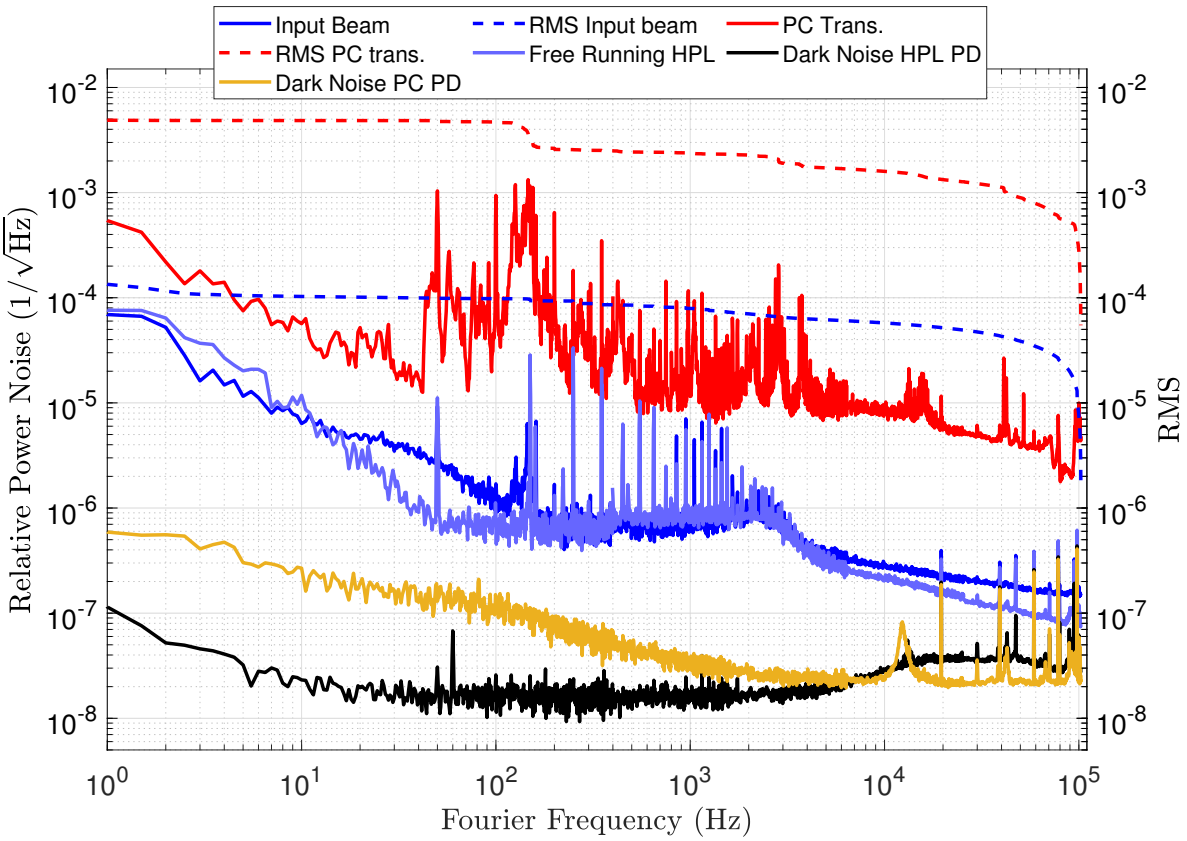

Figure 5.6: Amplitude spectral density of the relative power noise of the beam downstream the Production Cavity, the free running High Power Laser and the input beam. The dark noise 'HPL PD' trace corresponds to the photodiode used in front of the cavity for the free running High Power Laser and for the input beam while 'PC PD' corresponds to the photodiode used downstream of the cavity. The increased relative power noise in transmission of the Production Cavity is most likely caused by beam pointing of the input beam and by frequency fluctuations, which couples into relative power noise.

To determine which features contribute the most to power noise, the root mean square (RMS) of the spectra is also shown. The RMS is calculated by numerically integrating the power spectral density with respect to the frequency. The integration is performed from high frequencies down to the frequency the RMS is plotted at. The RMS is then plotted as a standard deviation, which is the square root of the value of the integration.

As can be seen from the measurement, the relative power noise of the beam downstream of the Production Cavity decreases in the frequency band between 1 Hz and 40 Hz, but is overall about one order of magnitude higher than the power noise of the input beam for this frequency range. Between 50 Hz and 200 Hz, the relative power noise is about three orders of magnitudes higher than that of the input beam. For frequencies between 200 Hz and 4 kHz, there is about two orders of magnitude difference between the power noise of the input beam and the beam downstream of the cavity. And at frequencies above 4 Hz, the difference decreases to about one order of magnitude. There are several possible explanation for the increase of the relative power noise downstream of the Production Cavity. On the one hand, it can be caused by beam pointing, e.g., lateral or angular fluctuation of the position of the input beam with respect to the eigenmode basis of the Production Cavity. As shown in Equation 5.8, the input beam can be express as a superposition of the spatial eigenmodes of the Production Cavity [34, 73]

$$|U_{in}|^2 = |U_{00}|^2 + \varepsilon_x^2 |U_{10}|^2 + \varepsilon_y^2 |U_{01}|^2 , \tag{5.8}$$

with $\varepsilon_{x,y}^2$ being the misalignment parameter for the vertical and horizontal plane described in Chapter 2. Since the higher-order modes are non resonant within the cavity when the cavity is locked on the fundamental mode, they are reflected by the cavity. Therefore, any lateral and angular misalignment fluctuations would lead to power fluctuations in transmission of the Production Cavity. On the other hand, frequency fluctuation of the High Power Laser can also couple into power noise of the transmitted Production Cavity beam. To verify these hypotheses, the input beam is observed with a quadrant photodiode and a coherence measurement is performed between the transmitted power and the differential power in the pitch and yaw plane on the quadrant photodiode. The differential power on the quadrant photodiode is measured according to Equation 4.8. Additionally, the coherence is measured between the relative power noise and the frequency noise. For the frequency noise, the signal in the control port of the control system is observed. These measurements are shown in Figure 5.7. As can be seen from the Figure 5.7, there exists a significant coherence of up to 1 between pitch and the relative power noise for frequencies between 30 Hz and 70 kHz. A similar coherence also exist for the yaw. The origin for this pointing could be either a motion of the optic mounts or a motion of the High Power Laser beam itself with respect to the eigenmode of the Production Cavity. To avoid this high coupling, an auto-alignment system, based on the differential wavefront sensing method, could be implemented [73, 74]. A significant coherence of up to 0.95 is also observed between the frequency noise and the relative power noise for frequencies between 40 Hz and 150 Hz, which means that beside pointing, frequency noise also contributes to the power noise at that frequency band. Above 150 Hz, the coherence is not significantly pronounced, but it is not completely negligible and contributes to a small extent to the power noise. This can be seen

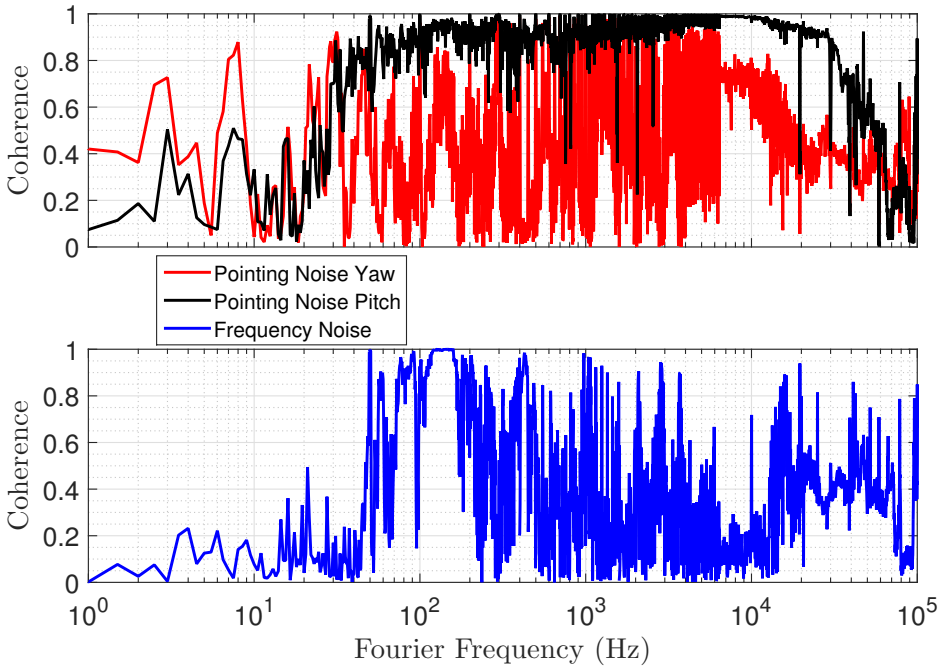

Figure 5.7: (Top) Coherence measurement between the relative power noise downstream of the Production Cavity and beam pointing of the input beam in pitch and yaw measured with a quadrant photodiode. (Bottom) Coherence measurement between relative power of the Production Cavity and the frequency fluctuation of the High Power Laser measured in the control point of the control system.

again in the spectrum of the input beam, since for frequencies between 4 kHz and 100 kHz its noise is increased compared to the free running High Power Laser noise. The spectrum of the transmitted power noise also shows several peaks, e.g. between 2 kHz and 4 kHz, which are also present in the spectrum of the length noise of the cavity, which additionally confirms that there is a clear coupling between frequency noise and power noise.

Because the control signal is used to determine a possible coherence between the relative power noise and the frequency noise, the observed coherence shown in Figure 5.7 could also be caused by another mechanism. The frequency of the laser is actuated by the control signal applied to the PZT of the laser. Driving the PZT might cause pointing, which would be observable in the control signal and in the relative power noise, which would lead to a coherence.

Thus, it can be concluded that the increased relative power noise downstream of the Production Cavity is most likely caused by pointing and frequency noise, which couples into relative power noise. However, since this increased relative power noise does not limit the experiments in this chapter, it is not further investigated.

The total RMS of the relative power noise downstream of the Production Cavity is 5×10^{-3}, which is about two orders of magnitude higher than that of the input beam. The broadband noise around 110 Hz accounts for about 40 % of the RMS, while the noise between 110 Hz and 4 kHz is responsible for 10 % of the RMS. The noise above 4 kHz accounts for 50 % of the RMS.

In Section 5.4, this transmitted Production Cavity beam is injected to the Regeneration Cavity. This is to investigate the influence of the phase-locked loop between the Production Cavity and the fundamental field of the Reference Laser on the Production Cavity beam while it is resonant within the Regeneration Cavity.

5.3 Performance of the Regeneration Cavity

To test the performance of the Regeneration Cavity, the second harmonic beam of the Reference Laser is mode matched and aligned to the eigenmode of the Regeneration Cavity, as described in Chapter 3. Then, the frequency of the Reference Laser is stabilized, as mentioned earlier, via its second harmonic beam to a resonance of the Regeneration Cavity. The eigenmode of the Regeneration Cavity is still spatially aligned to the Production Cavity eigenmode as described in Chapter 4 and remains unchanged.

In this section, the design of the control loop for the stabilization of the frequency of the Reference Laser is explained and the corresponding transfer function measurements are shown. Then, the performance of the Regeneration Cavity in terms of relative power noise and length noise is investigated and the corresponding measurements are discussed.

5.3.1 Design of the control loop

Similar to the Production Cavity, a controller is designed to stabilize the frequency of the Reference Laser to a resonance frequency of the Regeneration Cavity using its second harmonic field. The controller is designed based on the transfer function of the Reference Laser actuator, which is shown in Figure 5.8.

As Figure 5.8 shows, the actuator response is flat for the frequency range shown. As can be further seen, the phase response does not match the magnitude response. From about 10 kHz, a phase lag occurred, which is not consistent with the magnitude response. A possible explanation for this discrepancy might be a delay of the signal. As shown in Figure 5.8, a delay of $\approx 3.5\,\mu$s could explain this phase lag. Based on this transfer function, a controller is designed, which consists of a low-pass filter and a proportional gain stage. The corresponding simulated and measured transfer functions are shown in Figure 5.8. The proportional gain is chosen such that the unity gain frequency of the open-loop transfer function is about 30 kHz, as can be seen from the simulated transfer function. Furthermore, the measured open-loop transfer function agrees very well with the simulated one. The simulated open-loop transfer function consists of the measured transfer function of the Reference Laser actuator, which includes the delay, and the simulated transfer function of the controller. For this chosen unity gain frequency, the control loop has a phase margin of about 50°. Similar to the control loop of the Production Cavity, a

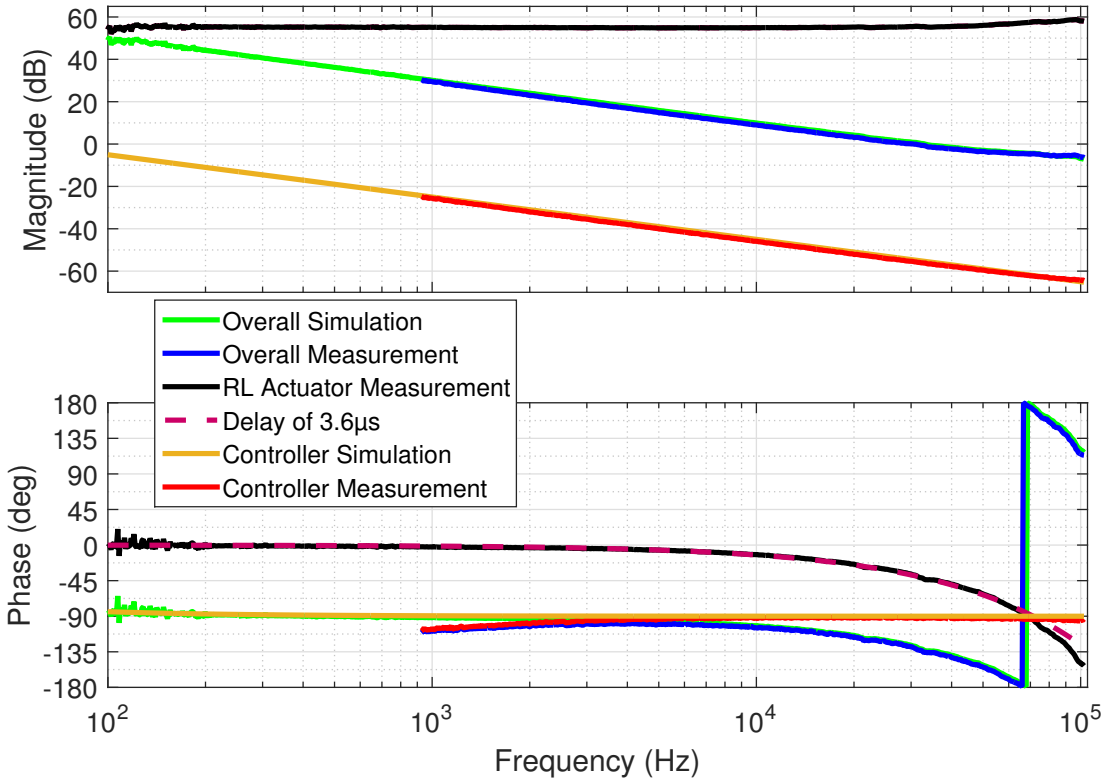

Figure 5.8: Bode plot of the transfer functions of the components for the frequency stabilization control loop of the Reference Laser and the corresponding overall transfer function with a bandwidth of $\approx 30\,\mathrm{kHz}$. The phase lag in the transfer function of the Reference Laser actuator is most likely due to a delay of the signal. The transfer function are measured in analogy to the measurement shown in Figure 5.4.

high-voltage amplifier with a gain of $15\,\mathrm{V/V}$ and an maximum output voltage of $150\,\mathrm{V}$ is used to extend the dynamic range of the actuator.

5.3.2 Frequency noise performance

Similar to the Production Cavity, the amplitude spectral density of the error and control signal is measured to estimate the length noise of the Regeneration Cavity. The signals are calibrated in the way described in the previous section. The calibration factor for the actuator response is measured to be (2.5 $\pm$0.2) MHz/V for the fundamental frequency, i.e. (5 $\pm$0.4) MHz/V for the second harmonic frequency. The calibration factor for the error signal, according to its slope, is measured to be (200 $\pm$16) kHz/V. As can be seen in the measurement shown in Figure 5.9, the calibrated signals cross at about 30 kHz as expected, which corresponds to the unity gain frequency of the control system. The measurement shows that the free running noise of the Regeneration Cavity is also about a factor five higher than that of the estimated free running NPRO. Since the Regeneration Cavity is set up in a similar configuration and under similar conditions as the Production Cavity, it can be assumed that the same noise sources as described

in the previous section are the cause of this length noise. The broadband increase of the length noise at ≈ 120 Hz, as well as the increase at ≈ 1 kHz and 3 kHz are due to the resonances of the length actuator. The increase above 20 kHz is most likely due to the low phase margin of the control system.

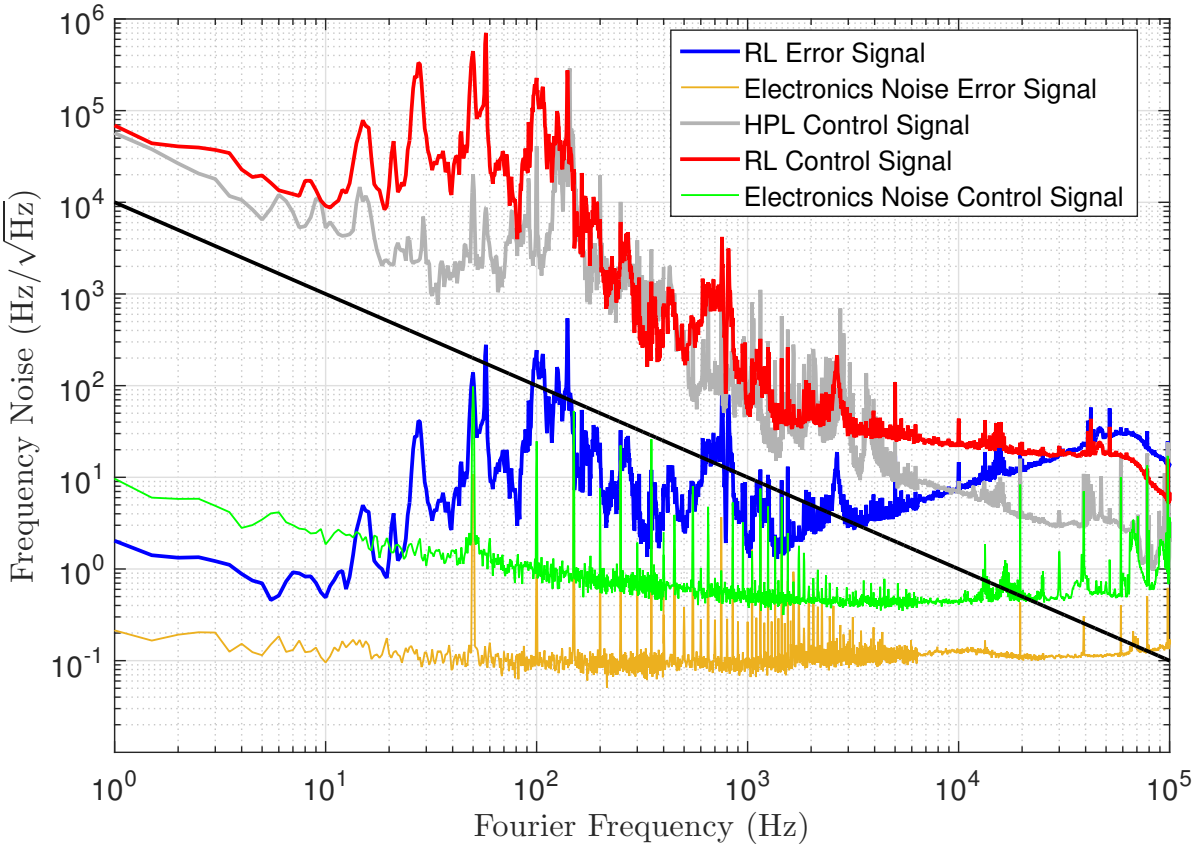

Figure 5.9: Calibrated amplitude spectral density of the error and control signal of the frequency stabilization control system of the Reference Laser. The control signal is calibrated with the gain of the high-voltage amplifier, which is 15 V/V, the transfer function of the Reference Laser actuator and its voltage-dependent frequency change, which is (5 ±0.4) MHz/V for its second harmonic beam. The error signal is calibrated with a calibration factor of (200 ±16) kHz/V. The electronics noises are measured while the loop is open and the photodiode is covered. They are calibrated with the same factors as the control and error signal.

To compare the free running length noise of the Regeneration Cavity with the free running length noise of the Production Cavity, the calibrated control signal of the High Power Laser frequency stabilization control system is also shown in the Figure 5.9. As can be seen from the Figure 5.9, the free running noise of both cavities is similar. However, between 10 Hz and 80 Hz and between 5 kHz and 30 kHz, the free running length noise of the Regeneration Cavity is slightly higher.

These two calibrated length noise signals are used to design a control system for the phase-locked loop in Section 5.4.

5.3.3 Relative power noise

While the loop is closed, the relative power noise of the second harmonic beam is measured downstream of the Regeneration Cavity, which is shown in Figure 5.10. Additionally, the relative power noise of the second harmonic beam of the free running Reference Laser and that of the second harmonic beam (input beam), while the frequency of Reference Laser is stabilized to a resonance frequency of Regeneration Cavity, is shown. It can be seen that below 10 Hz, the power noise downstream of the cavity is identical to the relative power noise of the input beam. Between 10 Hz and 6 kHz, the relative power noise of the transmitted beam is about one order of magnitude higher than that of the input beam. Between 6 kHz and 100 kHz, the noise decreases and at 100 kHz the noise is only about a factor of two above the input beam.

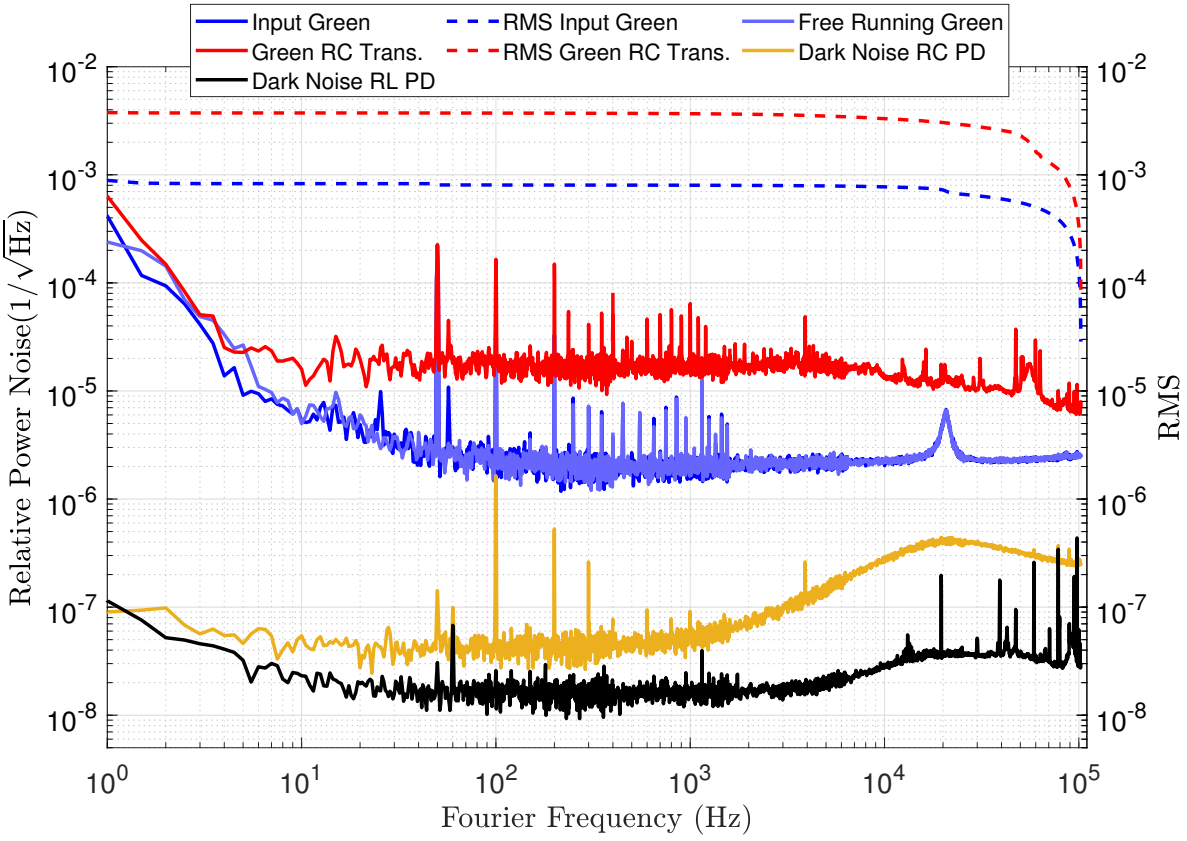

Figure 5.10: Amplitude spectral density of the relative power noise of the second harmonic beam of the Reference Laser downstream the Regeneration Cavity, the free running second harmonic beam, and the input beam. The dark noise 'RC PD' trace corresponds to the photodiode used downstream of the cavity while 'RL PD' corresponds to the photodiode used in front of the cavity for the free running Reference Laser and for the input beam. The increased relative power noise of the beam downstream of the Regeneration Cavity is most likely caused by beam pointing noise, which couples into power noise.

Since noise sources similar to the Production Cavity can be assumed, a coherence measurement between the power downstream of the cavity and the frequency noise, and pointing noise

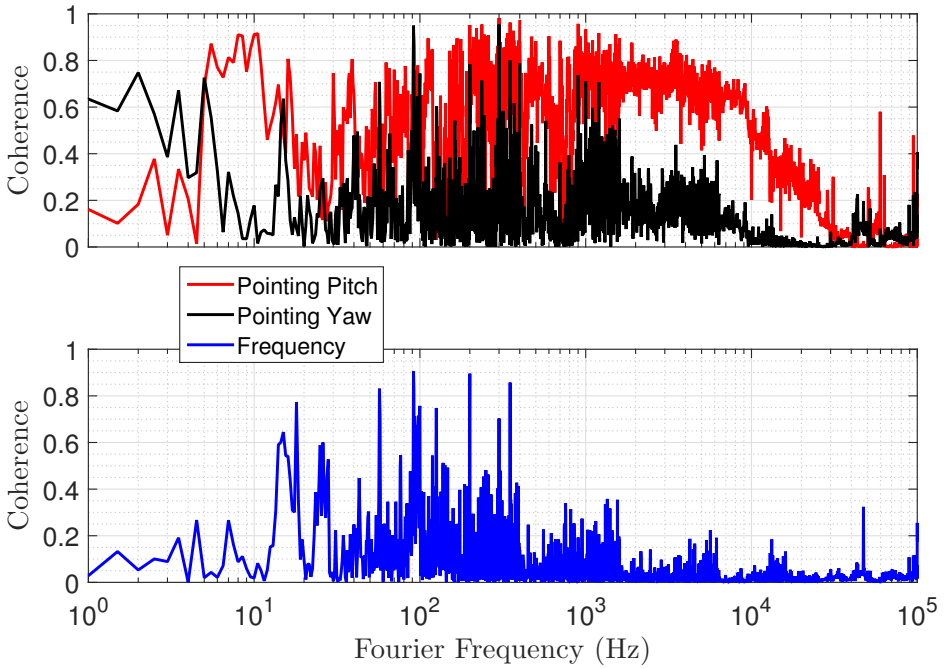

Figure 5.11: (Top) Coherence measurement between the transmitted relative power noise of the Regeneration Cavity and the pointing noise of the input beam in pitch and yaw. (Bottom) Coherent measurement between the relative power noise and the differential frequency noise between the Regeneration Cavity and the Reference Laser.

is performed. These measurements are shown in Figure 5.11. The measurement indicates a clear coherence of up to 0.8 between the pointing noise in pitch and the relative power noise. This decreases at frequencies above 10 kHz and is almost negligible at frequencies higher than 80 kHz. The coherence to yaw is significantly lower compared to pitch, but not completely negligible. Also the coherence to frequency is not that significant and can be neglected. Thus, it can be concluded, that the power noise downstream of the cavity is mostly caused by pointing noise. The mechanisms leading to the power noise due to pointing are the same as those explained in the previous Section 5.2. It can also be assumed that the pointing for the Regeneration Cavity is due to similar mechanisms as those for the Production Cavity.

In the noise spectrum of the second harmonic beam of the free running Reference Laser, a peak at about 20 kHz can be seen. This results from the fundamental beam of the Reference Laser. A measurement of the power noise directly at the output of the Reference Laser shows the same behavior at this frequency. Since this effect has no influence on the experiments in this chapter, no further investigation are done to eliminate it.

The total RMS of the relative power noise at the output of the Regeneration Cavity is 4×10^{-3}. It is thus about a factor five higher than the total RMS of the free running second harmonic beam of the Reference Laser, which is 8×10^{-4}.

When comparing the relative power noise of the second harmonic beam of the Reference

Laser downstream of the Regeneration Cavity with the relative power noise of the High Power Laser downstream of the Production Cavity, shown in Figure 5.6, it is noticeable that the power noise spectrum of the High Power Laser has significantly more peaks. The reason for this is not yet known and needs to be further investigated.

5.4 Dichroic lock of the Regeneration Cavity

This section shows the experiments related to the dichroic lock of the Regeneration Cavity. In a first attempt, the phase noise of the two free running cavities is analyzed, since it is via the frequency control system imprinted onto both the High Power and the Reference Laser and is thus important for the design of a suitable control system for the PLL. Subsequently, a dedicated control loop is designed for the Reference Laser and Production Cavity path and the result is verified experimentally. In the final step, the transmitted field of the Production Cavity is injected into the Regeneration Cavity and its performance downstream of this cavity is analyzed in terms of relative power noise.

5.4.1 Required bandwidth for the PLL

As described in the previous sections, the High Power Laser follows the Production Cavity, while the Reference Laser follows the Regeneration Cavity. Thus, the generated free running beat note signal between the field in transmission of the Production Cavity and the fundamental field of the Reference Laser represents the frequency difference between the Production Cavity and the Regeneration Cavity resonance frequency. The main actuator for the PLL is the length of the Production Cavity. Therefore, the PLL matches the length of the Production Cavity and thus the frequency of the High Power Laser to the resonance frequency of the Regeneration Cavity. The previously described feedback into the error point of the frequency stabilization control system of the Reference Laser only serves to achieve a high unity gain frequency for the PLL. Therefore, it has no impact on the matching of the frequency of the High Power Laser to the resonance frequency of the Regeneration Cavity. To estimate the free running noise of the PLL, the free running noise of both cavities, shown in Figure 5.5 and 5.9, is calibrated in terms of phase noise. The calibration is performed by multiplying the free running frequency noise by the factor $1/f_r$, where f_r represents the Fourier frequency. In a second attempt, the phase noise of both cavities is combined by summing them as uncorrelated noise sources:

$$\varphi_{sum} = \sqrt{\varphi_{PC}^2 + \varphi_{RC}^2}, \tag{5.9}$$

where φ_{PC} and φ_{RC} represent the calibrated free running phase noise spectrum of the Production and Regeneration Cavity, respectively. It is possible that common-mode noise sources exist for both cavities. Therefore, the assumption that the noise sources are uncorrelated is to be considered as a worse-case scenario. In a final attempt, the RMS of the combined phase noise is calculated in the manner described previously. Since the control signals of both cavities represent their free running phase noise only below their unity gain frequency, the RMS is calculated only for frequencies below theses unity gain frequencies in order to avoid a contribution of the higher frequency components to the RMS. The combined phase noise and the corresponding RMS are shown in in Figure 5.12. For the phase loop to be stable, the bandwidth of the control

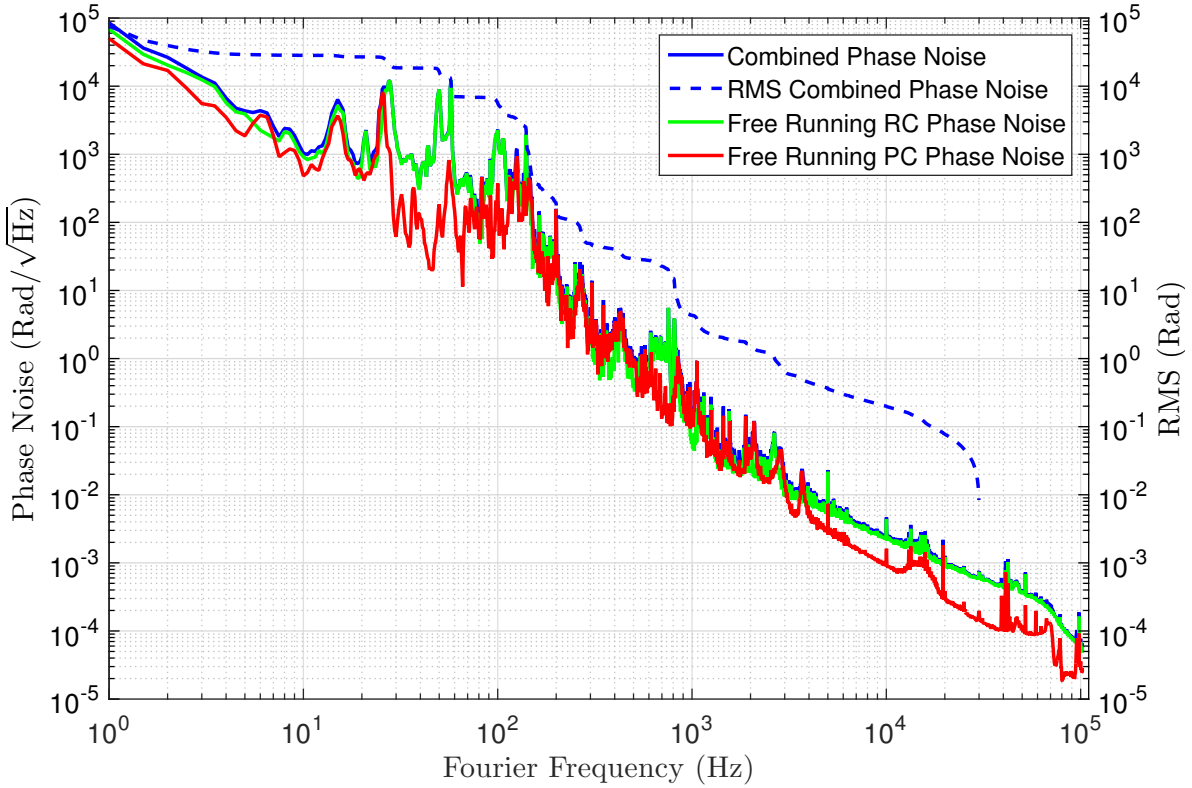

Figure 5.12: Calibrated phase noise of the free running Production and Regeneration Cavity and their combined phase noise. At the Fourier freuqency of $\approx 2.2\,\mathrm{kHz}$, the combined RMS provides a phase noise of $\approx \pi/2$ and thus determines the bandwidth for the control system of the phase-lock to $> 2.2\,\mathrm{kHz}$.

system has to be designed such that the total RMS phase noise above the unity gain frequency is $< \pi/2$. This is because phase noise exceeding $\pi/2$ would cause the linear range of the error signal to be exploited, resulting in loop instability. Ideally, the RMS phase noise above the unity gain frequency should be much smaller than $\pi/2$ to have sufficient linear dynamic range for the error signal to compensate the corresponding peak-to-peak fluctuations. Furthermore, it should be taken into account that phase noise of an integer of multiple of 2π would not be detected by phase detector due to phase wrapping. As can be seen in the Figure 5.12, the RMS of the

combined phase noise is at 2.2 kHz $\approx \pi/2$, which determines the bandwidth for the control system to > 2.2 kHz.

5.4.2 Production Cavity length actuator

The actuator used for the length actuation of the Production Cavity is mounted and calibrated in the same way as the Regeneration Cavity actuator described in Chapter 4. Since it has resonances that can limit the unity gain frequency for the PLL, its transfer function is measured. For that purpose, a perturbation signal is fed to the length actuator and a measurement is performed at the control port of the frequency stabilization system of the High Power Laser. The result of this measurement is shown in Figure 5.13. In the transfer function a first resonance is at $\approx$

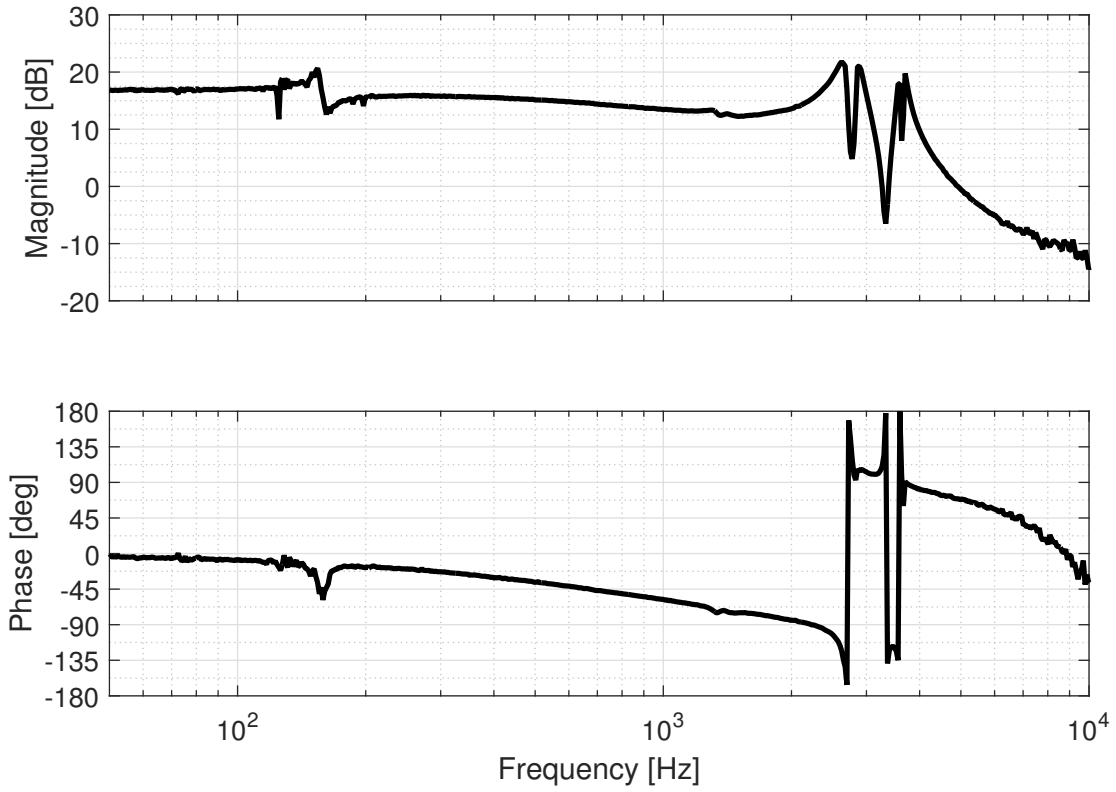

Figure 5.13: Bode plot of the transfer function of the Production Cavity length actuator. The actuator hast several resonances between 2.5 kHz and 4 kHz, which limits the Bandwidth for the control system of the phase-lock between the High Power Laser and Reference Laser.

150 Hz and others are much more pronounced between 2.5 kHz and 4 kHz. Due to these resonances, the bandwidth for the length actuation of the Production Cavity is limited to < 2.5 kHz. As explained in the previous section, a stable PLL requires RMS phase noises $< \pi/2$ above its unity gain frequency, which means that the length actuator alone is not sufficient to implement a robust control loop. Therefore, as already explained, the frequency of the Reference Laser

is additionally actuated by the PLL at high frequencies. It should be noted that the path of the PLL for the Production Cavity is designed to be stable on its own. The second path of the PLL, which is the Reference Laser path, can then be activated to provide more robustness to the PLL. If both paths are active, the crucial characteristics of the subsequent overall loop are the stability at the crossover frequency and the unity gain frequency of the faster path.

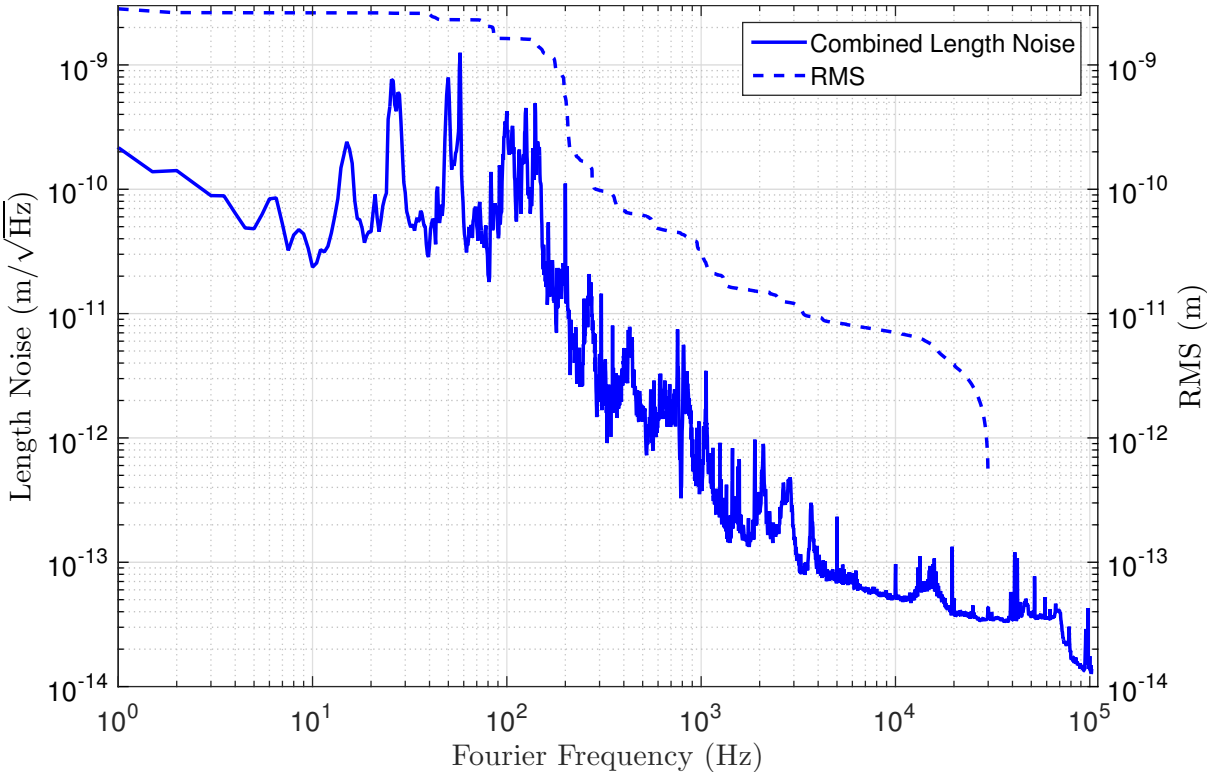

Figure 5.14: Calibrated and combined free running length noise of the Production and Regeneration Cavity. The total RMS of the length noise is $\approx 3\times10^{-9}$m, which prevents a saturation of the dynamic range of the Production Cavity length actuator.

The actuator used has a dynamic range of $\approx 12\,\mu$m. Since it needs to compensate the free running length noise of both cavities, the dynamic range might not be sufficient. Therefore, the combined free running noise of the cavities is calibrated in terms of linear length and the corresponding RMS is calculated to get an indication of possible saturation of the actuator. The result of this calculation is shown in Figure 5.14. It is obvious that the total RMS is $\approx 3\times10^{-9}$m and thus much smaller than the dynamic range of the actuator. Thus, it can be assumed that there is no saturation of the actuator.

Based on this information, dedicated control loops are designed for the Production Cavity and Reference Laser path of the PLL, which are described in the next sections.

5.4.3 Production Cavity loop

Based on the transfer function shown in Figure 5.13, a control system is designed for the Production Cavity path. As mentioned earlier, in the phase-locked loop the phase is measured, but for the phase tuning the frequency of the High Power Laser or Reference Laser is actuated. Consequently, the transfer function of actuator of the Production Cavity and Reference Laser has a $1/f$ characteristic, as shown in Figure 5.15. This fact needs to be taken into account to design a stable control loop.

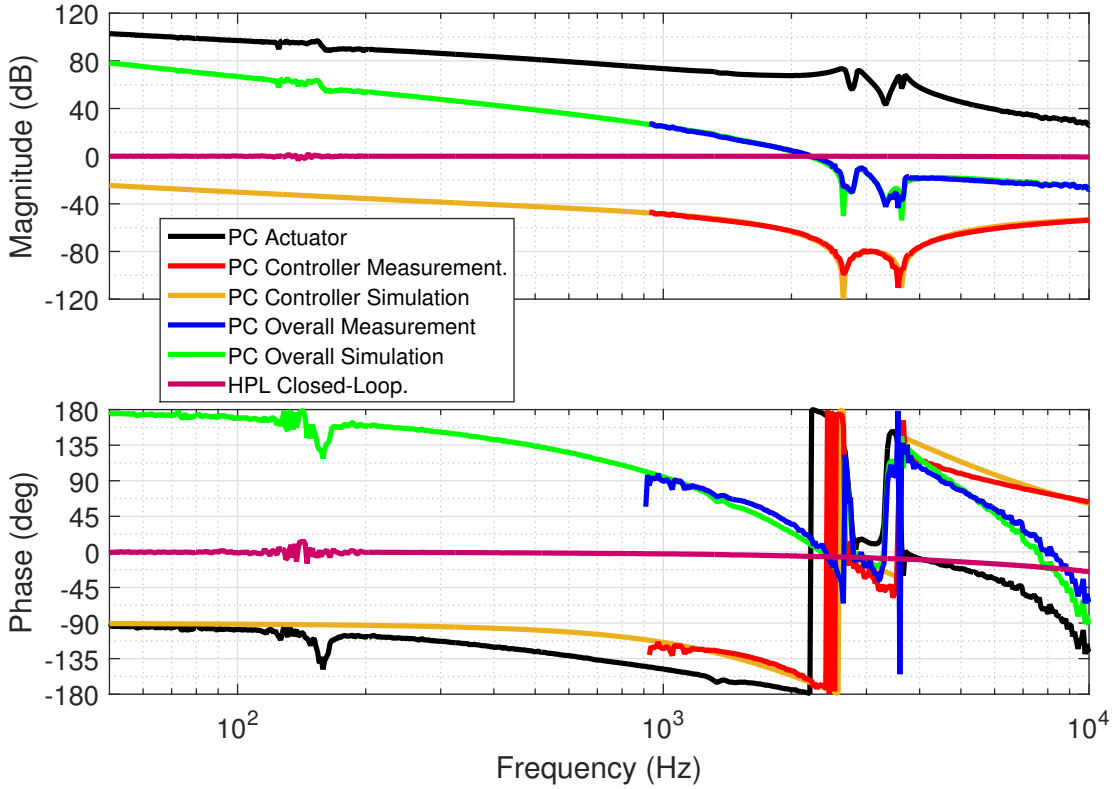

Figure 5.15: Bode plot of the simulated and measured transfer functions of the components for the phase-locked loop of the Production Cavity path and the corresponding simulated and measured total transfer functions. The resonances of the Production Cavity length actuator between 2 kHz and 4 kHz limit the bandwidth for the Production Cavity path of the PLL to < 2.5 kHz.

To reduce the impact of the mentioned resonances of the Production Cavity actuator for the control loop design, they are actively attenuated by two notch filters [75]. Then, a proportional gain is utilized to tune the unity gain frequency of this path to ≈ 2 kHz. To have sufficient gain for lower frequencies, an additional integrator is used for the frequency range below 1 kHz. The resulting simulated transfer function of the controller as well as the overall transfer function for the Production Cavity length control path are shown in Figure 5.15. The simulated overall transfer function consists of the measured transfer function of the Production Cavity length actuator, the closed-loop transfer function of the frequency stabilization system of the High Power

Laser, and the simulated transfer function of the controller. The open-loop transfer function of the High Power Laser lock has a unity gain frequency of $\approx 30\,\text{kHz}$, therefore the corresponding closed-loop transfer function has no significant influence on the overall loop of the Production Cavity path, because it is flat for the relevant frequency range of the Production Cavity path of the PLL. As can be seen in the Figure 5.15, the simulated and the measured transfer function of the designed controller are in good agreement. The controller is measured while the entire control loop (consisting of the Production Cavity and the Reference Laser path, which is explained in the next section) is closed. Also the measured overall loop agrees well with the simulated one. The achieved unity gain frequency for this path of the loop is $\approx 2.2\,\text{kHz}$. It should be noted that the overall phase of the overall loop experiences a sign change due to phase wrapping.

5.4.4 Reference Laser loop

In a similar approach, a dedicated control loop is designed for the Reference Laser path. Since the frequency of the Reference Laser is to be actuated only for higher frequencies, the controller consists of a high-pass filter of second order, as shown in Figure 5.16. The reason for this is

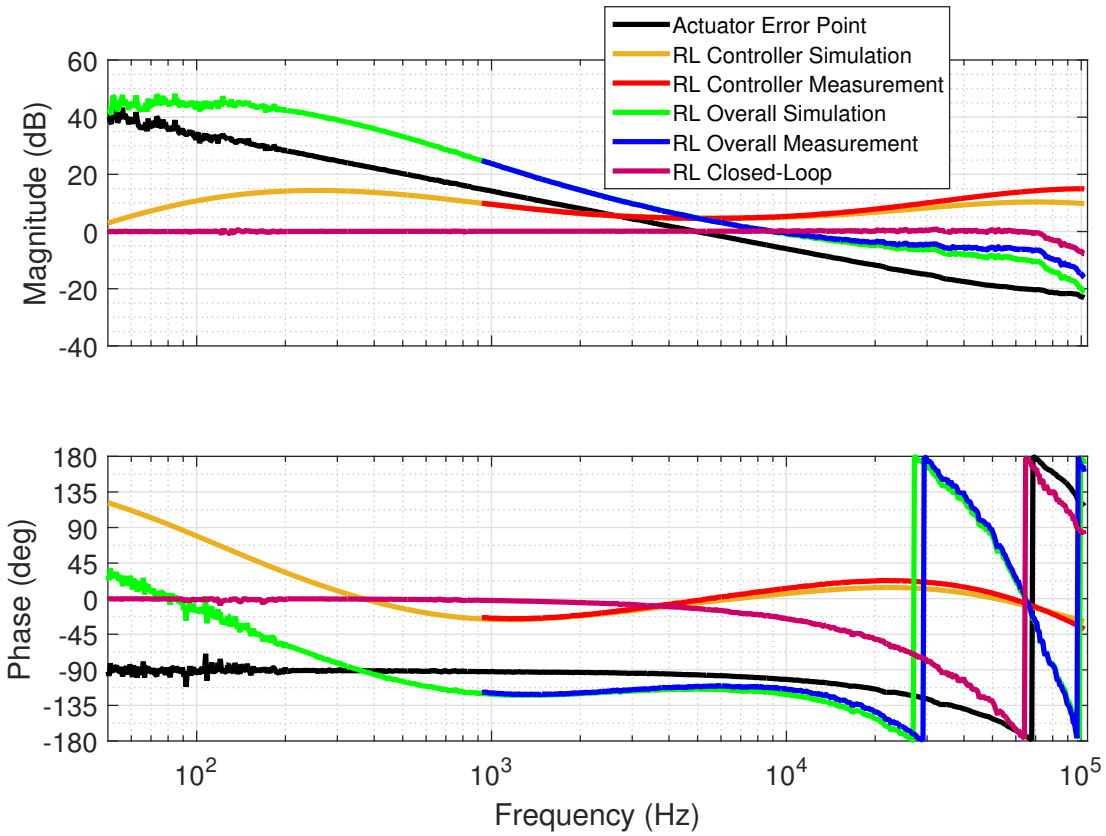

Figure 5.16: Bode plot of the transfer function of the components for the phase-locked loop of the Reference Laser path. The overall simulated transfer function has a unity gain frequency of $\approx 10\,\text{kHz}$ for the Reference Laser path, which is consistent with the measured overall transfer function.

that the transfer function of the actuator shows a $1/f$ characteristic. Consequently, a first order high-pass would only flatten the transfer function below its corner frequency. The second unit of the controller is a proportional gain stage, which is set to achieve a unity gain frequency of $\approx$ 10 kHz. The unity gain frequency is set such that the impact of the closed-loop transfer function of the Reference Laser on the magnitude and phase of the phase-locked loop is small. As can be seen in the Figure 5.16, the closed-loop transfer function of the Reference Laser is subjected to a phase lag, which does not correspond with the magnitude response. A possible explanation might be a delay of the signal. To support the loop with additional phase, the controller contains a differentiator for the transfer function of the Reference Laser path.

As shown in the Figure 5.16, the simulated and the measured transfer function of the controller are in good agreement. The simulated overall transfer function consist of the measured transfer function of the Reference Laser actuator, the closed-loop transfer function of the frequency stabilization system of the Reference Laser and the simulated transfer function of the controller. As can be seen, the measured overall transfer function is in good agreement with the simulated one. The phase margin at the unity gain frequency is $\approx 45°$. The transfer functions are measured in analogy to the performed measurement in the previous section.

5.4.5 Combined loop

To align the entire system and to close all loops contained, i.e. the loops for the frequency stabilization of the individual lasers and for the PLL, a certain procedure is followed, which is performed in several steps. These steps are as follows:

- In a first step, the frequency of the High Power Laser is stabilized to the resonance frequency of the Production Cavity.
- In a second step, the length of the Regeneration Cavity is tuned such that the transmitted Production Cavity field, which couples into the Regeneration Cavity, resonates within it.
- Then, the frequency of the Reference Laser is tuned such that its harmonic beam is also resonant within the Regeneration Cavity and then the corresponding Pound-Drever-Hall loop is closed.
- The length of the Production Cavity is slightly tuned, if necessary, such that its field is maximally resonant in the Regeneration Cavity and its corresponding path of the phase-locked loop is closed.
- In a final step, the path of the phase-locked loop for the Reference Laser is closed.

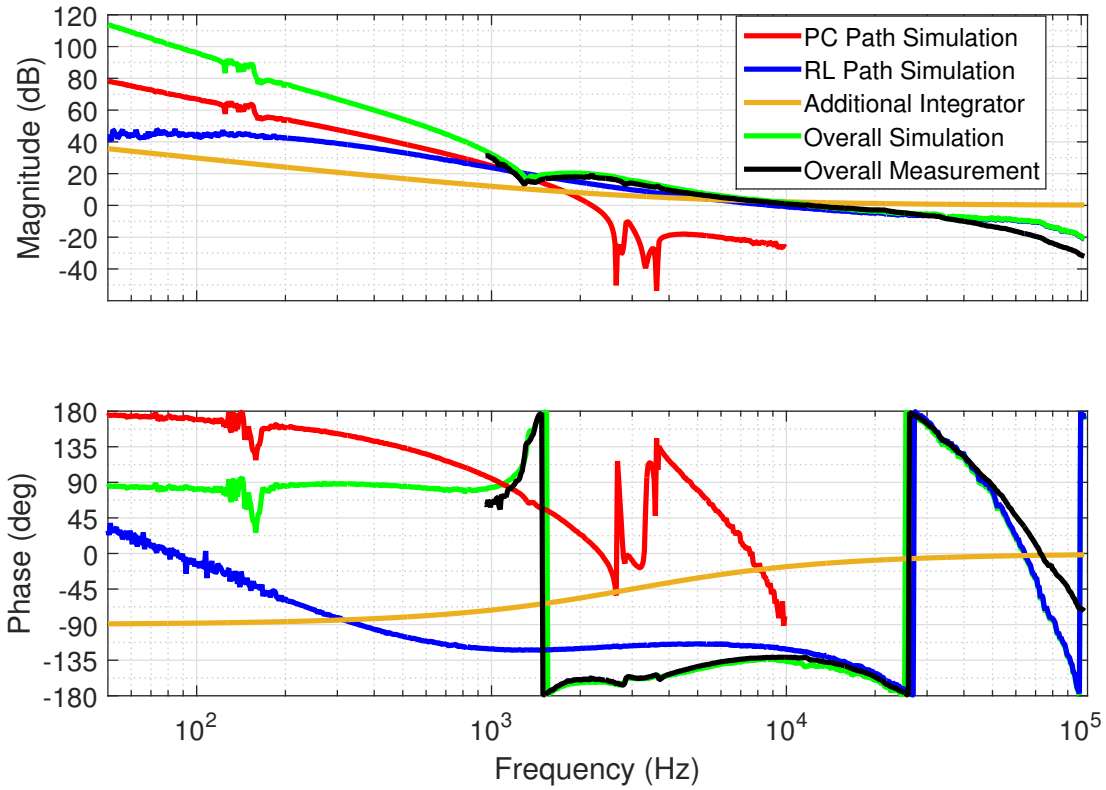

Figure 5.17: Bode plot of the transfer function of the entire simulated and measured phase-locked loop and the Production Cavity and Reference Laser path. The crossover frequency of the paths is ≈ 1.2 kHz. The achieved measured unity gain frequency of the overall loop is ≈ 10 kHz and the corresponding phase margin is $\approx 45°$. The overall loop provides a suppression of ≈ 100 dB at 10 Hz.

Once all loops are closed individually, the loop transfer function of the phase-lock is measured, which is shown in Figure 5.17. As can be seen from the measurement, the simulated crossover frequency between the two actuators is ≈ 1.2 kHz and is in agreement with the measured one. It should be noted that the phase difference of $\geq 180°$ between the two actuators at the crossover frequency is due to the phase wrapping of the phase of the Production Cavity path, as describe in Section 5.4.3. Taking this fact into account, the phase difference at the crossover frequency is $\approx 160°$, which means that the loop is stable at the crossover frequency. In both the measured and the simulated transfer function, a slight decrease of ≈ 6 dB of the magnitude can be observed at the crossover frequency, which is most likely due to crossover dynamics. The achieved unity gain frequency of the entire loop is ≈ 10 kHz and is in agreement with the simulated one. The corresponding phase margin is about 45°. In Addition to the previously described components in the path of the Reference Laser and Production Cavity, an integrator is added to the entire loop to provide sufficient suppression for frequencies below 3 kHz. As can be seen, the loop provides ≈ 100 dB suppression at ≈ 100 Hz. According to the measured and simulated transfer function, the Production Cavity should follow the Regeneration Cavity accurately up

to the crossover frequency. To verify this, an additional measurement is performed. While all loops are closed, a swept sine signal with an amplitude of $\approx$ 1 mV is injected to the length actuator of the Regeneration Cavity. Then, a transfer function measurement is performed from the Regeneration Cavity length actuator to the control signal of the Production Cavity actuator. Because the crossover frequency is about 1.2 kHz, the magnitude of this transfer function should be constant up to this frequency and then decreases. The corresponding measurement is shown in Figure 5.18. The measurement shows a constant magnitude for the frequency band up to $\approx$ 1 kHz. Between 1 kHz and 1.5 kHz, an increase in magnitude can be seen, which is most likely

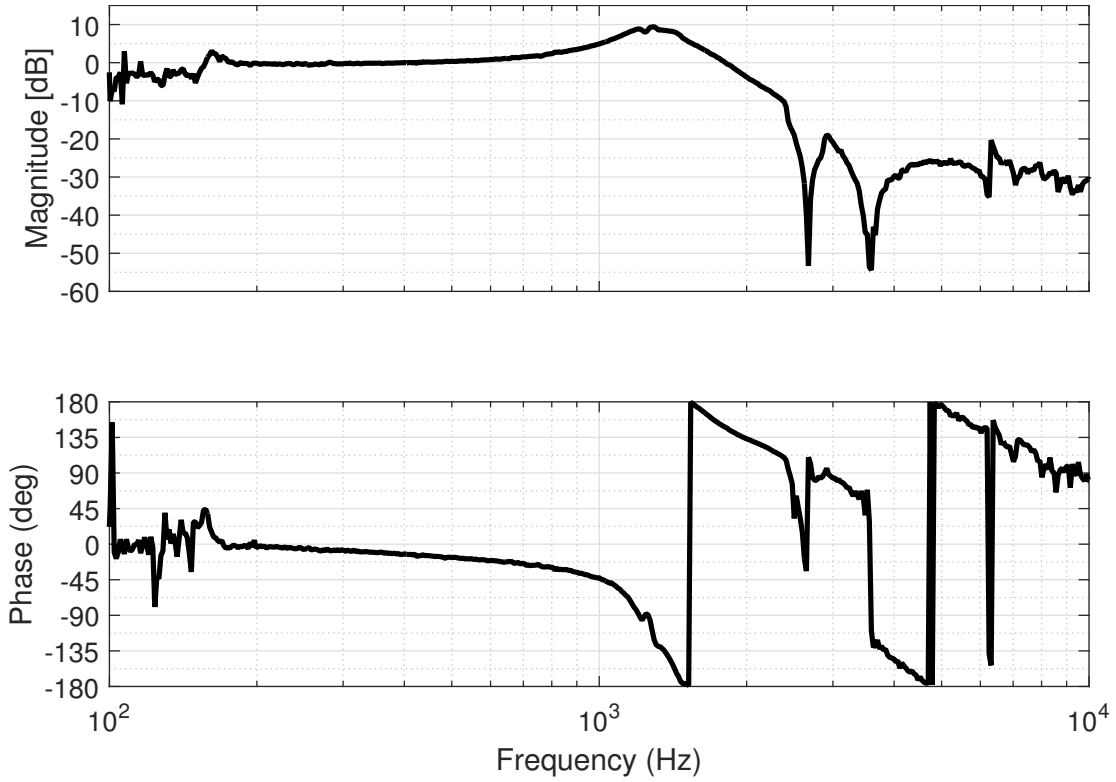

Figure 5.18: Bode plot of the transfer function measured from the Regeneration Cavity length actuator to the Production Cavity control signal. The measurement is performed while the phase-locked loop is closed and a swept sine signal is fed to the Regeneration Cavity lengths actuator to disturb its length. The measurement shows that the Production Cavity follows the Regeneration Cavity accurately up to the crossover frequency.

due to crossover dynamics. Above this frequency, as expected, a decrease of the magnitude is observed. The rapid decrease between 2 kHz and 4 kHz is caused by the resonances of the two actuators. This is also why the decrease in magnitude above the crossover frequency does not follow $1/f$ but $\approx 1/f^4$.

Thus, it can be concluded that the loop performs as expected with two different dominating actuators: the Production Cavity length actuator below the crossover frequency and the feedback to the Reference Laser above the crossover frequency. In the next sections, the control

system is used to investigate the performance of the PLL in terms of frequency noise and relative power noise of the involved beams.

5.4.6 Frequency noise performance

While the loop is closed, the amplitude spectral density of the error and control signal of both actuators is measured, which is shown in Figure 5.19. The corresponding electronics noise of the individual ports is shown in Figure 5.20. The control signal of the actuator of the Production

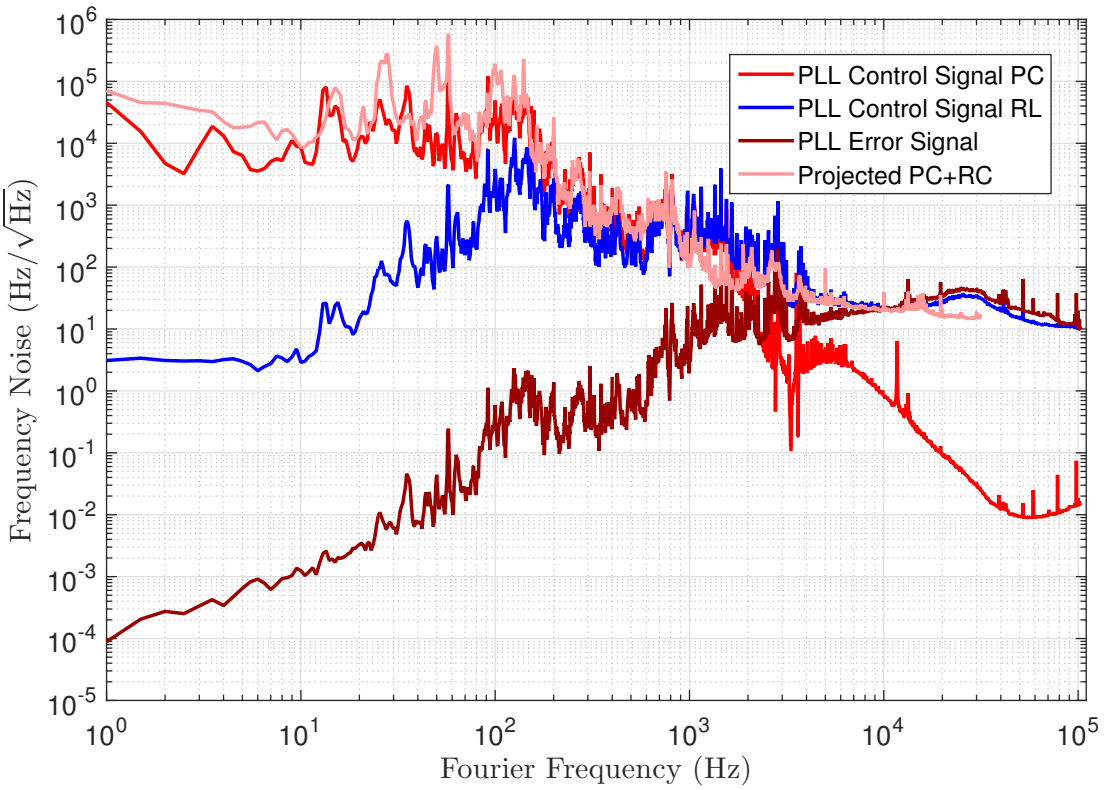

Figure 5.19: Calibrated amplitude spectral density of the error and control signal of the phase-locked loop. The calibrated control signal of the Production Cavity and Reference Laser actuators cross at $\approx 1.2\,\mathrm{kHz}$, which is the designed crossover frequency of the actuators. In addition to the control signals of the phase-locked loop, the free running noise of the Production and Regeneration Cavity is shown to verify that the length noise in the phase-locked loop is the free running noise of both cavities.

Cavity is measured at the output of the controller. To calibrate this signal, it is first multiplied by the calibration factor of the actuator. This factor is (20 ± 1.6) MHz/V and is measured in the same manner as described before. The signal is also calibrated with the gain of the High-Voltage amplifier, which is $7.5\,\mathrm{V/V}$, and the transfer function of the actuator shown in Figure 5.15. The control signal for the Reference Laser path is calibrated with a factor according to the slope of the Pound-Drever-Hall error signal of the Reference Laser, which is (200 ± 16) kHz/V, and the transfer function of the Reference Laser actuator, as shown in Figure 5.8. Since the

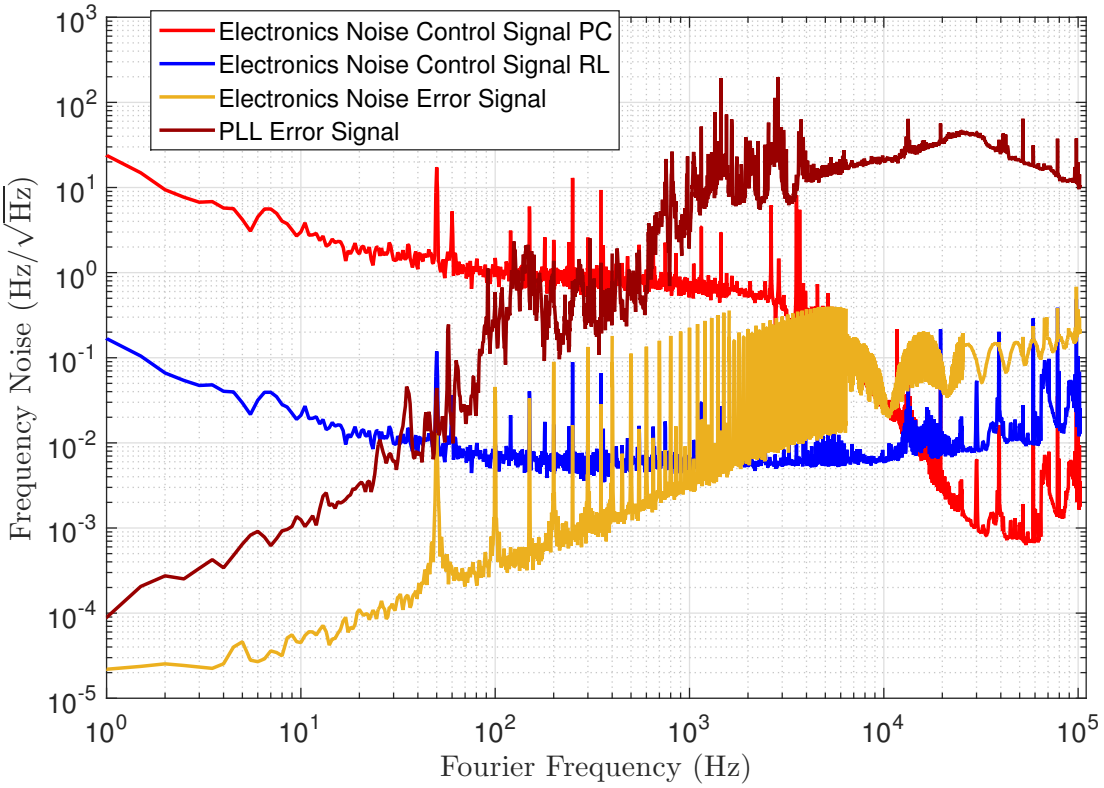

Figure 5.20: Calibrated amplitude spectral density of the electronics noise in the error and control port of the phase-locked loop. The signals are calibrated in the same way as the control and error signals shown in Figure 5.19

error signal of the PLL is proportional to phase, it is multiplied with $1/f_r$ to calibrate it with respect to frequency. It is then calibrated such that it crosses the control signal of the Reference Laser at the unity gain frequency. The electronic noises of the ports are calibrated in the same way as the signals. As can be seen, the calibrated control signals cross at $\approx 1.2\,\mathrm{kHz}$, which is the crossover frequency of the two actuators. As can further be seen, at frequencies below the crossover frequency, the control is done by the length actuator of the Production Cavity. At 10 Hz, its signal is about four orders of magnitude higher than that of the Reference Laser, which is determined by the high-pass filter implemented in the Reference Laser path. Above the crossover frequency, the control loop is mainly feeding back to the Reference Laser, whose signal is about three orders of magnitude higher than that of the Production Cavity actuator signal at $\approx 100\,\mathrm{kHz}$. The increase of the control signal of the Reference Laser above 10 kHz is most likely caused by the low phase margin of the PLL.

Since at low frequencies the Production Cavity follows the Regeneration Cavity and at high frequencies the Reference Laser follows the Production Cavity, the free running noise of both cavities is imprinted on the PLL. To verify this, the uncorrelated sum of the free running noise, from Sections 5.2 and 5.3, is also shown in the Figure 5.19 (Projected PC + RC). Since the two lasers have each a frequency-stabilization bandwidth of $\approx 30\,\mathrm{kHz}$, their control signals

represent only the free running noise below the unity gain frequency. Therefore, the noise spectral density is only shown up to 30 kHz. The Figure 5.19 clearly shows that the calibrated control signal of the PLL system, at frequencies between 1 Hz and 30 kHz, corresponds to the free running noise of both cavities.

The control loop suppresses the free running noise of the cavities by about seven orders of magnitude at 20 Hz. From the calibrated error signal and the corresponding calibrated electronic error point noise, shown in Figure 5.20, it can be seen that the electronics noise does not exceed the error signal. This means, that the suppressed noise is mainly dominated by the differential free running noise between the two cavities. Also the calibrated electronics noise of the control ports is below the free running noise and is not limiting the measurement.

5.4.7 Relative power noise

To measure the relative power noise of the beam of the Production Cavity downstream of the Regeneration Cavity, the local oscillator frequency of the PLL is tuned such that the power in transmission of the Regeneration Cavity is maximized. It is observed that the PLL local oscillator frequency has to be tuned at regular intervals during the measurements. Variations in temperature and humidity in the laboratory are assumed to lead to changes in the characteristics of the dichroic coating and thus in the penetration depths of the two beams. Furthermore, it is observed that if the frequency deviates from the optimum, the relative power noise downstream of the cavity increases significantly. Most likely, this is due to the fact that the lock is no longer at the maximum of the resonance frequency of the cavity and therefore the frequency noise is much more strongly coupled into the power noise. Figure 5.21 shows the amplitude spectral density of the relative power noise of the second harmonic beam of the Reference Laser, the Production Cavity beam downstream the Regeneration Cavity, and the Production Cavity beam before injected to the Regeneration Cavity. This measurement is performed under optimized conditions, i.e. with an optimally tuned offset frequency.

As can be seen from the Figure 5.21, the relative power noise of the beam of the Production Cavity downstream of the Regeneration Cavity is about one order of magnitude higher than the relative power noise of the injected beam for frequencies between 1 Hz and 1 kHz. Above 1 kHz, it falls off and from about 5 kHz it is about factor two higher than the relative power noise of the injected beam. Considering the power noise of the green beam and comparing it with the power noise without PLL in Section 5.3, it is noticeable that its power noise is also about one order of magnitude higher in the frequency range between 1 Hz and 1 kHz. Similar to the infrared beam, its power noise falls off above 1 kHz and has the same power noise as the green beam without PLL from about 5 kHz. The power noise of the beam of the Production Cavity in front of the Regeneration Cavity does not seem to experience a significant increase

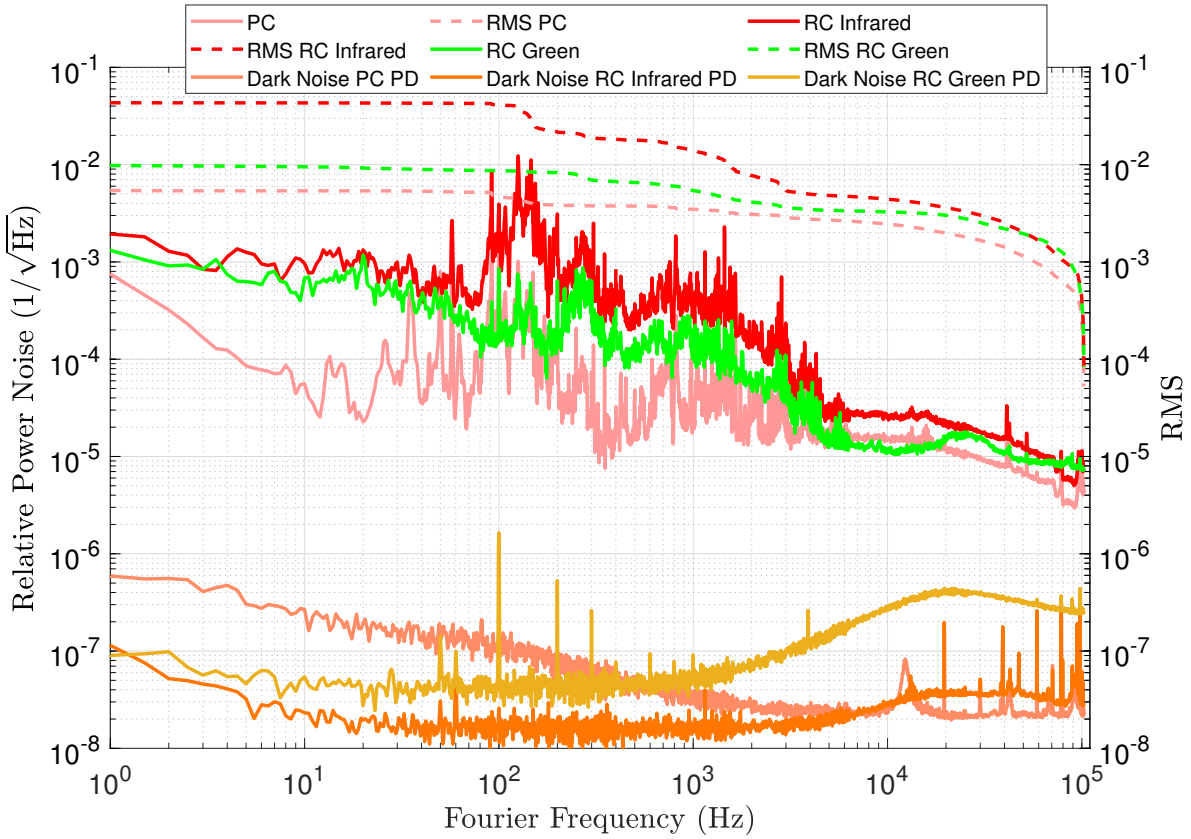

Figure 5.21: Amplitude spectral density of the relative power noise of the different beams and their RMS. 'PC' represents the relative power noise in transmission of the Production Cavity, while 'RC Red' represents the Production Cavity beam in transmission of the Regeneration Cavity. 'RC green' represents the relative power noise of the second harmonic field of the Reference Laser in the transmission of Regeneration Cavity.

of the power noise due to the PLL when compared to the measurement in Section 5.2. The measurement before the Regeneration Cavity shown here is performed simultaneously with the measurement downstream of the cavity. To determine whether there is a coherence between the differential frequency noise between the two cavities and the relative power noise downstream of the Regeneration Cavity, a coherence measurement is performed. The measurement is performed between the power noise of the infrared beam in transmission of the Regeneration Cavity and the control signals of both actuators. Additionally, a coherence measurement between the power in transmission of the Production Cavity and downstream of the Regeneration Cavity is performed. These measurements are shown in Figure 5.22.

As can be seen, the coherence between the power downstream of the Regeneration Cavity and the control signal of the individuals actuators is negligible at frequencies below 10 Hz but increases to up to 1 for the frequency band between 1 kHz and 4 kHz. It decreases for frequencies between 4 kHz and 20 kHz to about 0.4 and is negligible for frequencies above 20 kHz. A coherence is also observed between the beam of the Production Cavity before and in trans-

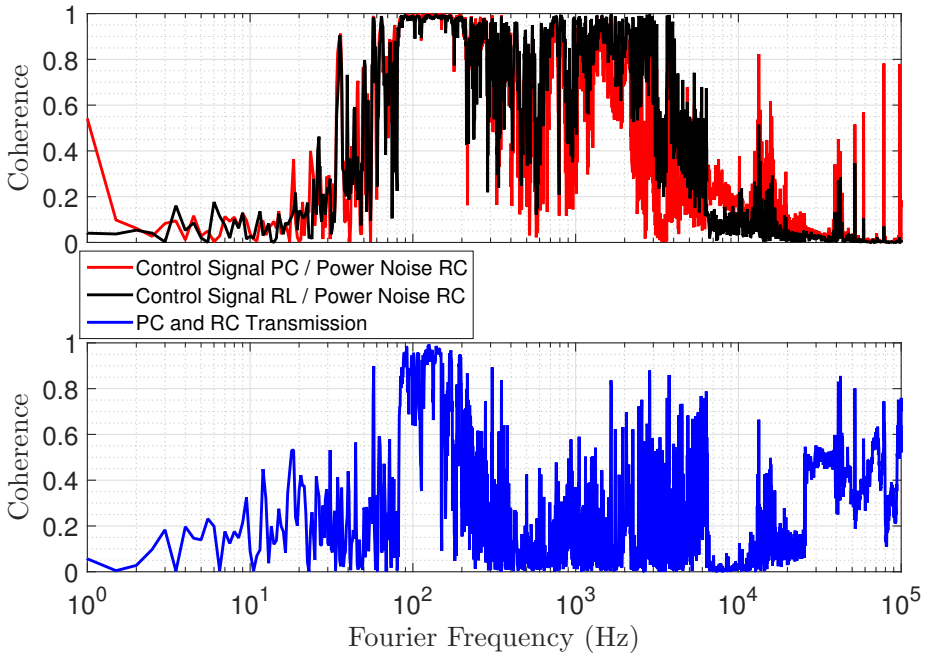

Figure 5.22: Coherence measurement between the power noise in transmission of the Regeneration Cavity and the control signal of the Production Cavity and Reference Laser actuator, and between the power in transmission of the Production Cavity and Regeneration Cavity.

mission of the Regeneration Cavity. In the frequency band between 100 Hz and 150 Hz, the coherence is very significant with a value ≈ 1 and decreases to about 0.7 for frequencies above 150 Hz but never gets negligible.

The increased power noises of the second harmonic beam downstream of the Regeneration Cavity in the presence of the PLL is most likely due to the feedback into the error point of the Reference Laser frequency-stabilization loop. The feedback is treated by the frequency-stabilization loop as artificial frequency noise, which means that the Reference Laser cannot accurately follow the resonance frequency of the Regeneration Cavity. This frequency noise most likely couples into power noise. As described before, the departure of the harmonic beam of the Reference Laser from the Regeneration Cavity resonance does neither influence the length of the Regeneration Cavity nor the frequency of the High Power Laser. Thus, it has no impact on the resonance condition of the High Power Laser beam within the Regeneration Cavity and can be excluded as a cause for the increased power noise of the High Power Laser beam downstream of the Regeneration Cavity.

The increased power noise of the infrared beam downstream of the Regeneration Cavity is not yet fully explained. A possible reason for this could be phase or frequency noise of the local oscillator at low frequencies. This would cause the PLL to act on the length of the Production Cavity, although the Regeneration Cavity length remains unchanged. As a result, the Production Cavity field would no longer follow the infrared resonance frequency of the Regeneration Cavity

accurately, which could result in power noise. Another explanation could be pointing induced to the Production Cavity by the PLL while it is actuating the length of the Production Cavity. This would cause pointing of the transmitted Production Cavity beam that the Regeneration Cavity converts to relative power noise. These hypotheses need to be verified in further experiments.

The total RMS of the power noise of the infrared beam in transmission of the Regeneration Cavity is 4 % and thus below the set target of 5 %. The noise between 3 kHz and 100 kHz is responsible for 13 % of the total RMS while the noise between 150 Hz and 3 kHz contributes about 47 % to the total RMS. The noise in the frequency band below 150 kHz is responsible for the remaining 40 %.

5.5 Summary and Conclusion

In order to stabilize the frequency of the High Power Laser to a resonance frequency of the Production Cavity, a dedicated control loop is designed and implemented. By measuring the corresponding transfer function of the control loop, it is shown that it provides a unity gain frequency of ≈ 30 kHz as expected by the design. Thus, the control loop is able to suppress the differential frequency or length noise between the Production Cavity and the High Power Laser by about three orders of magnitude at ≈ 20 Hz. Furthermore, it is shown that the Production Cavity is about five times more noisy than the free running NPRO. The reasons for this are attributable to the non-optimized environmental conditions, such as air flow fluctuations. It is further observed that the power noise downstream of the cavity is about one order of magnitude higher than the power noise of the free running High Power Laser. Based on various coherence measurements, it is shown that this is mostly caused by pointing and frequency noise, which couples into power noise.

The stabilization of the frequency of the Reference Laser is done based on the ALPS II design using its second harmonic beam and a suitable control loop. The control loop provides, similar to the lock of High Power Laser, a unity gain frequency of about 30 kHz and is able to suppress the free running differential length noise between the Regeneration Cavity and the Reference Laser by three orders of magnitude at about 20 Hz. The analysis of the free running length noise shows a length noise, which is a factor of about five higher than the corresponding frequency noise of a free running NPRO. Also here, the noise can most likely be attributed to the non-optimal environmental conditions. Compared to the relative power noise of the free running state, the power noise of the second harmonic beam is increased by about one order of magnitude downstream the Regeneration Cavity. Again, various coherence measurements show that this is mostly caused by pointing.

While the frequencies of the two lasers are individually stabilized to the respective cavities, a

phase-locked loop is implemented to keep the field circulating in the Production Cavity resonant in the Regeneration Cavity. Since both, the Production Cavity field and the second harmonic field of the Reference Laser within the Regeneration Cavity, experience different cavity lengths, the frequency offset between these fields is first determined empirically. For this purpose, both cavities are tuned in such a way that both beams resonate simultaneously in the Regeneration Cavity. Then, the beat note signal between the fundamental field of the Reference Laser and the Production Cavity field is measured, which is set as the offset frequency in the PLL. For the PLL two actuators are used: the length actuator of the Production Cavity is used for low frequencies, while at higher frequencies a signal is fed to the error point of the Pound-Drever-Hall loop of the Reference Laser. Using the Reference Laser path as a second actuator is necessary to obtain a robust PLL. For each actuator a suitable controller is designed such that the crossover frequency between the actuators is $\approx 1.2\,\mathrm{kHz}$ and the whole loop has a unity gain frequency of 10 kHz. Furthermore, the loop design suppresses the free running noise of the laser with respect to each other by about seven orders of magnitude at 20Hz. Based on the measured and calibrated control signals of both actuators, it is shown that the PLL's free running noise is similar as the summed free running length noise of both cavities, as expected.

The analysis of the relative power noise shows that the beam of the Production Cavity experiences an increase of its relative power noise downstream of the Regeneration Cavity. A similar behavior is also observed for the second harmonic beam in the presence of the PLL. The power noise for the harmonic beam is attributed to the feedback in its error point, while for the infrared beam the increased relative power noise is not yet explained. One possible explanation could be phase or frequency noise of the local oscillator of the PLL. Another explanation might be pointing induced to the Production Cavity by the PLL that the Regeneration Cavity converts to relative power noise. Despite this fact, it is shown that the power noise of the Production Cavity beam downstream of the Regeneration Cavity is below the ALPS II requirements of 5 %. ALPS II might face similar troubles concerning the infrared beam. Therefore, this effect needs to be investigated and understood more thoroughly. For this purpose, the local oscillator should be investigated and possibly replaced by another one with lower noise to exclude this effect. Also the pointing of the transmitted Production Cavity beam should be investigated in the presence of the PLL.

To prevent the high free running length noise of both cavities, a more effective protection of the cavities is necessary. One possible option might be to operate the cavities in a vacuum chamber. The vacuum chamber would also have the advantage of reducing the influence of temperature and humidity on the characteristics of the dichroic mirror. In addition, it would have the advantage of investigating the effect of different penetration depths within the dichroic coating with a complete setup under ALPS II-like conditions, i.e. high finesse cavities and high

intracavity power. This effect is not yet fully explained and needs further investigation.

Chapter 6

Summary

Within the scope of this thesis, a 1m-prototype is built to test and verify some fundamental requirements and concepts for ALPS II. In a first step, the Central Optical Bench concept is tested and verified with the aid of an autocollimator. Here, the main focus is on the angular alignment of the planar mirrors of both cavities with respect to each other. Two different mounting schemes are used to mount the mirrors to the Central Optical Bench. The first scheme is a Π-shaped frame designed for cuboid mirror substrates, which are placed on the Central Optical Bench. The alignment concept for this design is based on the high planarity of the Central Optical Bench surface and a best-effort rectangularity between the bottom surface and the highly-reflective surface of the mirror substrates. Despite some challenges, it is shown that it is possible to align the angular degree of freedom of the cuboid mirrors with a precision better than 5 μrad and to keep this alignment stable over a course of 180 h, which fully meets the ALPS II requirements. In a second attempt, an alternative commercial mount, which is designed for circular substrates, is tested. Its major benefit is the availability of alignment screws, which allow faster reproducible alignment in comparison to the Π-shaped frame. It is demonstrated by means of an autocollimator measurement that this mounting scheme provides a peak-to-peak stability of $\approx 2\,\mu$rad per degree of freedom over a course of ≈ 65 h, which also satisfies the ALPS II requirements.

To verify the autocollimator-assisted measurement, another experiment is performed. For this purpose, the planar mirrors of both cavities are aligned in advance, using the autocollimator, in such a way that their angular mismatch is less than 5 μrad. Then, the frequency of the High Power Laser is stabilized to a resonance frequency of the Production Cavity whose eigenmode is spatially overlapped with the eigenmode of the free running Regeneration Cavity. A subsequent mode scan in the eigenmode basis of the Regeneration Cavity shows that the relative power in the first-order mode is about $\approx 1.6 \times 10^{-4}$ and thus significantly below the value of 2.2×10^{-4}, which is expected for an angular misalignment of 5 μrad. Thus, the measurement confirms that

the autocollimator-assisted alignment of the planar cavity mirrors is sufficient to provide the requirements on the angular alignment for the ALPS II cavities.

In a further experiment, the readings of the quadrant photodiodes intended to be used for tracking the eigenmode position of the ALPS II cavities and the stability of their mechanical mounts are verified. In various experiments, it is shown that the quadrant photodiodes provide precise readouts of the eigenmode position of the cavities. Furthermore, it is shown that over a measurement period of $\approx 120\,\mathrm{h}$, the drift of the quadrant photodiodes is less than $20\,\mu\mathrm{m}$ in both the vertical and the horizontal plane, which meets the ALPS II requirements.

In the second part of this thesis, the entire frequency and length stabilization concept of ALPS II is demonstrated. Here, the frequency of the High Power Laser is stabilized to a resonance frequency of the Production Cavity while the frequency of the Reference Laser is stabilized via its second harmonic beam to the Regeneration Cavity. For each laser, a stabilization bandwidth of $\approx 30\,\mathrm{kHz}$ is achieved. Furthermore, it is observed that the free running noise of both cavities is about a factor of five above the estimated free running noise of the lasers, which is due to non-optimized environmental conditions. It is further observed that the relative power noise downstream of the cavities is increased in comparison to the power noise of the free running lasers. The reason could be attributed to pointing of the incident beam and the eigenmodes of the cavities relative to each other.

In a further step, the length of the Production Cavity is stabilized to the length of the Regeneration Cavity using a phase-locked loop, which acts on the length of the Production Cavity. To achieve a robust phase-locked loop, the Reference Laser is used as a second fast actuator by feeding a signal to the error point of its frequency-stabilization loop. Dedicated control loops are designed for each of the actuators and the performance of the entire control system is tested experimentally. It is shown by various measurements, that the crossover frequency of the actuators is $\approx 1.2\,\mathrm{kHz}$ and the entire loop has a unity gain frequency of $10\,\mathrm{kHz}$. Furthermore, it is shown that the RMS of the relative power noise of the Production Cavity beam downstream of the Regeneration Cavity is less than 5 %, which meets the ALPS II requirements, but significantly increased compared to the relative power noise in transmission of the Production Cavity. It is assumed that this is attributed to frequency noise of the local oscillator of the PLL or to pointing effects, which needs further investigations.

ALPS II will look into the dark side of the universe to probe particles beyond the Standard Model of particle physics. In order to achieve the desired sensitivity, the results obtained in this thesis regarding the lateral and angular alignment of both cavities as well as the stability of the associated components are of enormous importance. The demonstration of the control system for the frequency and length stabilization is also of major importance, since the overall ALPs detection concept strongly depends on a sophisticated control system.

Thus, the prototype successfully demonstrated and verified the requirements for lateral and angular alignment, the stability of quadrant photodiodes and the phase-lock concept for ALPS II.

Acknowledgements

I enjoyed doing my PhD at the AEI very much, as it was a very formative and educational time. I would like to thank everyone who made this time unforgettable and who supported me during the last years.

A very special thanks goes to my advisor Benno Willke. Thank you for giving me the opportunity to be part of your group and to work on this really interesting project. Thank you also for the excellent supervision, for the valuable advice and the many patient scientific discussions during the last years.

Thank you also to my dear colleagues from the laser group, Fabian, Nina, Ali, Marina, Joscha, Jasper, Nicole and Jan-Henning for the comfortable working atmosphere, the common group activities and the valuable support and advice. You created a working atmosphere in which it is a pleasure to work.

I would like to thank my colleagues from the ALPS collaboration for the great teamwork. In particular, I would like to thank Jan Põld for the support in the form of many discussions and advice as well as in the lab. Thanks for carefully reading the thesis and the very helpful comments. I would also like to thank Li-Wei for the great teamwork during the last years. Thanks for the advice and support in the lab. Thank you also to Todd and Alasdair James for proofreading the thesis. You guys were a great support.

I would like to thank all the other institute members who contribute to such a great working atmosphere. A special thank you goes to the colleagues in the electronics and mechanics workshops for making the many components.

Finally, I would like to thank all my friends and family for their support. A special thanks goes to my parents and my siblings, who have been supporting me all my life. I could always rely on your care and active support in any form. A family that you can always rely on is something very valuable.

Bibliography

[1] C. Berger; *Teilchenphysik Eine Einführung*; volume 1 (Springer-Verlag, Berlin-Heidelberg, 1992).

[2] M. Tanabashi et al.; *Review of Particle Physics*; Phys. Rev. D **98**, 030001 (2018).

[3] P. W. Higgs; *Broken Symmetries and the Masses of Gauge Bosons*; Phys. Rev. Lett. **13**, 508 (1964).

[4] S. Chatrchyan and et al.; *Search for the standard model Higgs boson decaying into two photons in pp collisions at s=7 TeV*; Physics Letters B **710**, 403 (2012).

[5] G. Aad et al.; *Observation of a new particle in the search for the Standard Model Higgs boson with the ATLAS detector at the LHC*; Physics Letters B **716**, 1 (2012).

[6] H. Kurashige; *Highlight of Results from ATLAS at LHC*; Physics Procedia **80**, 14 (2015); 26th International Conference on Nuclear Tracks in Solids (ICNTS26) Kobe, Japan 15th – 19th September 2014.

[7] J. Alves, F. Combes, A. Ferrara, T. Forveille, and S. Shore; *Planck 2015 results*; A&A **594**, E1 (2016).

[8] I. I. Bigi and A. I. Sanda; *CP Violation*; American Journal of Physics **69**, 1287 (2001).

[9] G. C. Branco, L. Lavoura, and J. P. Silva; *CP Violation*; volume 94 (Oxford University Press, Oxford, 1999).

[10] R. D. Peccei; *The Strong CP Problem and Axions*; Axions 3–17 (2008).

[11] R. Crewther, P. Di Vecchia, G. Veneziano, and E. Witten; *Chiral estimate of the electric dipole moment of the neutron in quantum chromodynamics*; Physics Letters B **88**, 123 (1979).

[12] R. D. Peccei and H. R. Quinn; *Constraints imposed by* CP *conservation in the presence of pseudoparticles*; Phys. Rev. D **16**, 1791 (1977).

[13] L. D. Duffy and K. Van Bibber; *Axions as dark matter particles*; New Journal of Physics **11**, 105008 (2009).

[14] D. Horns, L. Maccione, M. Meyer, A. Mirizzi, D. Montanino, and M. Roncadelli; *Hardening of TeV gamma spectrum of active galactic nuclei in galaxy clusters by conversions of photons into axionlike particles*; Phys. Rev. D **86**, 075024 (2012).

[15] M. Giannotti, I. Irastorza, J. Redondo, and A. Ringwald; *Cool WISPs for stellar cooling excesses*; Journal of Cosmology and Astroparticle Physics **2016**, 057 (2016).

[16] P. Arias, J. Jaeckel, J. Redondo, and A. Ringwald; *Optimizing light-shining-through-a-wall experiments for axion and other weakly interacting slim particle searches*; Phys. Rev. D **82**, 115018 (2010).

[17] P. Sikivie; *Experimental Tests of the "Invisible" Axion*; Phys. Rev. Lett. **51**, 1415 (1983).

[18] A. Wagner, G. Rybka, M. Hotz, L. J. Rosenberg, S. J. Asztalos, G. Carosi, C. Hagmann, D. Kinion, K. van Bibber, J. Hoskins, C. Martin, P. Sikivie, D. B. Tanner, R. Bradley, and J. Clarke; *Search for Hidden Sector Photons with the ADMX Detector*; Phys. Rev. Lett. **105**, 171801 (2010).

[19] B. Majorovits et al.; *MADMAX: A new road to axion dark matter detection*; Journal of Physics: Conference Series **1342**, 012098 (2020).

[20] J. L. Ouellet, C. P. Salemi, J. W. Foster, R. Henning, Z. Bogorad, J. M. Conrad, J. A. Formaggio, Y. Kahn, J. Minervini, A. Radovinsky, et al.; *First Results from ABRACADABRA-10 cm: A Search for Sub-*μeV *Axion Dark Matter*; Phys. Rev. Lett. **122**, 121802 (2019).

[21] V. Anastassopoulos, S. Aune, K. Barth, A. Belov, H. Bräuninger, G. Cantatore, J. Carmona, J. Castel, S. Cetin, F. Christensen, et al.; *New CAST limit on the axion–photon interaction*; Nature Physics **13**, 584 (2017).

[22] E. Armengaud, F. Avignone, M. Betz, P. Brax, P. Brun, G. Cantatore, J. Carmona, G. Carosi, F. Caspers, S. Caspi, et al.; *Conceptual design of the International Axion Observatory (IAXO)*; Journal of Instrumentation **9**, T05002 (2014).

[23] K. Ehret, M. Frede, S. Ghazaryan, M. Hildebrandt, E.-A. Knabbe, D. Kracht, A. Lindner, J. List, T. Meier, N. Meyer, et al.; *New ALPS results on hidden-sector lightweights*; Physics Letters B **689**, 149 (2010).

[24] P. Pugnat, L. Duvillaret, R. Jost, G. Vitrant, D. Romanini, A. Siemko, R. Ballou, B. Barbara, M. Finger, M. Finger, et al.; *Results from the OSQAR photon-regeneration experiment: No light shining through a wall*; Physical Review D **78**, 092003 (2008).

[25] A. S. Chou, W. Wester, A. Baumbaugh, H. R. Gustafson, Y. Irizarry-Valle, P. Mazur, J. H. Steffen, R. Tomlin, X. Yang, and J. Yoo; *Search for axionlike particles using a variable-baseline photon-regeneration technique*; Physical review letters **100**, 080402 (2008).

[26] R. Battesti, M. Fouché, C. Detlefs, T. Roth, P. Berceau, F. Duc, P. Frings, G. Rikken, and C. Rizzo; *Photon regeneration experiment for axion search using X-rays*; Physical review letters **105**, 250405 (2010).

[27] R. Bähre, B. Döbrich, J. Dreyling-Eschweiler, S. Ghazaryan, R. Hodajerdi, D. Horns, F. Januschek, E. A. Knabbe, A. Lindner, D. Notz, A. Ringwald, J. E. von Seggern, R. Stromhagen, D. Trines, and B. Willke; *Any light particle search II — Technical Design Report*; Journal of Instrumentation **8**, T09001 (2013).

[28] P. Sikivie, D. Tanner, and K. van Bibber; *Resonantly enhanced axion-photon regeneration*; Physical review letters **98**, 172002 (2007).

[29] A. Siegman; *Lasers*; volume 1 (University Science Books, Sausalito, 1986).

[30] F. Thies, N. Bode, P. Oppermann, M. Frede, B. Schulz, and B. Willke; *Nd: YVO 4 high-power master oscillator power amplifier laser system for second-generation gravitational wave detectors*; Optics letters **44**, 719 (2019).

[31] A. Hallal, G. Messineo, M. D. Ortiz, J. Gleason, H. Hollis, D. Tanner, G. Mueller, and A. Spector; *The heterodyne sensing system for the ALPS II search for sub-eV weakly interacting particles*; arXiv preprint arXiv:2010.02334 (2020).

[32] M. Hartman, A. Lindner, R. Smith, A. Spector, L.-W. Wei, K. Karan, J. Poeld, B. Willke, M. D. Ortiz, J. Gleason, et al.; *Design of the ALPS II Optical System*; arXiv preprint arXiv:2009.14294 (2020).

[33] J. Poeld and H. Grote; *ALPS II design requierment document*; Inernal Note, ID:D00000008263751 (2020).

[34] D. Z. Anderson; *Alignment of resonant optical cavities*; Appl. Opt. **23**, 2944 (1984).

[35] P. Kwee, F. Seifert, B. Willke, and K. Danzmann; *Laser beam quality and pointing measurement with an optical resonator*; Review of Scientific Instruments **78**, 073103 (2007).

[36] E. D. Black; *An introduction to Pound–Drever–Hall laser frequency stabilization*; American Journal of Physics **69**, 79 (2001).

[37] R. C. G. Smith; *Digital Control Systems in the Regeneration Cavity of ALPS IIa*; Ph.D. thesis; Hannover: Gottfried Wilhelm Leibniz Universität Hannover (2020).

[38] R. Drever, J. L. Hall, F. Kowalski, J. Hough, G. Ford, A. Munley, and H. Ward; *Laser phase and frequency stabilization using an optical resonator*; Appl. Phys. B 31 97–105 (1983).

[39] E. Benkler, A. G. Steffan, and H. R. Telle; *Frequency-Offset PLL for Synchronous Optical Sampling of OTDM Signals*; IEEE Photonics Technology Letters **19**, 267 (2007).

[40] T. J. Kane and E. A. Cheng; *Fast frequency tuning and phase locking of diode-pumped Nd:YAG ring lasers*; Opt. Lett. **13**, 970 (1988).

[41] W. R. Leeb, H. K. Philipp, A. L. Scholtz, and E. Bonek; *Frequency synchronization and phase locking of CO2 lasers*; Applied Physics Letters **41**, 592 (1982).

[42] F. Gardner; *Phaselock Techniques*; volume 3 (Wiley-Interscience, New Jersey, 2005).

[43] S. Spiekermann, F. Laurell, V. Pasiskevicius, H. Karlsson, and I. Freitag; *Optimizing non-resonant frequency conversion in periodically poled media*; Applied Physics B **79**, 211 (2004).

[44] S. C. Kumar, G. Samanta, and M. Ebrahim-Zadeh; *High-power, single-frequency, continuous-wave second-harmonic-generation of ytterbium fiber laser in PPKTP and MgO:sPPLT*; Opt. Express **17**, 13711 (2009).

[45] F. Acernese, M. Agathos, L. Aiello, A. Allocca, A. Amato, S. Ansoldi, S. Antier, M. Arène, N. Arnaud, S. Ascenzi, et al.; *Increasing the Astrophysical Reach of the Advanced Virgo Detector via the Application of Squeezed Vacuum States of Light*; Phys. Rev. Lett. **123**, 231108 (2019).

[46] M. Mehmet, S. Ast, T. Eberle, S. Steinlechner, H. Vahlbruch, and R. Schnabel; *Squeezed light at 1550 nm with a quantum noise reduction of 12.3 dB*; Opt. Express **19**, 25763 (2011).

[47] D. Spanner; *The Peltier Effect and its Use in the Measurement of Suction Pressure*; Journal of Experimental Botany **2**, 145 (1951).

[48] G. Boyd and D. Kleinman; *Parametric Interaction of Focused Gaussian Light Beams*; Journal of Applied Physics **39**, 3597 (1968).

[49] DataRay; *Beam Fit Algorithms, Application Notes*; https://dataray-web.s3.amazonaws.com/pdf/dataray-beam-fit-algorithms-app-note.pdf (2020); accessed: 21 June 2020.

[50] W. B. Ribbens; *Interferometric Surface Roughness Measurement*; Appl. Opt. **8**, 2173 (1969).

[51] B. P. Abbott, R. Abbott, T. Abbott, M. Abernathy, F. Acernese, K. Ackley, C. Adams, T. Adams, P. Addesso, R. Adhikari, et al.; *Observation of Gravitational Waves from a Binary Black Hole Merger*; Phys. Rev. Lett. **116**, 061102 (2016).

[52] E. Hecht; *Optik*; volume 5 (De Gruyter Oldenbourg, Munich, 2009).

[53] Trioptics; *Knowledge Base*; https://trioptics.com/products/triangle-electronic-autocollimators (2020); accessed: 03 August 2020.

[54] J. Yuan and X. Long; *CCD-area-based autocollimator for precision small-angle measurement*; Review of Scientific Instruments **74**, 1362 (2003).

[55] R. H. H. Bähre; *Design and setup of an optical experiment for searching for weakly interacting sub-eV particles (WISPs) that couple to an electro-and/or magnetic field*; Ph.D. thesis; Hannover: Gottfried Wilhelm Leibniz Universität Hannover (2017).

[56] F. Kawazoe, R. Schilling, and H. Lueck; *Eigenmode changes in a misaligned triangular optical cavity*; Journal of Optics **13**, 055504 (2011).

[57] M. R. Ardigo, M. Ahmed, and A. Besnard; *Stoney Formula: Investigation of Curvature Measurements by Optical Profilometer*; in *Residual Stresses IX*; volume 996 of *Advanced Materials Research*; 361–366 (Trans Tech Publications Ltd, 2014).

[58] J. Gunnars and U. Wiklund; *Determination of growth-induced strain and thermo-elastic properties of coatings by curvature measurements*; Materials Science and Engineering: A **336**, 7 (2002).

[59] L.-W. Wei, K. Karan, and B. Willke; *Optics mounting and alignment for the central optical bench of the dual cavity enhanced light-shining-through-a-wall experiment ALPS II*; Appl. Opt. **59**, 8839 (2020).

[60] L. M. Manojlović; *Resolution limit of the quadrant photodetector*; Optik **127**, 7631 (2016).

[61] M. González-Cardel, P. Arguijo, and R. Díaz-Uribe; *Gaussian beam radius measurement with a knife-edge: a polynomial approximation to the inverse error function*; Appl. Opt. **52**, 3849 (2013).

[62] Y. Panduputra, T. W. Ng, A. Neild, and M. Robinson; *Intensity influence on Gaussian beam laser based measurements using quadrant photodiodes*; Appl. Opt. **49**, 3669 (2010).

[63] A. Abramovici and J. Chapsky; *Feedbacl Control Systems, a Fast Track- Guide for Scientists and Engineers*; volume 1 (Kluwer Academic Publishers, Massachusetts, 2000).

[64] L. Enloe and J. Rodda; *Laser phase-locked loop*; Proceedings of the IEEE **53**, 165 (1965).

[65] T. Hansch and B. Couillaud; *Laser frequency stabilization by polarization spectroscopy of a reflecting reference cavity*; Optics Communications **35**, 441 (1980).

[66] D. Shaddock, M. Gray, and D. McClelland; *Frequency locking a laser to an optical cavity by use of spatial mode interference*; Opt. Lett. **24**, 1499 (1999).

[67] R. Boyd and D. Prato; *Nonlinear Optics*; volume 3 (Elsevier Science, Amsterdam, 2008).

[68] Onsemi; *Phase-Frequency Detector*; https://www.onsemi.com/pub/Collateral/MCH12140-D.PDF (2020); accessed: 09 October 2020.

[69] S. Brozek; *Frequenzstabilisierung eines Nd: YAG-Hochleistungs-Laser-Systems für den Gravitationswellendetektor GEO600*; Ph.D. thesis; Hannover: Gottfried Wilhelm Leibniz Universität Hannover (1999).

[70] D. Timothy; *Frequency-Stabilized Solid State Lasers for Coherent Optical Communications* ; Ph.D. thesis; Standford University (1991).

[71] P. Kwee and B. Willke; *Automatic laser beam characterization of monolithic Nd:YAG nonplanar ring lasers*; Appl. Opt. **47**, 6022 (2008).

[72] C. Harb, M. Gray, H.-A. Bachor, R. Schilling, P. Rottengatter, I. Freitag, and H. Welling; *Suppression of the intensity noise in a diode-pumped neodymium:YAG nonplanar ring laser*; IEEE Journal of Quantum Electronics **30**, 2907 (1994).

[73] E. Morrison, B. J. Meers, D. I. Robertson, and H. Ward; *Automatic alignment of optical interferometers*; Appl. Opt. **33**, 5041 (1994).

[74] E. Morrison, B. J. Meers, D. I. Robertson, and H. Ward; *Experimental demonstration of an automatic alignment system for optical interferometers*; Appl. Opt. **33**, 5037 (1994).

[75] H. Wupper and U. Niemeyer; *Elektronische Schaltungen 2, Operationsverstärker, Digitalschaltung, Verbindungsleitung*; volume 2 (Springer-Verlag, Berlin-Heidelberg, 1996).